



Norwegian University of
Science and Technology

Upgrading off-grades from the silicon process

Increasing the silicon yield from Elkem Thamshavn using
mechanical or metallurgical separation

Ole Jørgen Østensen

Chemical Engineering and Biotechnology

Submission date: June 2011

Supervisor: Gabriella Tranell, IMTE

Abstract

The aim of the thesis is to produce high grade silicon from off-grade materials like skulls and process slags from Elkem Thamshavn. The methods investigated are dense medium separation (DMS), optical separation, flotation and metallurgical separation by remelting. DMS trials are conducted using magnetite suspended in water and aim to find the suspension density where only one phase will float. Optical separation experiments are done to identify light intensity thresholds between refractories, silicon and slag. The viability of flotation without surface activators and at neutral pH are investigated by measuring the zeta potential of each phase. Remelting experiments are done, building on previous work by the author, with the aim of investigating whether adding CaO or MgO to the slag will increase the settling efficiency.

No results were obtained in the DMS experiments, because the viscosity of the suspension increased to infinity before the density of either slag or silicon was reached. The zeta potential experiments showed that flotation is not viable at neutral pH without surface activators, as the zeta potential of slag and silicon is nearly identical.

The optical separation experiments were a success. The product fraction had an average silicon content of 74 wt%, compared to 52 wt% in the original off-grade material, while the waste fraction contained 7.5 wt% silicon. The separation efficiency was best for coarser grains, which is the expected result based on theory.

The remelting experiments concluded that adding CaO or MgO to the slag will increase the settling efficiency. This was established both by chemical analysis and by surface area analysis of slag samples from each experiment. MgO seemed to contribute more to the settling efficiency than CaO, but because of the large variance between samples, this is not conclusive. The quality of the produced silicon was unaffected or improved by adding CaO, but additions of MgO increased the magnesium content slightly.

Acknowledgements

I wish to sincerely thank my supervisor, Gabriella Tranell, for all her help and assistance this past year. I would also like to thank Mark Kennedy and Jon Arne Bakken for helping me understand some of the electromagnetic theory behind induction furnaces, and for giving me the tools I needed to create my own version of the theory. However, I owe my understanding of the practical electronics of induction and RLC circuits to my father, Per Østensen, and my brother, Andreas Østensen. What our tiny induction “furnace” lacked in power, it made up for in learning and entertainment value.

I wish to express my gratitude to those who have aided me in my experiments; Arvid Rein and Kurt Sandaunet at SINTEF, Erlend Nordstrand and Dmitry Slizovskiy at IMT, Rolf Arne Kleiv at IGB, Jacek Kolacz at Comex and Frank D. Priesemann at Rana Gruber.

I also wish to express my deepest gratitude to everyone at Elkem Thamshavn for sponsoring my project, especially product manager Bente M. Faanes and managing director Alf Tore Haug.

Finally, I wish to thank Kristin Michalsen for all her love and support.

Table of Contents

1 Introduction.....	1
2 Theory.....	2
2.1 Mechanical separation of slag and freeze linings	2
2.1.1 Dense medium separation	3
2.1.2 Optical separation	6
2.1.3 Flotation	7
2.2 Remelting and settling of slag and freeze linings	9
2.2.1 The Al ₂ O ₃ -CaO-SiO ₂ slag system	9
2.2.2 Density.....	11
2.2.3 Viscosity.....	13
2.2.4 Surface and interfacial tension.....	15
2.2.5 Melt stirring speed	17
2.3 Furnace design.....	19
2.3.1 The induction furnace	19
2.3.2 Furnace design.....	21
2.3.3 Refractories	27
2.3.4 Freeze linings	30
2.3.5 Lining problems	33
3 Experimental procedure.....	37
3.1 Material	37
3.2 Mechanical separation experiments.....	38
3.2.1 Dense medium separation	38
3.2.2 Optical separation	39
3.2.3 Flotation – zeta potential analysis.....	40
3.3 Remelting and settling of silicon	40
4 Results	45
4.1 Mechanical separation experiments.....	45
4.1.1 Dense medium separation	45
4.1.2 Optical separation	45
4.1.3 Flotation – zeta potential analysis.....	47
4.2 Remelting experiments	48
4.3 Furnace design.....	52

4.3.1 Heat balance.....	52
4.3.2 Dimensioning an induction furnace for remelting off-grades.....	53
4.3.3 Freeze lining thickness.....	56
5 Discussion	59
5.1 Mechanical separation experiments	59
5.1.1 Dense medium separation	59
5.1.2 Optical separation	59
5.1.3 Flotation	61
5.2 Remelting experiments	62
5.2.1 Chemical analysis.....	62
5.2.2 Microscopy analysis.....	63
5.2.3 Experimental difficulties.....	66
5.2.4 Error analysis	69
5.3 Furnace design.....	71
5.3.1 Heat balance.....	71
5.3.2 Dimensioning an induction furnace for remelting off-grades.....	72
5.3.3 Freeze lining thickness.....	73
6. Conclusions.....	75
7 Future work	76
8. References	77
Appendix.....	80
1 Count data, microscopy analysis	80
2 Design of an induction furnace for remelting off-grades.....	82
3 Cooling system design for a furnace using freeze lining	85

TABLE OF FIGURES

Figure 1: Apparent viscosity of medium suspensions as a function of vol% solids. [3]	4
Figure 2: Flow sheet for dense medium separation.	5
Figure 3: Typical coal washability curve [10].	6
Figure 4: Off-grades	6
Figure 5: The Comex OSX optical separator [13].	7
Figure 6: Sketch of flotation agents on a mineral surface [3].	8
Figure 7: Zeta potential of feldspar and quartz as a function of pH [3].	9
Figure 8: The Al_2O_3 -CaO-SiO ₂ system [15].	10
Figure 9: Content of Al and Ca in the produced metal as a function of slag composition [1].	11
Figure 10: Isodensity curves (in g/cm ³) for the SiO ₂ -CaO-Al ₂ O ₃ system [15]. The cross marks the composition of the slag in the off-grades used in the remelting experiments. The blue line designates the approximate density of silicon at 1550 °C.	12
Figure 11: Density of the Al_2O_3 -CaO-MgO-SiO ₂ system as a function of MgO and SiO ₂ content [15].	12
Figure 12: Phase diagram for 30% Al_2O_3 -SiO ₂ -CaO-MgO [15].	13
Figure 13: Isoviscosity curves for the Al_2O_3 -CaO- SiO ₂ system at 1500 °C, [15]. Values in poise (0.1 Ns/m ²). The cross marks the composition of the slag in the off-grades used in the remelting experiments.	14
Figure 14: Silicate chains in slag partly broken by CaO [18].	15
Figure 15: Schematical overview of surface tension ^[20]	16
Figure 16: Critical bulk velocity for re-entrainment of droplets	18
Figure 17: A metal bar in an induction coil showing the magnitude and the phase shift of the induced eddy currents in the bar [30].	20
Figure 18: Sketch of the induction furnace proposed by Ahmed, Masoud and El-Sharkawy.	22
Figure 19: The 10 turn induction coil for aluminium billet heating proposed by Kennedy et al. [33].	22
Figure 20: 10 turn helical “current sheet” coil or solenoid [33].	23
Figure 21: Flow patterns in an induction furnace [38].	25
Figure 22: A plot of $\varphi\xi w$ as a function of ξw [33].	26
Figure 23: Isothermal section of the Al_2O_3 -MgO-SiO ₂ phase diagram [41].	28
Figure 24: Saturation lines between slag and refractories in the Al_2O_3 -CaO-SiO ₂ system [15].	30
Figure 25: Comparison of different cooling systems [50].	32
Figure 26: Different cooler solutions.	33
Figure 27: Spring loaded furnace [53]	35
Figure 28: Monitoring of copper coolers using ultrasonic sensors	36
Figure 29: Experimental setup for dense medium separation.	39
Figure 30: Analysis method used by Comex	39
Figure 31: Estimated slag compositions in experiments 1-5.	41
Figure 32: Estimated slag compositions in experiment 6 and 7. Alumina content is set at 30 wt%.	42
Figure 33: The ASEA induction furnace [59]	43
Figure 34: 8X8 mosaic image of a sample surface, each image was taken at 100X and joined into the larger image.	44
Figure 35: Left: The original mosaic image of a sample. Right: The binarized image of the same sample	44
Figure 36: Original and analyzed image of the coarse fraction (40-80 mm).	45
Figure 37: Original and analyzed image of the middle fraction (20-40 mm).	46
Figure 38: Original and analyzed image of the fine fraction (5-20 mm).	46
Figure 39: Results of the zeta potential analysis	47
Figure 40: Chemical analysis of produced slag. Oxides are given as fraction of the total slag, where Si_{met} is not included.	49
Figure 41: XRF analysis of the produced silicon.	50
Figure 42: Area fraction of silicon in samples from experiment 1, 2 and 3, 30 minutes holding time	50

<i>Figure 43: Area fraction of silicon in samples from experiments 4, 5, 6 and 7, 10 minutes holding time</i>	<i>51</i>
<i>Figure 44: Average area fraction and chemically determined silicon content of slag in each experiment.</i>	<i>51</i>
<i>Figure 45: Previous work and new mosaic area analysis of slags from previous work.</i>	<i>52</i>
<i>Figure 46: Schematic showing the dimensions of the furnace</i>	<i>55</i>
<i>Figure 47: Flow chart for an optical sorting process with reprocessing of waste products</i>	<i>61</i>
<i>Figure 48: Comparison of the first three experiments to previous work with 30 min holding time</i>	<i>65</i>
<i>Figure 49: Comparison of the last four experiments to previous work with 10 min holding time</i>	<i>65</i>
<i>Figure 50: A horizontal section through the crucible from experiment 7.</i>	<i>67</i>
<i>Figure 51: Failed experiment where the top of the charge sintered into an air-tight bridge which the building CO₂ pressure ejected from the crucible.</i>	<i>68</i>
<i>Figure 52: Failed experiment where the flux did not mix properly with the slag.</i>	<i>69</i>
<i>Figure 53: Flow sheet for a double optical sorting scheme</i>	<i>72</i>

1 Introduction.

The yield of silicon from metallurgical production in electric arc furnaces is governed by several aspects, like reaction rate, quality of products and other process parameters. Most of these aspects have already been looked at in some detail, for example by Schei, Tuset and Tveit [1] among several others. But one source of loss which seems to have been ignored is the loss of high grade product in off-grade materials like slag and skulls. The current industry practice is to sell off-grades as a low Si material to manganese producers, which use them to increase the Si content of their SiMn product. However, the price of off-grades per silicon unit compared to the price of high grade silicon is quite low, which means that there is an economic incentive to recover silicon from off-grade materials. There is an environmental incentive as well, as the total amount of waste from the silicon process is reduced. The aim of this thesis is therefore to find a simple, cheap, non-polluting way to recover high-grade silicon from off-grades, either mechanically, by comminution and separation, or metallurgically, by remelting and settling.

In previous work by the author, an attempt has been made to separate slags from silicon by utilizing the difference in electrical conductivity, but because of the high resistivity of silicon the method did not work [2]. In this thesis the mechanical separation techniques investigated are dense medium separation, optical separation and flotation. Dense medium separation utilizes differences in density as a separation criterion. By suspending fine powders of heavy minerals in water, the density of the suspension can be adjusted until it becomes intermediate to the density of slag and the density of silicon. As the lighter mineral floats, the dross can be removed. Optical separation uses reflectivity as a separation criterion. An image is taken by a digital camera, and a computer determines the composition of each particle based on the color, hue and intensity of the reflected light. Hydraulically operated flaps then separate waste from silicon. Flotation utilizes differences in surface chemistry between different minerals as a separation criterion. By adding specific flotation agents and adjusting the conditions of the separation, silicon can be separated from slag.

The metallurgical route also utilizes the density differences between slag and silicon as a separation criterion, but in the liquid state. As a mixture of slag and silicon is melted, the two phases will spontaneously separate due to surface tension. Assuming that there is a density difference between the phases, and that the intensity of stirring in the ladle is low, after a given holding time the lighter phase will float and the heavier phase will settle. It is then simply a matter of carefully decanting the floating phase and discarding the dross. In previous work by the author, the effect of holding time on the silicon yield has been investigated. It was found that the maximum holding time necessary in a small scale induction furnace was about 40 minutes [2].

Experiments with dense medium separation will be done with small samples (<100 g), as the method should be independent of the scale. The aim is to find the density range which will float either metallic silicon or slag. Optical separation experiments will be carried out manually at Comex labs by taking and analyzing static images of the charge. A preliminary flotation experiment will be done by measuring the zeta potential of slag and metal. Metallurgical separation will be carried out at 1600 °C in a small induction furnace, with and without slag additions to compare the effect of slag chemistry on separation efficiency and product quality. Chemical analysis of the products will be done by Elkem labs at Elkem Thamshavn and at Elkem Solar Research.

2 Theory

The aim of this project has been to evaluate various methods of separating silicon and slag. There are mainly two groups of separation methods: Mechanical separation based on low temperature reactions or physical properties, and metallurgical separation based on high temperature chemistry and qualities. All methods are based on the same basic principle of utilizing a characteristic property which varies widely between the two phases. In a previous project carried out by the author in the fall of 2010, an attempt was made to utilize the difference in electrical conductivity between slag and silicon as a separation criterion. Unfortunately, the difference in electrical conductivity proved too low for the available equipment, and no separation was obtained. The project also looked at metallurgical separation of slag and metal and attempted to quantify the holding time necessary to reach a steady-state concentration of silicon in the slag phase, with satisfying results [2]. The current project will look into other mechanical separation methods and continue the previous work on metallurgical separation. The new methods investigated were dense medium separation (DMS), optical separation and flotation. Metallurgical separation will be carried out with added fluxes at constant holding time. A theoretical background for each of the separation methods and for the slag system will be presented in the following sections. The last section of this chapter will go through theories and equations needed to dimension a slag remelting furnace and to choose a good lining concept for the furnace.

2.1 Mechanical separation of slag and freeze linings

The easiest and most common way of separating two minerals is by utilizing differences in density. The method has been used for millennia to separate minerals like gold, silver, galena (a heavy lead mineral) and cassiterite (a mineral based on tin). During the middle ages, processes were invented for separation of metal sulfides and other heavy minerals. Over the past century, gravitational separation has expanded to coal, chromite, rutile, ilmenite and many other important minerals, and is now the main separation method used for upgrading ores and removing shales [3].

The process has one crucial limitation however. The difference in density between the materials must be rather large for gravitational separation to be efficient. In order to quantify the necessary density difference, Digre, Malvik and Sandvik [3] introduces the gravitational potential, G .

$$G = \frac{\rho_h - \rho_f}{\rho_l - \rho_f} \quad (2.1)$$

The density of the heavy mineral is ρ_h , the density of the light mineral is ρ_l and the density of the separation medium is ρ_f , i.e. the liquid which the separation is carried out in. For separation of heavy minerals from light minerals, say hematite ($\rho_h = 5.2 \text{ g/cm}^3$) and quartzite ($\rho_l = 2.7 \text{ g/cm}^3$) in water ($\rho_f = 1.0 \text{ g/cm}^3$), the value of G will be large. A value of G above >2 has empirically been shown to give good separation of phases, according to Digre, Malvik and Sandvik [3].

$$G = \frac{5.2 - 1}{2.7 - 1} = 2.47 \quad (2.2)$$

Separating hematite and quartzite is thus easily done by gravitational separation in water [3]. Because the density of high-silicon slags and silicon is quite similar, separating silicon from slag is harder. As seen in Figure 10, the densities of slags in the $\text{Al}_2\text{O}_3\text{-CaO-SiO}_2$ system range from about 2.3 g/cm^3 to 2.7 g/cm^3 , and the density of silicon is 2.33 g/cm^3 at $25 \text{ }^\circ\text{C}$ [4]. This means that in the best

case scenario, the density difference is about 0.4 g/cm^3 . Assuming that gravitational separation was to be performed with water as separation medium, this would give a value for G of 1.28, which indicates poor separation capabilities. However, if the medium could be made to have a density intermediate to the density of the two minerals, the value for G could be adjusted to more or less any value. This is the principle for Dense Medium Separation (DMS).

2.1.1 Dense medium separation

DMS can employ any liquid with a density between the densities of the two desired separation products to increase the value of G. However, according to Burt [5] the liquid is in practice always a suspension of fine, magnetic particles in water. The reason for this is that there is an extensive list of demands for an industrial separation liquid. It should be available in quantity on site at relatively low cost, it must be noncorrosive, nontoxic and both physically and chemically stable in water. The liquid must also rinse easily from the product, be capable of regeneration and be adjustable over a range of densities [5]. The available true dense fluids are either poisonous organic liquids or enormously expensive polymers of dense metals. Examples include tetrabromoethane, which is both toxic by inhalation and environmentally dangerous [6], and diiodomethane, which is an irritant and toxic by ingestion [7]. Sodium polytungstate is a much safer option, but the cost is far too high for industrial applications [8]. As a result, all the industrial dense liquids are suspensions of magnetite or ferrosilicon (FeSi). These are preferred because they can be almost completely regenerated by using low-intensity magnetic separators, and because the working range is wide. Magnetite suspensions can reach densities of about 2.5 kg/dm^3 , FeSi can reach approximately 4 kg/dm^3 . In the case of separation of silicon from slag, elevated iron content in the product from imperfect rinsing of the product could pose a problem. This issue can be minimized by using more intensive water scrubbers or installing several scrubbers in series.

The ideal dense media suspension should have a low apparent viscosity, low yield stress and high stability. However, there is an inverse relationship between stability and yield stress, meaning that the settling time is inversely proportional to the stability of the fluid. Using finer particles in the suspension will increase the stability, but the viscosity of the suspension will also be increased. A compromise must therefore be made between having a stable liquid, i.e. fine particles, and an efficient process, i.e. coarse particles [3]. Whatever the grain size chosen, the viscosity of the suspension will increase exponentially to infinity after 20-40 vol% for any suspension [9]. The shape of the particles is of great importance, as round particles will have lower apparent viscosities at equal density compared to cubical or splintered materials. This is shown in Figure 1 for a range of FeSi particle sizes in water. The dotted line shows round, atomized FeSi particles in water, and it is clear that rounded particles are a prerequisite for high density liquids. The reason for this phenomenon happens is that round particles will tend to slide past each other much more easily than edged particles, giving a much lower resistance to fluid movement.

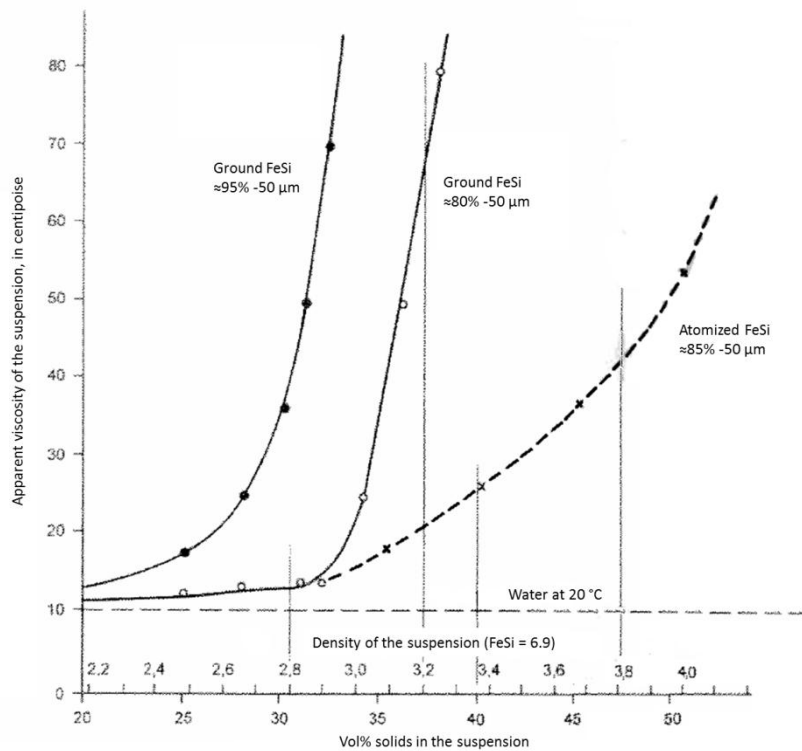


Figure 1: Apparent viscosity of medium suspensions as a function of vol% solids. [3]

The dense medium separation process can effectively separate particles with density differences of $<100 \text{ kg/m}^3$ in the size range of 4 mm to 500 μm [10]. The largest size is dictated by the separation vessel, the smallest size is dictated by medium rheology. By using centrifugal separators which can increase the force on each particle, and thereby increase the settling velocity, the lower limit can be pushed further to about 500 μm. Slime and fine particles under the lower value must therefore be removed before a DMS process, as they will stay in the suspension and pollute the medium [5]. As a separation method, it is therefore more of a system than a unit process. The feed must be prepared by sieving and de-sliming before mixing with the medium. The heavies and lights must be separated and rinsed, and the recovered medium must be recycled. A flow chart for the process is presented in Figure 2.

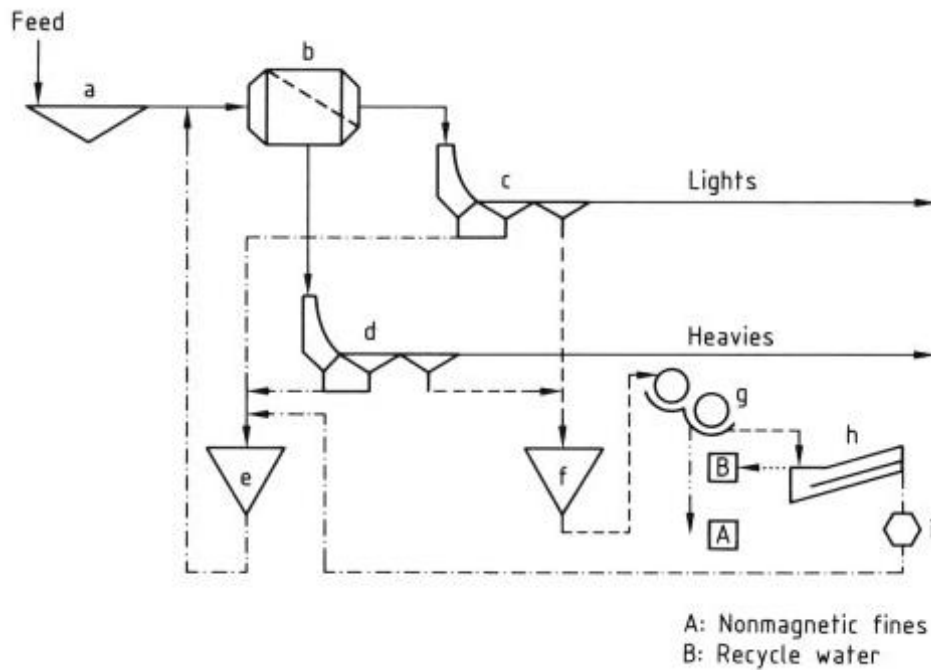


Figure 2: Flow sheet for dense medium separation.

a) Feed preparation screen; b) Heavy-medium separation; c) Lights drain –wash screen; d) Heavies drain –wash screen; e) Heavy-medium sump; f) Dilute heavy-medium sump; g) Magnetic separator; h) Densifier; i) Demagnetizing coil — Ore, heavies, lights; - - - - Heavy medium; ····· water. [5]

Evaluation of a given dense medium separation process is done in the laboratory using true dense mediums like tetrabromoethane, diiodomethane or sodium polytungstate in cyclones. By the use of true dense media, the settling time can be near infinite and even extremely small particles can be separated. Liquids covering incremental steps of density are prepared, and the sample is separated in the heaviest liquid first. The lights from this process is drained and transferred to the next lower density liquid and so on. The heavies from each liquid is drained, washed, dried and weighed. This gives the density distribution of the sample which, together with chemical analysis of the yield of each sink fraction, can give the washability curve for the sample [10]. Such a curve is shown for coal and ash in Figure 3, below. However, before a full washability curve analysis is done, which is both expensive and dangerous to personnel, it is important to know that the separation is viable at all. This is done using a single experiment where the density of the suspension is adjusted until a density is found where one fraction floats, and the other fraction sinks. If such a density cannot be found, the separation method is not viable, and a full washability curve analysis is unnecessary.

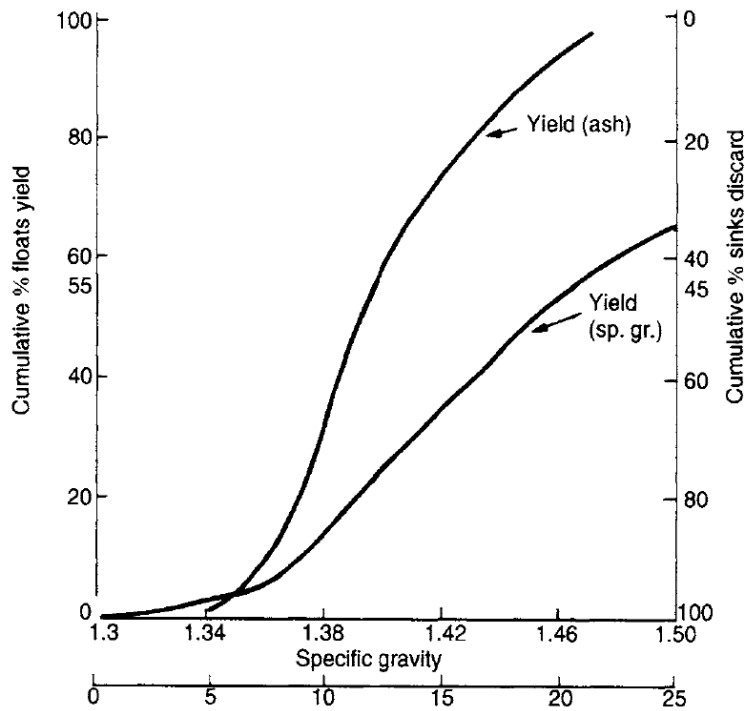


Figure 3: Typical coal washability curve [10].

2.1.2 Optical separation

Gravitational separation utilizes the density of materials as a contrast to separate two or more substances from each other. However, any physical or chemical trait which is sufficiently different between two materials can be used as a separation contrast. Silicon and slag have nearly identical densities; they are both insulators [11] and both materials are nonmagnetic, but the reflectivity of silicon is much larger than the reflectivity of slag. Metallic silicon has a shiny, metallic gloss and slag normally presents a dull finish with a green, brown or black color. Refractory material which is chiseled off with the freeze linings are white or gray with a dull finish, and the contrast between refractories and metal/slag is excellent. The three phases are shown in Figure 4.

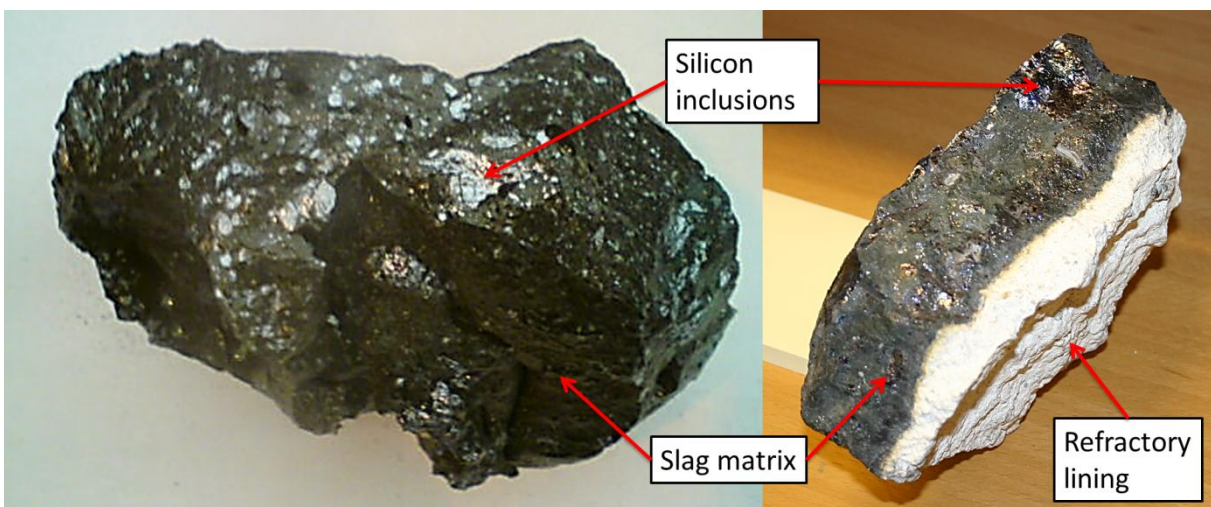


Figure 4: Off-grades

Optical separation utilizes the optical properties of the feedstock as separation criteria. According to Digre, Malvik and Sandvik [14], properties like color, reflection, shape, fluorescence, thermal radiation and translucency with regards to any part of the electromagnetic spectrum can be used as separation criteria. As long as the minerals can be excited in some way which gives unique feedback for each mineral, optical separation is a viable option. An optical separator works by taking pictures of the charge, analyzing them and then selectively removing particles based on a given set of criteria. The efficiency of the separation depends on the particle size and the accuracy of the given separation criteria, which are normally threshold values for identifying phases. Smaller particles will reduce either the capacity of the separator or the accuracy, as the work done per ton is increased. It is therefore common to remove the finest particles before separating, which could lead to a significant loss if the charge is very brittle [3]. The physical separation of particles is done either by air nozzles which propel small particles, or pneumatic flaps for large particles. An example of a modern optical separator is the OSX separator series produced by Comex. An overview of their OSX separator series is shown in Figure 5. According to their data the selectivity of the optical separator ranges from 70 to 99 % [12].

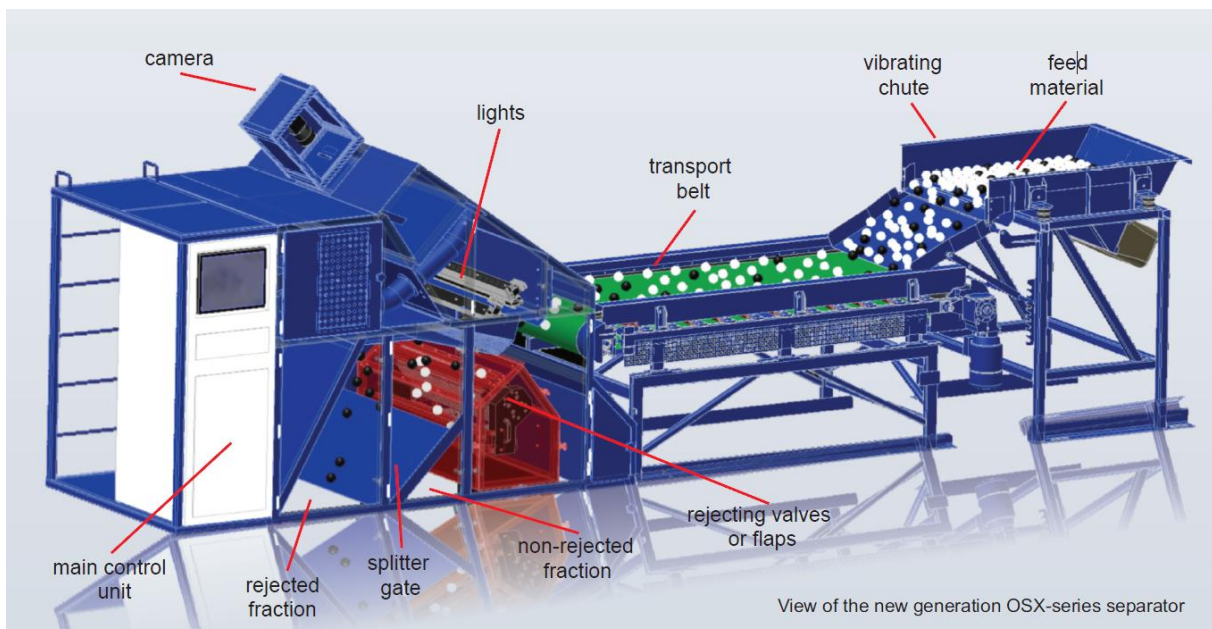


Figure 5: The Comex OSX optical separator [13].

2.1.3 Flotation

The basic principle of flotation is to make certain minerals in a solution float while other minerals sink. According to Digre, Malvik and Sandvik [3], this is achieved by adding flotation chemicals which adhere to certain surfaces and foam off during stirring or bubbling. As all minerals are composed of different species and/or have different structure, the surface chemistry will be slightly different from one mineral to the next. It is therefore an important separation criterion which can be utilized in flotation processes. By carefully designing the process, valuable minerals can be selectively floated from the shale and treated further. The added chemicals are called flotation agents, and work by having an electrically charged (polar) part which adheres to the surface of the mineral and another which is organic, and therefore aerophilic/hydrophobic. The hydrophobic part of the molecule is

lighter than the surrounding liquid and adds buoyancy to the particle. If enough agents adhere to the surface, the particle will float and can be skimmed off. Adhesion of the agents to the particle is shown in Figure 6, below.

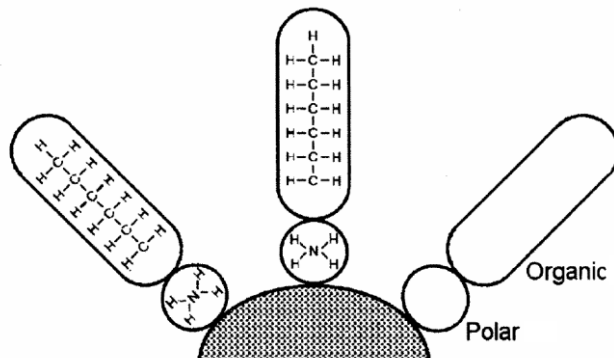


Figure 6: Sketch of flotation agents on a mineral surface [3].

Separation by flotation requires that the difference in surface properties between two minerals is sufficiently large, so that an added agent will stick to one of the surfaces, but not the other. This can be quantified by the zeta potential; the electric potential between the interface of a particle and the bulk fluid. A large difference in zeta potential between two materials indicates that a flotation process will be effective, because added flotation agents will adhere differently to differently charged surfaces. The zeta potential is formed as a result of attraction to the surface of dissolved ions and polar molecules, and it can be manipulated by varying the chemical composition of the solution. Because the surfaces of various minerals are different, the change in the zeta potential for each species at a given change in pH or composition can be different. By carefully manipulating pH and ion content of the solution, a very high degree of specificity can be achieved. This is shown in Figure 7 for separation of quartz and feldspar, a common industrial process. In basic solutions, the zeta potential of the materials is equal, and a flotation process will be inefficient. In solutions with a pH of about 2-3, the difference is large, so agents with a positive polar part are much more likely to adhere to feldspar than quartz, giving an effective flotation process.

An example of how surface activators can enable flotation can be found for flotation of sphalerite (zincblende, zinc sulfide). Sphalerite is poorly attracted to the flotation agent xanthate, which is often used to separate chalcopyrite (CuS) from sphalerite and pyrite (FeS_2), as these three minerals often appear together. When all of the chalcopyrite has been removed, copper sulfate (CuSO_4) is added to the mix. Copper ions from CuSO_4 will then switch places with zinc in the sphalerite mineral, and because copper is strongly attracted to xanthate, the process is suddenly viable for flotation of sphalerite as well [3]. Designing a flotation system is therefore a matter of finding the right combination of flotation agents, pH and surface activators which will act on one of the materials but not the other. Because of the many variables, designing a flotation process is often very time consuming, and often requires an approach based on educated guesses and frequent trial-and-error.

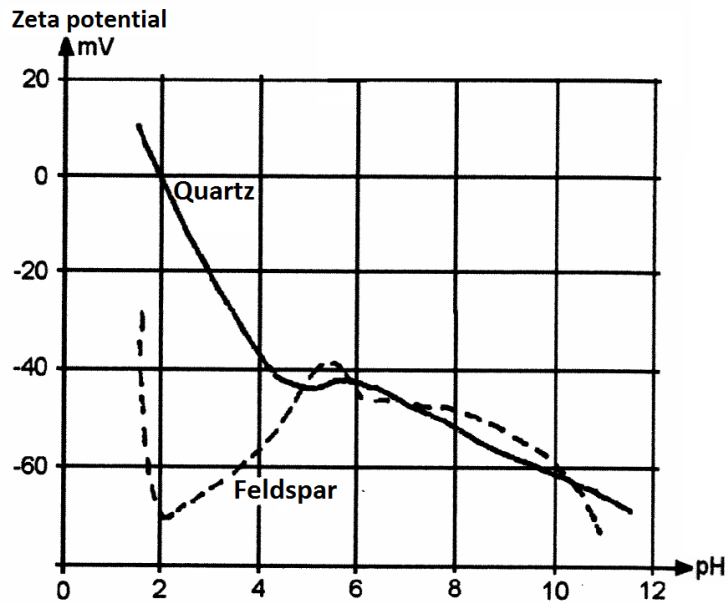


Figure 7: Zeta potential of feldspar and quartz as a function of pH [3].

2.2 Remelting and settling of slag and freeze linings

Settling of metal from slags is a regular operation in all metallurgical industry. Yet when this is done in most industries, the metal and slag normally comes straight from the furnace in a molten state, and separation of the two phases is a minor issue. In production of manganese e.g., the metal is significantly denser than the slag, which means that the metal quickly forms a bulk phase underneath the slag. By careful pouring, the slag is easily removed [14]. However, remelting high-silicon wastes to separate slag and silicon is a different scenario altogether. The density of the slag is almost equal to the metal, pouring the slag is difficult because of its extreme viscosity, stirring of the melt can entrain particles back into the slag and silicon is reactive towards oxygen in the atmosphere. In order to overcome these difficulties, it is important to find the optimal operating conditions and slag compositions for effective settling. It is important to keep in mind that a slag-metal equilibrium will be in place at all times, so when fluxes are added to the slag phase, the composition of the silicon phase will change.

2.2.1 The Al_2O_3 - CaO - SiO_2 slag system

There are three main species in slag from a silicon furnace; Alumina (Al_2O_3), lime (CaO) and silica (SiO_2) [15]. These will enter the system through the various charge materials. The source of silicon in the electric arc furnace is quartz, SiO_2 . Most of the quartz is reduced in the furnace to metallic silicon, but some quartz will remain unreacted and will exit the furnace as slag. Alumina enters the furnace mainly as impurities in quartz and in the reduction materials, which are coke, coal and wood chips. CaO is present as an impurity in the charge as well, but additional lime is also added to the system to control the slag composition and give an on-spec silicon product. Most of the Al_2O_3 and CaO will end up in the slag phase. The phase diagram for the SiO_2 - CaO - Al_2O_3 system is given in Figure 8.

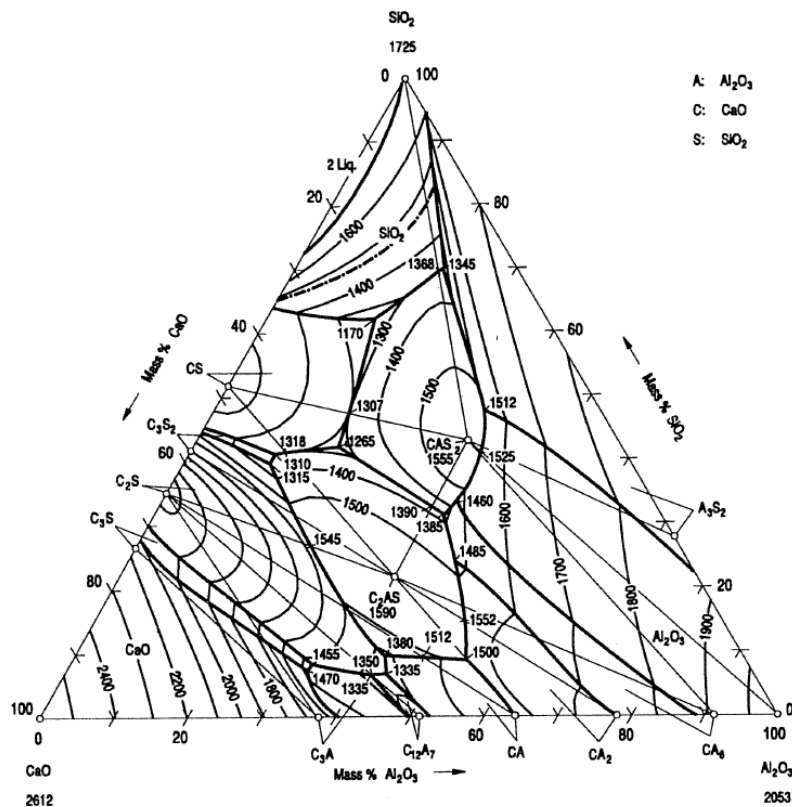


Figure 8: The Al_2O_3 - CaO - SiO_2 system [15].

At the high temperatures involved in settling of silicon (1500 – 1600 °C), reactions normally happen so fast that the slag and the metal is continuously in equilibrium [16]. This means that the impurity content of the metal depends directly on the composition of the slag. Schei, Tuset and Tveit presented work by Haaland, where the content of Ca and Al in metallic silicon was given for any given slag composition in the Al_2O_3 - CaO - SiO_2 system [1]. This diagram is shown below in Figure 9, and it can be seen that controlling the slag composition is essential to controlling the impurity levels of the metal. As seen in the diagram, the higher the CaO and Al_2O_3 content of the slag, the more Ca and Al impurities there will be in the produced silicon. Many consumers demand low values of these contaminations, so therefore an oxidative refining step is almost always introduced before casting the silicon. The refining is carried out by blowing oxygen-enriched air through the melt. Because aluminium and calcium both have a high affinity for oxygen, they are easily oxidized and selectively removed from the melt as oxides, which then enter the slag phase [1].

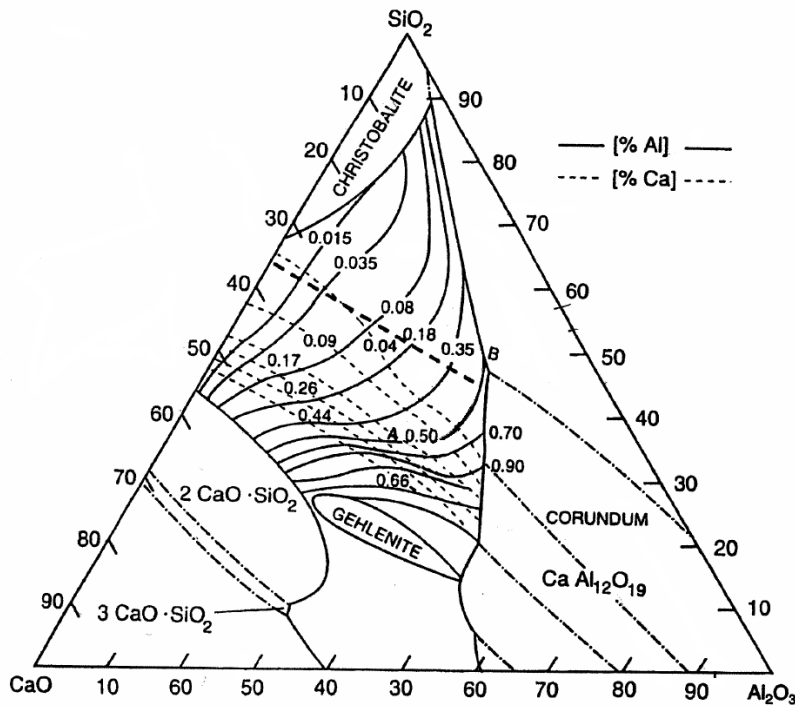


Figure 9: Content of Al and Ca in the produced metal as a function of slag composition [1].

2.2.2 Density

The density of the slag is important in a settling process because the produced metal must be separated in some way from the slag, preferably by simply pouring the lighter phase off. Controlling the density of the slag is done by addition of dense or light species to the slag. Figure 10 gives isodensity curves for the Al_2O_3 - CaO - SiO_2 system at 1550 °C. It is clear that slag density is nearly independent of Al_2O_3 , and increases with increasing CaO content. The slag composition marked in the figure has been found by X-Ray Fluorescence spectroscopy (XRF) of slag from Elkem Thamshavn. The density of liquid silicon at 1550 °C is calculated by Schei, Tuset and Tveit to be 2.47 g/cm³ [1], which will be the pivot point between a sinking and a floating slag. This is represented by the line in Figure 10. The slag composition found shows that the slag is lighter than the silicon, and will therefore float. As the slag density displaces from the pivot, the settling speed increases. This is shown in the Stokes' equation for Reynolds number $\text{Re} < 2$ [16]:

$$u_r = \frac{2\Delta\rho g a^2}{9\rho\nu} \quad (2.3)$$

This equation gives the terminal velocity, u_r , for a given difference in density, $\Delta\rho$, between a spherical inclusion of radius a and density ρ , and a liquid with kinematic viscosity ν . This equation, which holds for both liquid and solid inclusions, assumes that only gravitational forces apply to the inclusion, the Reynolds number is always below 2 and all inclusions are spherical. The implication of equation (2.3) is that the slag should preferably have as large a density difference, $\Delta\rho$, as possible compared to the silicon, and the slag should have as low viscosity as possible. This will ensure an efficient settling of the metallic inclusions. One way of doing this is by adding lime to the melt. As seen in Figure 10; by going from the current slag density (the cross) and adding lime, the density of the slag would increase until it becomes heavier than the silicon. The lighter silicon could then be poured off after

settling, while the remaining slag is discarded. As will be explained in detail in the next chapter, adding lime will have the co-benefit of reducing the viscosity as well.

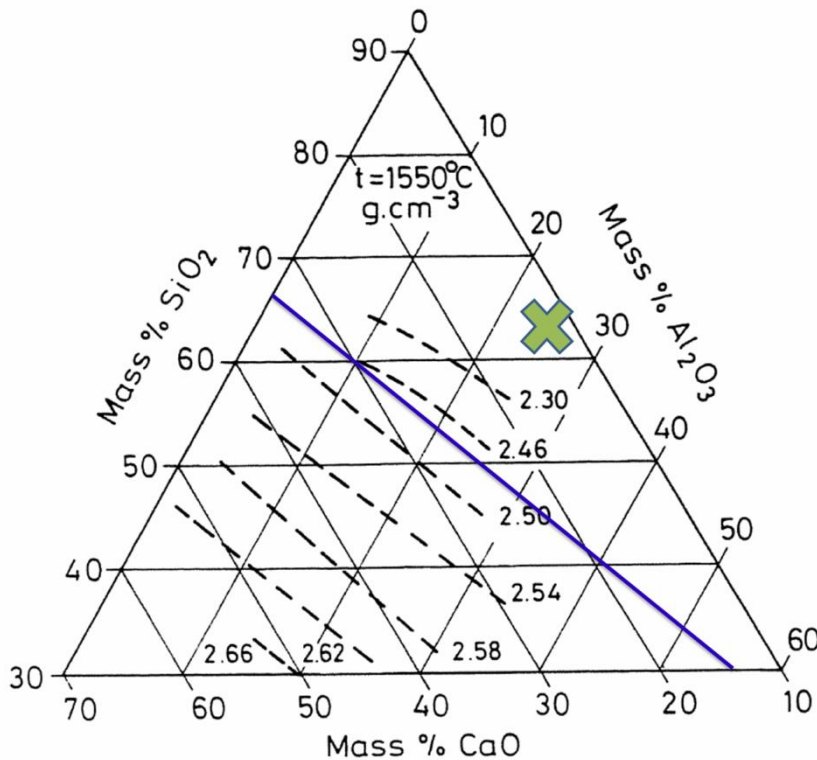


Figure 10: Isodensity curves (in g/cm^3) for the $\text{SiO}_2\text{-CaO-Al}_2\text{O}_3$ system [15]. The cross marks the composition of the slag in the off-grades used in the remelting experiments. The blue line designates the approximate density of silicon at 1550°C .

Magnesia (MgO) could also be added to a settling furnace as a way to increase the density. Lime and magnesia are almost equally dense at 1600°C . This can be seen in Figure 11, below. Ranging from 10-20 wt% MgO in the slag, the density dependence on SiO_2 is about the same.

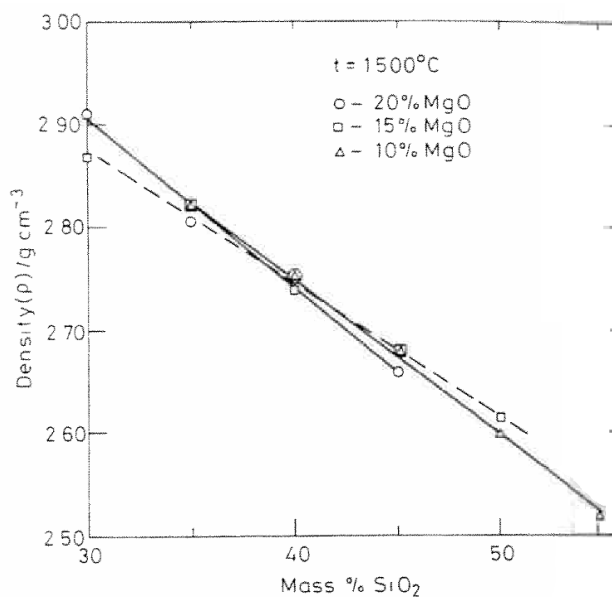


Figure 11: Density of the $\text{Al}_2\text{O}_3\text{-CaO-MgO-SiO}_2$ system as a function of MgO and SiO_2 content [15].

Adding about 5-10 wt% MgO to the slag will have the additional benefit of decreasing the melting point of the slag, as shown in Figure 12. That means that settling can be done at a lower temperature. At lower temperatures there is less wear on refractories and equipment. However, the possibility of MgO addition is quite limited, because of the many high-melting areas in the (30 wt% Al_2O_3)- CaO - MgO - SiO_2 system. One way of adding MgO is through the addition of dolomite, $\text{CaMg}(\text{CO}_3)_2$. This would introduce both MgO and CaO into the slag, giving a denser slag with a lower melting point, at the same time as the viscosity is lowered.

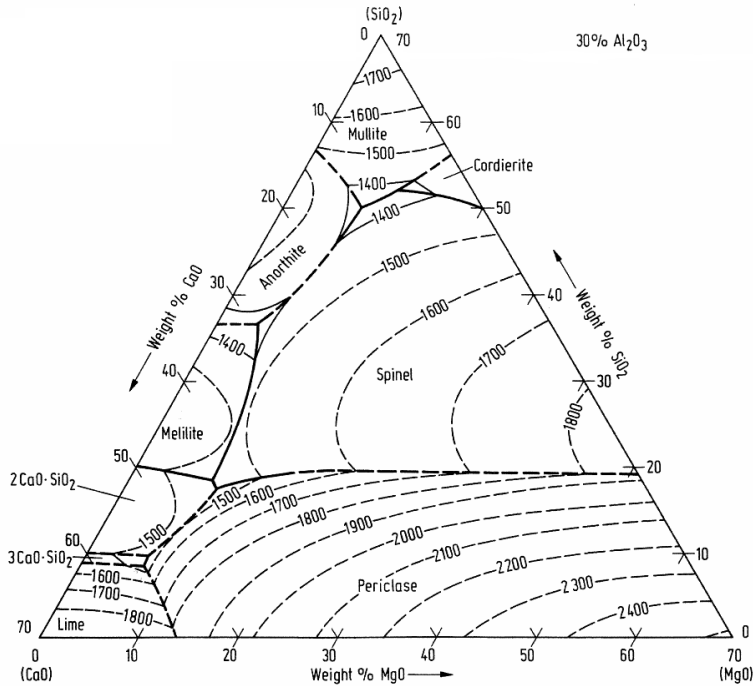


Figure 12: Phase diagram for 30% Al_2O_3 - SiO_2 - CaO - MgO [15].

2.2.3 Viscosity

The viscosity of the slag is crucial to the settling speed of the metal as it represents resistance to fluid motion. According to Engh [16] viscosity can be explained as the reciprocal of fluidity, i.e. a viscous fluid will flow very slowly when a force is applied. A highly viscous slag will therefore inhibit the motion of metallic silicon droplets within the slag, causing inefficient settling. Isoviscosity curves of the SiO_2 - CaO - Al_2O_3 system are given in Figure 13, and the slag composition found in off-grades is shown with a cross. The indicated value of between 500 – 800 poise is extremely high. Compared that to say, pine honey (also known as wood pitch or resin), which is a common fluid known for its viscosity, the slag is 2-5 times as viscous. Pine honey has a viscosity at room temperature (25 °C) of just 208 poise [17]. It should now be intuitively evident that extreme viscosity will hamper the motion of liquid metal.

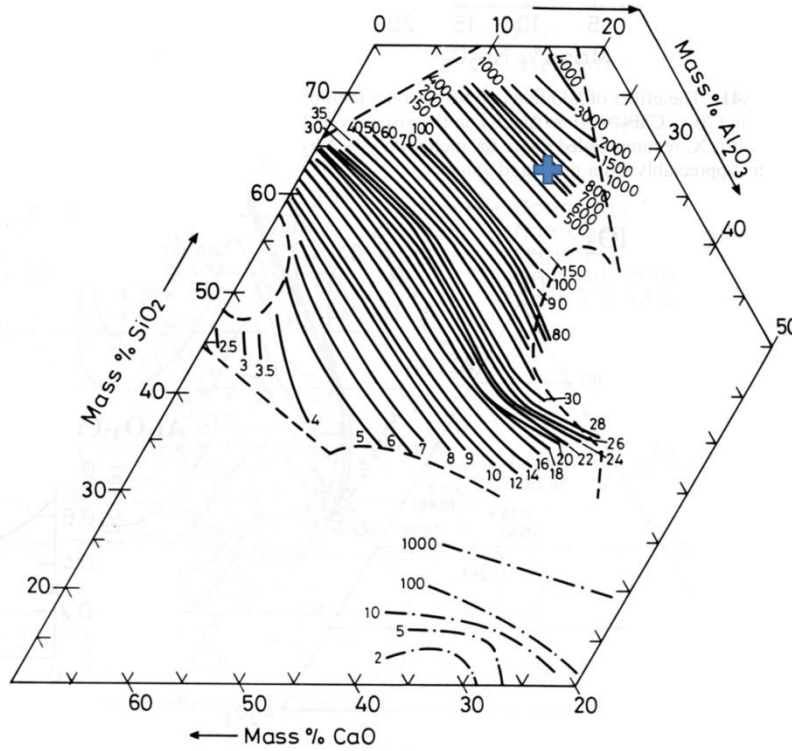


Figure 13: Isoviscosity curves for the Al_2O_3 -CaO- SiO_2 system at 1500 °C, [15]. Values in poise (0.1 Ns/m^2). The cross marks the composition of the slag in the off-grades used in the remelting experiments.

As seen in the figure, increasing amounts of the acidic specie SiO_2 will drastically increase the viscosity of the slag. This is because SiO_2 forms large scale 3-dimensional networks of oxygen-bonded SiO_4^{4-} throughout the slag [16]. SiO_2 is called an acidic specie as it removes free oxygen ions (O^{2-}) from the melt, just like introduction of an acid into an aqueous solution will consume negatively charged OH^- ions. Introducing basic slag components like CaO or MgO will break oxygen bonds in the network, reducing the amount of bonding in the melt and therefore reduce the melt viscosity. They are classified as basic because they contribute O^{2-} ions, like bases will in aqueous solutions. An attempt has been made in Figure 14 to visualize how this might look like in a silicate melt. CaO has been added; it has donated oxygen to the system, and it has broken some of the silicate bonds in the slag. Adding dolomite ($\text{CaMg}(\text{CO}_3)$) or limestone (CaCO_3) would therefore reduce the viscosity, increasing the settling speed.

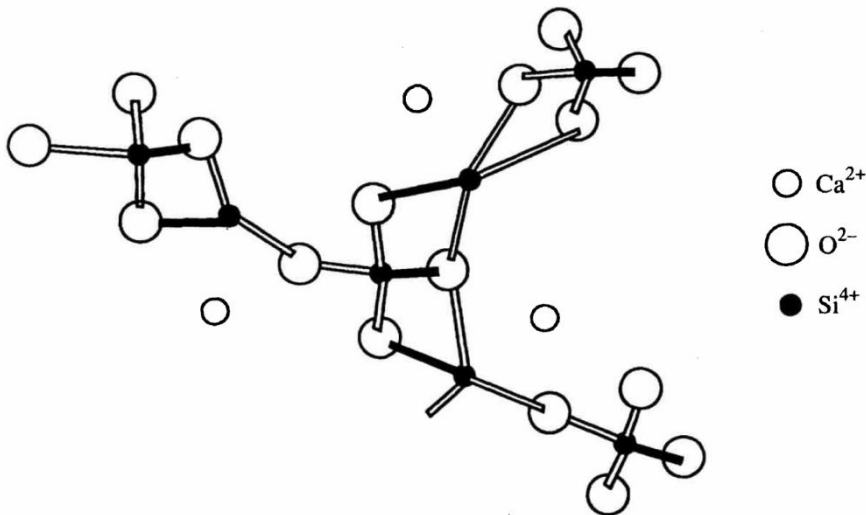


Figure 14: Silicate chains in slag partly broken by CaO [18].

2.2.4 Surface and interfacial tension

The phenomenon of surface tension is responsible for the ability of almost all liquids to spontaneously form droplets. Interfacial tension is the reason why a mixture of oil and water will separate into two separate phases with a clear boundary in between. The terms interfacial tension and surface tension are actually interchangeable, as they are the same phenomenon, but surface tension is normally reserved for liquid – gas interfaces. Interfacial tension in liquids arises from a difference in attractive forces between the molecules of the surface and those of the bulk. This is shown schematically in Figure 15. A molecule in the bulk is surrounded on all sides by equal molecules with an equal attraction to each other, resulting in zero net force. However, the surface molecules normally experience much less attractive force across the phase boundary than to neighbouring molecules. This creates a net inward force which behaves like a thin elastic membrane in a state of tension [15]. Interfacial tension is of vital importance in settling because the tendency for metal to form droplets, which subsequently coalesce and become a part of the bulk phase, is responsible for the spatial separation of phases. If the interfacial tension is near zero, for example like it is in milk (an emulsion), inclusions will stay dispersed in the liquid. No separation is then possible, which is why fat in milk does not spontaneously separate from the water, giving two separate phases. The definition of surface energy, σ , according to the Gibbs surface model is [19]:

$$\sigma = \left(\frac{\partial U}{\partial A_s} \right)_{S, V^\alpha, V^\beta, n_i} \quad (2.4)$$

The surface tension is given as σ , the internal energy of the system is U , A_s is the area of the interface, S is the entropy of the system, V^α and V^β are the volumes of each phase and n_i is the total number of molecules in the system. Parameters in subscript are assumed constant in the calculation. This equation basically states that surface tension arises from the need to minimize the internal energy of the system. Any exposed surface constitutes an increase in internal energy, which will be minimized by forming spherical droplets. When these coalesce, the total surface is further reduced, until a separate bulk phase is formed. The SI unit for surface tension is N/m, which is equivalent to the energy needed to increase the surface of a droplet by a unit area J/m^2 . According to the Slag

Atlas [15], thermodynamic data on interfacial tension will always relate to equilibrium conditions. Any reactions or mass transfer across the interface will quickly reduce the interfacial tension. If the reaction rate is sufficient, the tension will even drop to zero or negative values, leading to spontaneous mixing of phases.

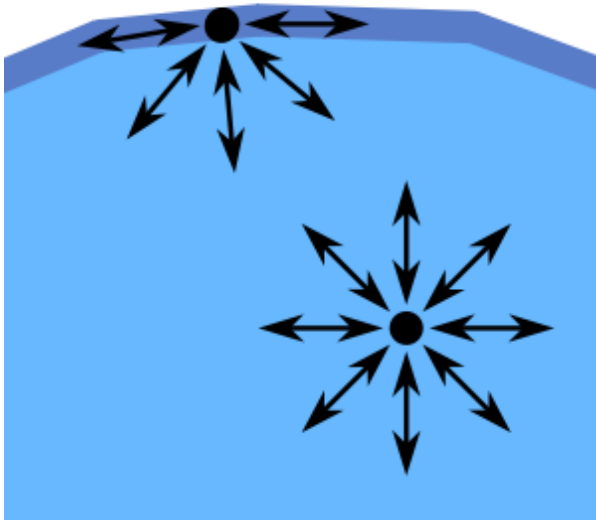


Figure 15: Schematic overview of surface tension ^[20]

The two principal parameters affecting interfacial tension are temperature and composition. With a few exceptions, all liquids exhibit a negative temperature coefficient for interfacial tension [15]. As the temperature increases, the liquid approaches the critical temperature and the intermolecular attractive forces in the bulk are reduced until they equal the surrounding media. The critical temperature is defined by Stølen and Grande [19] as the temperature where the miscibility gap between phases disappears. The forces acting on the surface molecules disappear, giving no net inward attraction, i.e. no interfacial tension [21]. Above the critical temperature, there is therefore complete miscibility between the two liquids. The temperature dependency of surface tension for a liquid-gas (lg) interface can be written as [19]:

$$\sigma^{lg} = \sigma_0^{lg} \left(1 - \frac{T}{T_c}\right)^n \quad (2.5)$$

The factor σ_0^{lg} refers to the surface tension at 0 K. The exponential factor n is found to be around 1.2 for metals [19].

In order to quantify the tendency for a slag to cover the surface of a metal, Schei, Tuset and Tveit introduces the spreading coefficient, $S_{s/m}$ [1]:

$$S_{s/m} = \sigma_{g/m} - (\sigma_{g/s} + \sigma_{s/m}) \quad (2.6)$$

The surface tension of the metal is $\sigma_{g/m}$, the surface tension of the slag is $\sigma_{g/s}$, and $\sigma_{s/m}$ is the interfacial tension between the slag and the metal. As long as the spreading coefficient is negative, there will be a net inward force for each of the phases. Given adequate time for settling, the phases will spontaneously separate and form a bulk metal phase and a bulk slag phase.

B.J. Keene [22] has conducted a thorough review of the surface tension of silicon from previous works, and suggested that the surface tension of *pure* metallic silicon, $\sigma_{g/m}$, is 860 mNm^{-1} at $1550 \text{ }^\circ\text{C}$. However, the same article visualizes the large differences in surface tension when silicon is even slightly contaminated with other metals and oxygen. Typically, metallurgical grade silicon will contain about 0.03 % Ca, 0.3 % Al, 0.2 % Fe and up to 0.035 % Ti. Ca impurities in the metal and oxygen in the furnace atmosphere will reduce the surface tension of silicon. Fe and Ti will somewhat tend to increase surface tension, but according to Keene this effect will be negligible compared to the effect of oxygen. The surface tension of silicon, $\sigma_{g/m}$, from freeze linings is therefore assumed to be 730 mNm^{-1} for settling at $1550 \text{ }^\circ\text{C}$.

Inserting values of $\sigma_{s/m} = 500 \text{ mN/m}^{-1}$, $\sigma_{g/m} = 730 \text{ mNm}^{-1}$, and $\sigma_{g/s} = 500 \text{ mN/m}^{-1}$, found in literature for the slag composition found by XRF analysis, gives a spreading coefficient for freeze linings of -270 mN/m^{-2} at $1550 \text{ }^\circ\text{C}$ [23]. Silicon should therefore spontaneously separate from slag, provided long enough settling time for inclusions to meet, coalesce and reach the bulk metal phase. If CaO is added to the slag, for example through dolomite, the surface tension of the slag will increase, leading to an even better (more negative) spreading coefficient.

2.2.5 Melt stirring speed

During the initial phases of settling, stirring is beneficial. This is because the fluid flow increases the likelihood of silicon droplets meeting each other and coalescing into larger drops, which will then enter the bulk metal phase. However, a high stirring speed of the melt can cause particles to become re-entrained into the slag. This can happen in an induction furnace, where the magnetic field creates a flow in the crucible, or in an electric furnace if there is stirring e.g. by gas blowing. According to Engh [16] the critical velocity, v_b , for a given spherical inclusion to be re-entrained into the slag is:

$$v_b < \left(\frac{4\Delta\rho g a x^{1/5}}{0,09\rho v^{1/5}} \right)^{5/9} \quad (2.7)$$

The difference in specific weight between the slag and the metal is $\Delta\rho$, gravity is given by g , a is the droplet radius, x is the reactor radius, ρ is the specific weight of silicon and v is the kinematic viscosity. A plot of equation (2.7) is given in Figure 16. Values used to calculate the plot are $\rho_{\text{Si}} = 2470 \text{ g/cm}^3$, $\rho_{\text{slag}} = 2540 \text{ g/cm}^3$, $v_{\text{slag}} = 3.22 \cdot 10^{-7} \text{ m}^2/\text{s}$ and $x = 1 \text{ m}$. The figure gives the bulk velocity where particles that are smaller than a certain size will be re-entrained in the slag. A high stirring rate will therefore increase the likelihood of an inclusion reaching the bulk metal phase, but reduce the total settling potential of the mix, i.e. the total amount of metal available for extraction. This can be combined in a resistance furnace to minimize the settling time needed while maximizing the yield. If the mix is first stirred by a bubbling through a lance to make droplets coalesce, and then allowed to settle without stirring, the best of both worlds can be achieved.

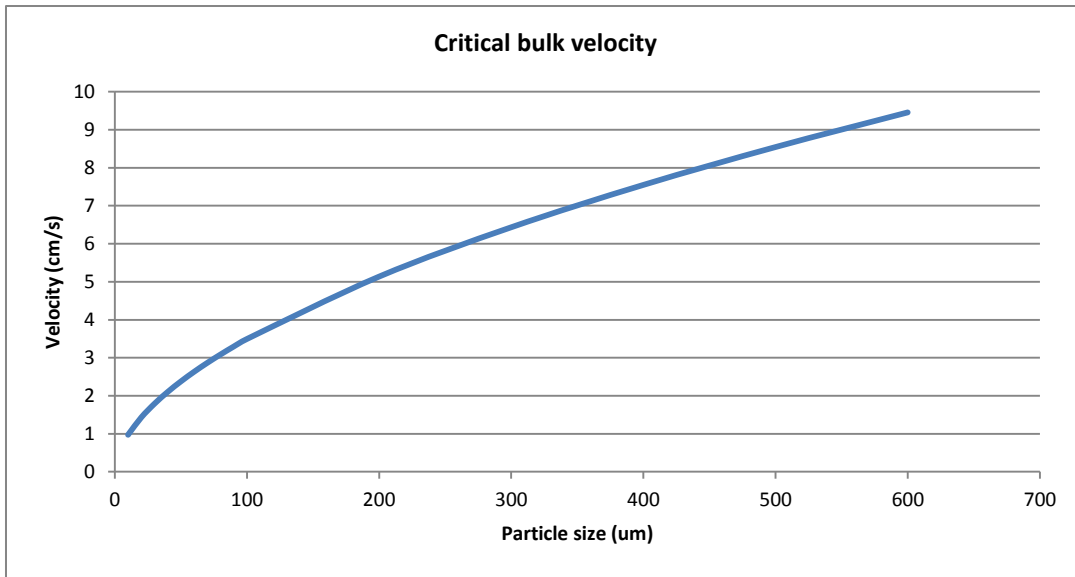


Figure 16: Critical bulk velocity for re-entrainment of droplets

2.3 Furnace design

Remelting off-grades at Elkem Thamshavn to extract silicon by settling would have to be done either in a separate remelting furnace, or by reintroducing the off-grades in some way to the process. Recycling off-grades would however eventually lead to a build-up of slag components in either the furnace or the ladle, and one way or another an output for process slag would have to be arranged. Besides, as will be calculated in chapter 4.3.1 Heat balance, the superheat from the silicon furnace is unlikely to be sufficient to melt the annual production of off-grade material. It is therefore fair to say that remelting high silicon wastes at Elkem Thamshavn would require the installation of a new furnace at the plant. In order to reach the melting temperature of silicon and slag, without producing large amounts of CO₂ and other polluting off-gases from burning carbon materials, there are only two kinds of furnaces available: The electric arc furnace and the induction furnace.

Electric arc furnaces produce heat when an electric arc is sent from an electrode through the charge material. It is a well-established method which has been in use for production and refining of metals for decades, amongst others for the production of silicon. However, electric arc furnaces are not ideal for remelting of slag. They deliver their power in a focused manner, superheating the areas which the arc plays over, meaning that the heat has to dissipate from the electrode tip to the extremities of the work piece. For remelting purposes, it is better to have a more uniform heat distribution. Also, the electrodes are normally made of graphite, which could break off during use and potentially ruin the batch.

Induction furnaces work by inducing eddy currents in a work piece, i.e. the heat is produced within the piece itself, not by an external source. This gives a very quick response to power adjustments, high power densities and good heating efficiency. There are no flue gases produced from the furnace itself, and the process can be done without introducing any contaminations to the slag. Moreover, an induction furnace is versatile, as the operator can alter the heating pattern by changing the inductor frequency [24]. The following chapter will therefore look further into the theory and application of induction furnaces for remelting of silicon, and equations will be presented for dimensioning a remelting furnace for off-grade material.

2.3.1 The induction furnace

The theoretical basis for the induction furnace was found by Heaviside in 1884 [25], as he and the other prominent pioneers of electromagnetism studied the heating effect observed in electrical transformers. He used a solenoid to heat an iron core, which could then transfer heat to a surrounding media. The first record of a deliberate use of a solenoid with an inductive charge as the secondary coil is from Schneider in 1904 [26], who used a combination of induction and electric arcs to generate a liquid metal pool. In 1916 an American called Dr Northrup, started investigating the practical issues of building industrial induction furnaces [27]. This first resulted in the Wyatt-Ajax industrial furnace and later in the first generator-driven induction furnace [28]. From here, the coils have grown larger, the heat intensity has increased and large advances have been with regards to refractory material, off-gas handling etc. but the overall design of the induction furnace remains largely unchanged.

The induction furnace works by generating large eddy currents in a material by running an oscillating current through a solenoid copper coil wrapped around the material. The primary coil generates a strong magnetic field, which induces an electric current according to Lenz's law [29]. As the current

(I) passes through the material, electric energy will dissipate as heat (P) because of the resistance of the material (R). The amount of heat generated is given by Joule's law, which states that the ohmic heating is proportional to the square of the current times the resistance:

$$P = I^2 R \quad (2.8)$$

However, the induced current is not evenly distributed through the work piece, because of what is known as the *skin effect*. This is best visualized by imagining a round metal bar being heated by a solenoid [30]. If the bar is divided into thin, concentric sleeves of metal, the outermost sleeve would feel the strongest magnetic flux from the coil. This would induce a current in the sleeve, which would act as the primary coil for the second sleeve. As energy is dissipated as heat in the first sleeve, the induced current in the second sleeve must logically be lower than in the first sleeve. The third sleeve will then experience a lower induced current than the second and so forth, until the center of the work piece is reached. As the initial current from the solenoid progresses into the metal, there is both a phase displacement and a radial variance in current density, which results in a magnetic penetration depth, the skin depth δ [29], given by equation (2.9).

$$\delta = \sqrt{\frac{2\rho}{\omega\mu_0\mu_r}} = \sqrt{\frac{\rho}{\pi f\mu_0\mu_r}} \quad (2.9)$$

The magnetic permeability of vacuum is μ_0 , the relative magnetic permeability of the material is μ_r , the resistivity of the material is ρ , and the angular frequency is ω , which equals $2\pi f$, where f is the absolute frequency of the generator AC current.

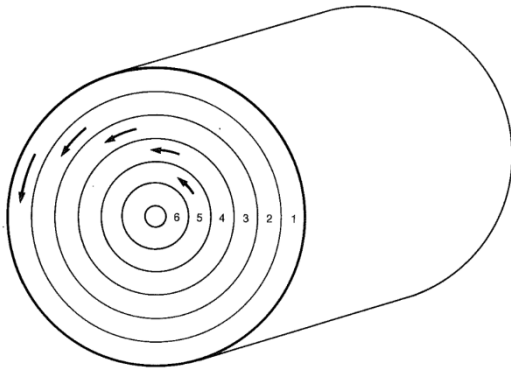


Figure 17: A metal bar in an induction coil showing the magnitude and the phase shift of the induced eddy currents in the bar [30].

As the frequency increases, the angular displacement between each sheet is increased, which increases the current density gradient. This means that the outer sheet carries a larger part of the current as the frequency increases, analogous to an increase in the number of sheets. At constant potential and current through the outer coil, the induced current in the inner coil is also constant even though the frequency is increased. The effective cross-section area (A) of the conductor therefore decreases and a large increase in resistance is the result [29]. The average circumference of the current sheet (l) will also increase, but the effect is negligible compared to the reduction in area.

$$R = \rho \frac{l}{A} \quad (2.10)$$

Varying the frequency will give the operator of an induction furnace the option of using high frequencies to superheat an outer sleeve of the work piece, or low frequencies to heat the work

piece through the whole of the volume. This is important when trying to melt silicon, because of the low conductivity of cold, solid silicon [28]. Silicon is a semiconductor, which means that its resistivity is intermediate to a resistor and a conductor. Its resistivity decreases as a function of temperature, which is opposite to the trend in metals. At room temperature, silicon has a resistivity of approximately $6.4 \cdot 10^2 \Omega \cdot \text{m}$ [31], which is very high compared to the common value for most metals of $10^{-7} - 10^{-8} \Omega \cdot \text{m}$. With such high resistance, creating eddy currents in the material is almost impossible, giving a very low efficiency of heating. The situation is worsened by the fact that the charge is added as separate grains, not as a continuous mass. Gaps between grains add to the resistance of the system, giving a very high apparent resistivity of the charge. It could therefore be necessary to introduce a graphite susceptor which would help heat the silicon until it can sustain eddy currents, or pour fresh, liquid silicon from the furnace onto the off-grades to pre-heat the charge and create contacts between grains. Liquid silicon has a much lower resistivity, at just 10^{-6} [32], and could therefore sustain eddy currents. Another option is to use graphite or SiC as lining material so that the lining itself is a susceptor. Heat transfer would then have to occur from the crucible wall to the charge, which would reduce the thermal efficiency of the system somewhat. In addition, if the lining is to be used as the heater, the hottest part of the furnace would always contact the coldest part, i.e. the cooled copper inductor, and the extra heat loss through the walls could be significant. Determining the optimal setup would have to involve modeling the different solutions and finding the thermal efficiency. This is outside the scope of this thesis however, so only solutions for the electromagnetic parameters of the system will be given.

2.3.2 Furnace design

The total production of off-grade material at Elkem Thamsavn is approximately 5160 tons/year. As mentioned several times before, the silicon content of off-grade materials will vary widely. The annual average of sold off-grades is estimated by Elkem engineers to at least 40 wt%. Analyses done in previous work by the author showed an average of 42 wt% silicon in freeze linings [2], and analyses done in this project has found an average of 49 wt% silicon in slag, see chapter 4.2 Remelting experiments. A remelting furnace must be dimensioned so that it is able to process all the off-grades in a reasonably short time, at a high efficiency. However, it should not be bigger than necessary in order to keep investment costs down.

The following derivation of equations for designing a silicon remelting furnace is based on work by Kennedy et al. [33], with references to other authors when applicable. Their work covers design methods for aluminium billet heating with induction coils, but since the equations presented in the article are not specific to the charge material, they can also be applied to melting and settling of off-grades. However, as mentioned above, the resistivity of silicon at low temperatures is very high, so the melting process would have to start with a molten sump or with inductive refractory lining, i.e. graphite or SiC. The overall geometry of the furnace has been based on work by Ahmed, Masoud and El-Sharkawy [34]. In their article, geometrical and electrical parameters were found for a 4 ton capacity induction furnace for melting iron. Figure 18 shows the cylindrical induction furnace design proposed by Ahmed, Masoud and El-Sharkawy. Figure 19 shows a 10 turn induction coil for aluminium billet heating, as proposed by Kennedy et al.

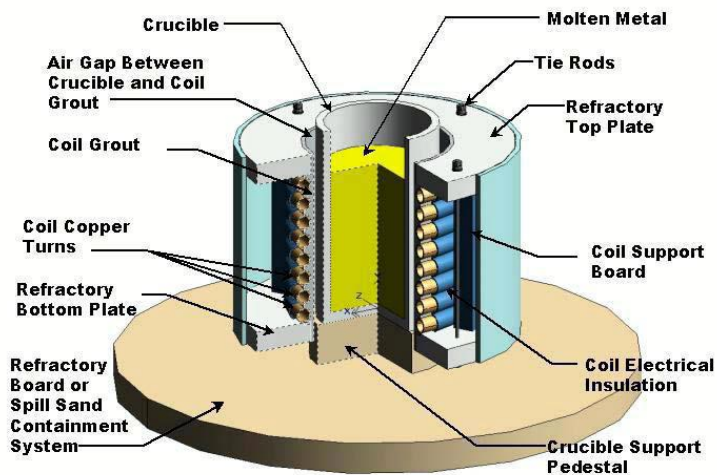


Figure 18: Sketch of the induction furnace proposed by Ahmed, Masoud and El-Sharkawy.

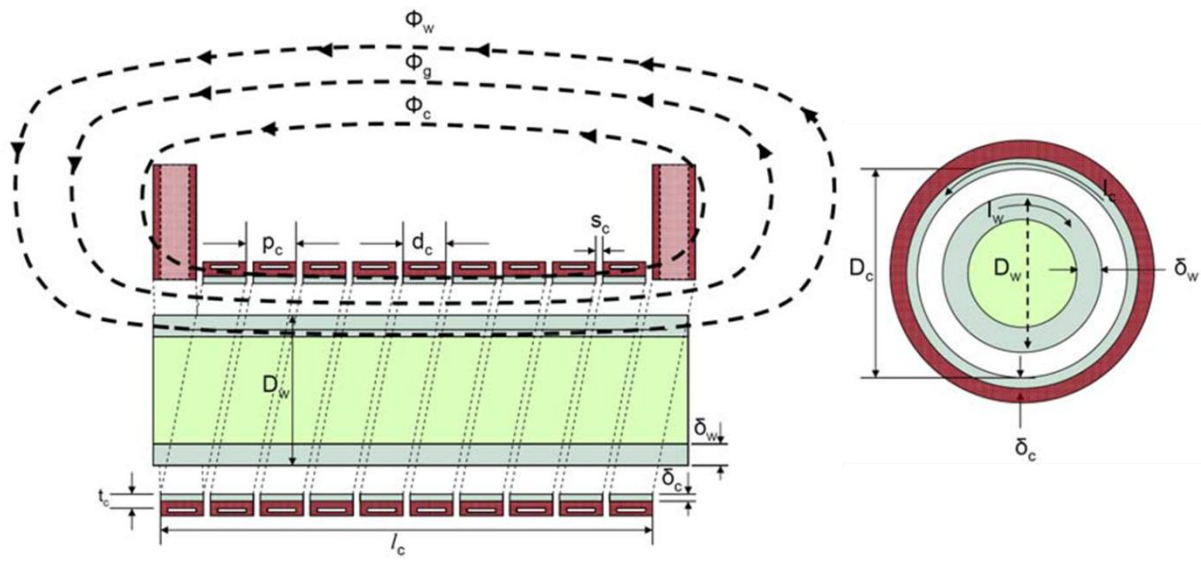


Figure 19: The 10 turn induction coil for aluminium billet heating proposed by Kennedy et al. [33]

The height, diameter and volume of the molten bath is given by equations (2.11) and (2.12), below.

$$V_m = \frac{\pi D_w^2 l_c}{4} = \frac{M}{\rho_v} \quad (2.11)$$

$$l_c = \sqrt[3]{\frac{4V_m X^2}{\pi}} \quad (2.12)$$

Where l_c is the height of the inductor, D_w is the diameter of the charge i.e. the crucible diameter, M is the mass of the charge, ρ_v is the density of the charge and X is the ratio between the height and the diameter of the charge. The next step is to calculate the dimensions of the coil itself. Kennedy et al. use the assumption that the coil is a helical copper spiral which approximates that of a theoretical "current sheet" with N_c turns, a sketch of which is shown in Figure 20 below.

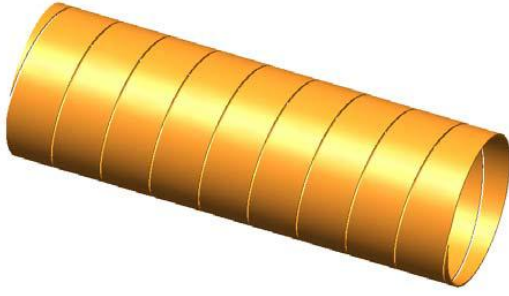


Figure 20: 10 turn helical “current sheet” coil or solenoid [33].

The space factor, k_r , gives the fraction of the side of the coil occupied by copper, and will be used later to account for air gaps in the solenoid.

$$k_r = \frac{d_c N_c}{l_c} = \frac{d_c N_c}{[(N_c - 1)s_c + d_c N_c]} \quad (2.13)$$

$$d_c = \frac{l_c k_r}{N_c} \quad (2.14)$$

$$l_{wire} = (D_c + \delta_c)\pi N_c \quad (2.15)$$

The width of the wire of the solenoid is given as d_c , the gap width is s_c , the internal diameter of the inductor is D_c , the wire length is l_{wire} and the skin depth is δ_c . The AC frequency used for this induction furnace is assumed to be high enough that the electromagnetic penetration depth is much smaller than the radial dimension of the copper conductor. In other words, all of the current is passed through a thin, inner layer of the conductor, just like the eddy currents in the charge is contained within a thin sleeve. Equation (2.9) is therefore applicable to the conductor as well, as long as the air gaps in between the coils are accounted for by introducing the space factor k_r . The relative magnetic permeability of copper (μ_r) is 1 [35].

$$\delta_c = \sqrt{\frac{\rho_c}{k_r \pi f \mu_0}} \quad (2.16)$$

The resistivity of copper is given as ρ_c . Because only a small fraction of the copper conductor is carrying the current, the effective area for the current path, $a_{current}$, is reduced and the resistance of the copper coil, R_c , is increased. The resistance can then be calculated from equation (2.10).

$$a_{current} = d_c \delta_c = \frac{\delta_c l_c k_r}{N_c} \quad (2.17)$$

$$R_c = \frac{\rho_c l_{wire}}{a_{current}} = \frac{\rho_c (D_c + \delta_c)\pi N_c}{\frac{\delta_c l_c k_r}{N_c}} = \frac{\rho_c (D_c + \delta_c)\pi N_c^2}{\delta_c l_c k_r} \quad (2.18)$$

The resistivity of the copper coil, ρ_c , varies greatly with the amount of impurities, which is important to remember when designing the coil. One way of quantifying this is by using the International Annealed Copper Standard [36], which uses a simple fraction, %IACS, to account for impurities. The conductivity of pure copper at room temperature, ρ_{0c} , is $1,7241 \cdot 10^{-8} \Omega m$, with a temperature coefficient, α , of $3,93 \cdot 10^{-3} K^{-1}$. The actual resistivity of copper, ρ_c , is given by equation (2.19), below.

$$\rho_c = \frac{\rho_{0c}(1 + \alpha \Delta T)}{\%IACS} \quad (2.19)$$

The temperature increase from room temperature is ΔT . As the resistance of the coil is now known, the ohmic power losses to heat in the coil, P_c , can be calculated from equation (2.8). The current supplied by the generator, I_c , must first be chosen. In equation (2.20), the root-mean-square (RMS) value for the AC current is used [37].

$$P_c = I_c^2 R_c = \frac{I_c^2 \rho_c (D_c + \delta_c) \pi N_c^2}{\delta_c l_c k_r} \quad (2.20)$$

$$I_c = \sqrt{I_{peak}^2} = \frac{I_{peak}}{\sqrt{2}} \quad (2.21)$$

The amplitude of the AC current the generator will deliver is I_{peak} . When the geometry of the furnace is to be calculated, the heat balance for the furnace must be solved and a melt cycle time must be chosen in order to determine the necessary power input to the charge. The lower limit of the melt cycle time is dictated by the capacity of the equipment, the upper limit is dictated by economic aspects. The heat balance has been calculated with HSC software using measured values for slag composition and silicon content as input to the calculation. The necessary power input to the charge is calculated using equation (2.22).

$$P = \frac{Q_{th}}{t} \quad (2.22)$$

The theoretical heat energy is given as Q_{th} and the melt cycle time is given as t . Calculating electrical parameters for an induction furnace is complicated, because of the many magnetic flux linkages and the complex differential equations needed to accurately solve the system. Empirical equations or numerical methods are therefore often used. One such empirical equation used by Kennedy et al. is the modified Nagaoka constant. It accounts for the fact that the coil has a finite length and that the charge affects the flux density in the gap between the coil and the charge. It also accounts for the induced eddy currents in the charge which will create an opposing magnetic field that in turn reduces the net flux in the space occupied by the charge. Exact solutions to the magnetic flux density assume uniform internal and negligible external flux density, which is a gross assumption when the ratio of the internal diameter of the coil and the length of the coil is less than about 8. The modified Nagaoka constant is given in equation (2.23), below.

$$k_N^* = \left(1 + \frac{0,4502(D_c + \delta_c)}{l_c}\right)^{-1} \left(1 - \left(\frac{D_w}{(D_c + \delta_c)}\right)^2\right) + \left(\frac{D_w}{(D_c + \delta_c)}\right)^2 \quad (2.23)$$

The effective magnetic flux which induces eddy currents in the charge can be found by Ampère's law or the Biot-Savart law [29], multiplied with the modified Nagaoka constant.

$$B_w = k_N^* B_\infty = \frac{k_N^* \mu_0 N_c I_c}{l_c} \quad (2.24)$$

The magnetic flux through the charge is B_w , the theoretical flux through an infinitely long coil is B_∞ . There is an upper limit to the magnetic flux, because a high magnetic flux will result in a high magnetic field strength, which imposes a powerful magnetic force on the charge. As the charge melts, the imposed magnetic field will tend to force the outer melt towards the center, creating a circular flow in the charge. The flow pattern is shown in Figure 21, below. If the magnetic field strength is high enough, the flow in the furnace can reach levels where the molten charge starts splashing out of the crucible. This could be dangerous to the operators and to equipment, it could

lead to loss of material, and as mentioned in chapter 2.2.5 Melt stirring speed, it could entrain silicon back into the slag phase. The magnetic field strength (H) is calculated using equation (2.25). Y. Sundberg [38] has presented an equation for calculating the maximum allowable field strength before splashing becomes a problem. It assumes that the fluid motion will produce a meniscus on the surface whose height, Δh , can be found by equating the hydrostatic pressure of the surface with the electrostatic pressure generated by the field. Empirically, the maximum height before splashing occurs is $\frac{\Delta h}{d_w} < 0.19$. This gives equation (2.26), which calculates the maximum allowable field strength for a melt of density ρ_v and a bath diameter of d_w . The gravitational acceleration is given by g , and is equal to 9.81 m/s^2 .

$$H = \frac{B_w}{\mu_0} \approx \frac{N_c I_c}{l_c} \quad (2.25)$$

$$H_{max} = \sqrt{\frac{2\rho g(0.19 \cdot d_w)}{\mu_0}} \quad (2.26)$$

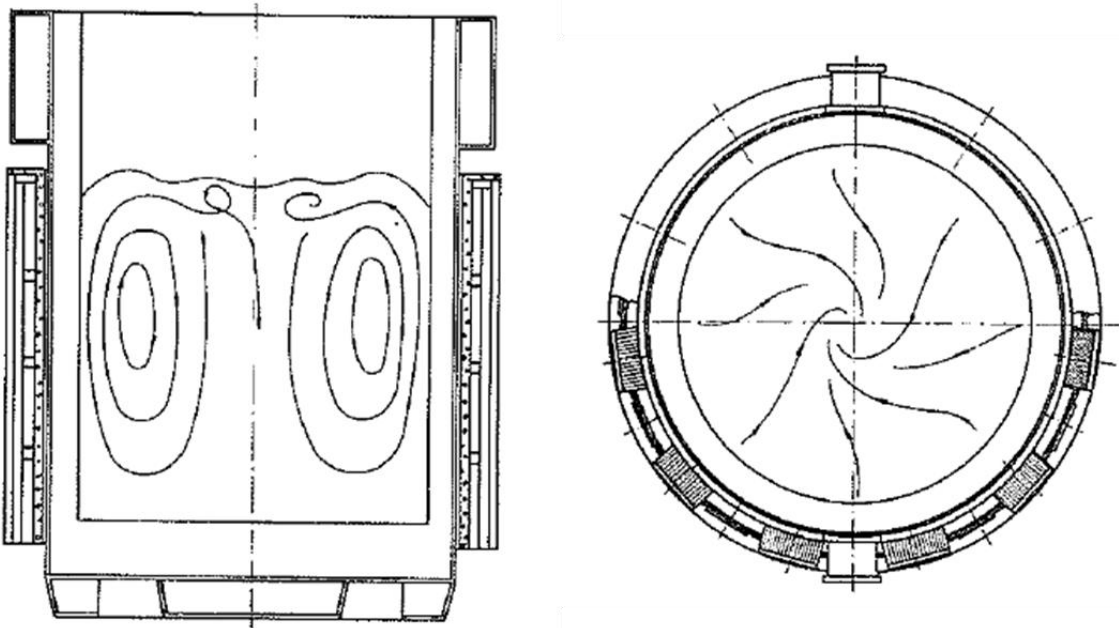


Figure 21: Flow patterns in an induction furnace [38].

Since all of the current in the charge is assumed to be carried in a thin sleeve with thickness equal to the skin depth, the charge can be **approximated** as a single turn coil ($N_w = 1$), and the current can be calculated using the ideal transformer relationship [29], referring the conditions back to the coil.

$$N_w I_w = k_N^* N_c I_c \left(\frac{l_c}{l_w} \right) = k_N^* N_c I_c \quad (2.27)$$

$$I_w = k_N^* N_c I_c$$

The current in the charge is I_w . If the length of the charge, l_w , is greater than the length of the inductor, l_c , the term $\left(\frac{l_c}{l_w} \right) = 1$ as it is assumed that only the part of the charge which is inside the

inductor interacts with the magnetic field of the coil. The next step is to calculate the resistance of the charge, R_w , and refer this back to the coil where voltage, current, impedance and resistance, R_w' , can be measured. This can be done using Bessel functions with complex numbers to solve the magnetic field equations, which are computationally very challenging. The result of the Bessel functions is $\varphi(\xi_w)$, shown as a plot in Figure 22. As ξ_w exceeds 3 the curve converges toward 1, meaning that as the length of the inductor increases, the solution approaches the ideal.

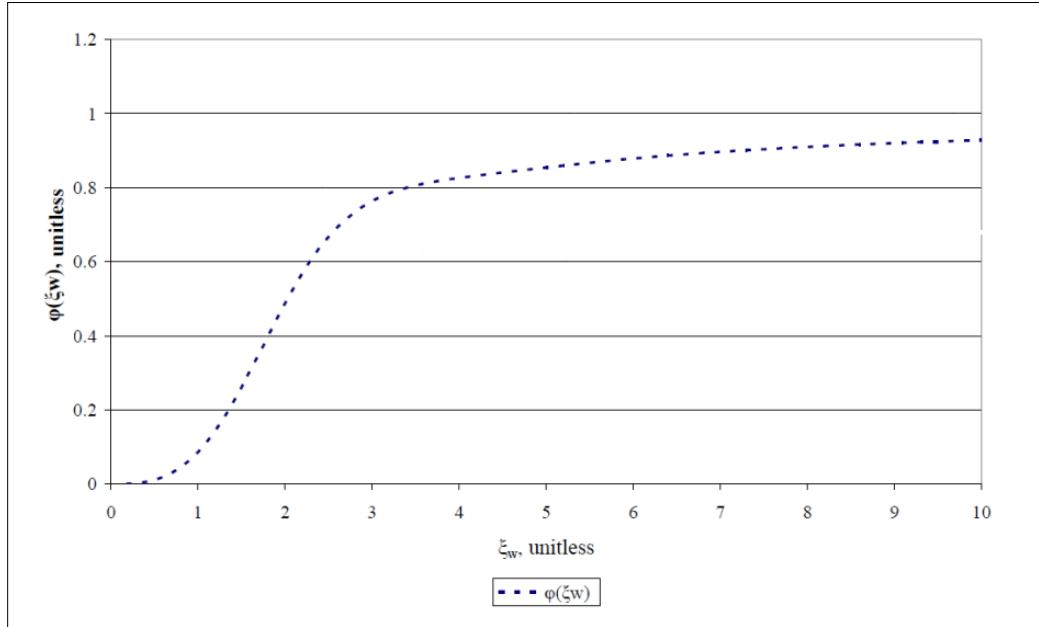


Figure 22: A plot of $\varphi(\xi_w)$ as a function of ξ_w [33].

$$\xi_w = \frac{D_w}{\delta_w \sqrt{2}} \quad (2.28)$$

$$R_w' = R_w N_c^2 = \frac{\sqrt{2} \pi N_c^2 \rho_w \xi_w \varphi(\xi_w)}{l_c} \quad (2.29)$$

The dimensionless parameter ξ_w is important in induction heating theory. If the skin depth is comparable in size to the diameter of the work piece, eddy currents generated on one side of the work piece can cancel out eddy currents generated on the other side. To avoid this phenomenon, the heating frequency must be sufficiently high, or the width of the inductor must be increased. Either choice will alter the electric properties of the system.

The power generated in the work piece can now be calculated by inserting equation (2.27) and (2.29) into equation (2.8).

$$P_w = I_w^2 R_w = I_w^2 \frac{R_w'}{N_c^2} = \sqrt{2} \pi \frac{k_N^{*2} N_c^2 I_c^2 \rho_w \xi_w \varphi(\xi_w)}{l_c} \quad (2.30)$$

By inserting the physicochemical parameters of silicon into equations (2.8) to (2.30), an induction furnace for remelting of silicon can be dimensioned. This has been done in chapter 4.3.2 Dimensioning an induction furnace for remelting off-grades.

2.3.3 Refractories

As all of the electrical and physical parameters of an induction remelting furnace have been set, the next step is to choose a refractory lining system which can be used in the remelting process. Choosing the correct lining material for a new smelting project is critical to the safety, the lifetime and the income of the project, as the lining is a large part of the total expenditure.

The ISO standard defines a ceramic material as a refractory if its softening temperature is equal or better than the pyrometric cone equivalent of $>1500\text{ }^{\circ}\text{C}$ [39]. In practice, the label refractory is given to any material which is mainly made to withstand a high temperature ($600 - 2000^{\circ}\text{C}$ [40]). The core groups of refractories are high-melting metals like wolfram and tantalum, nitrides like silicon nitride (Si_3N_4) and boron nitride (BN), carbides or carbonaceous materials like silicon carbide and graphite or oxides like magnesite, dolomite, silica and alumina. Of these, only the carbonaceous and oxidic materials are used in any large scale in metallurgical industry. In addition to the traditional refractories, freeze lining made by freezing the charge closest to the furnace wall is a modern addition to the lining assortment. The advent of freeze linings was a radical change in furnace design mentality, and the technology should theoretically be viable for almost any smelting process.

Choosing an optimal lining system is difficult, as the list of influencing parameters is extensive [41]. The chosen refractory must be structurally stable, as it must support both its own weight and any weight laid upon it, even at elevated temperatures. It should expand as little as possible as a function of temperature to avoid furnace “pregnancy”, i.e. bulging of the furnace sides due to expansion of the inner lining. It must be resistant to thermal cracking, and it cannot spall or implode/explode under any circumstance. Explosion is a definite possibility when the lining is water cooled, which is the norm for metallurgical reactors. Say a refractory stone is used which contains large, poorly distributed pores. If a crack opens which channels molten slag or metal through the stone onto the cooling system, it could result in a violent steam explosion [42]. Thus, having good control of the pore structure of the refractory stone used is important. Thermal cracking resistance can also be improved by ensuring good pore distribution, and by using materials with good thermal conductivity and low specific heat. In order to choose the correct lining setup, a thorough knowledge of both the process chemistry and the physical process parameters is needed.

The chemical composition of the lining is directly coupled to the chemistry in the furnace, because the two phases will be in intimate contact. If equilibrium or pseudo-equilibrium is not in place, the slag and metal phases will react with the lining, and dissolve it into the melt [41]. Initially, as the melt comes into contact with fresh lining it infiltrates into the pores of the refractory. The depth of infiltration is determined largely by the amount of porosity, by the viscosity and wettability of the slag and by the temperature gradient through the lining. As the slag reaches the infiltration depth, the flow is either stopped by increased viscosity or by crystallization of slags due to the temperature gradient. After this initial phase, the lifetime of the lining is defined by the speed of reaction from the lining to the slag, which again depends on the phase composition of the slag and the lining. The lifetime of the lining could however be drastically reduced by unexpected changes in slag composition or physical disturbances like shut-downs or accidents. Often, these disturbances end up being decisive for the total lifetime of the refractories [43].

The compatibility of a lining material to a slag is often measured by basicity, defined in chapter 2.2.3 Viscosity as the tendency to create or break oxygen networks. Table 1 shows an overview of common

oxidic materials and their basicity. Like acids and bases in aqueous solutions, the overall basicity of a slag mix is given by the molarity of its components. A molar ratio of SiO_2/CaO below 1 is referred to as basic, while a ratio above 2 is referred to as acidic [40]. If the basicity of the slag and the basicity of the lining are a close match, it is likely that they will be compatible with each other.

Table 1: Characterization of oxidic materials according to chemical reaction behavior [40], [18].

Term	Reaction or behavior	Refractory material
Acidic	Oxide + H_2O = Acid $\text{SiO}_2 + 2\text{O}^{2-} = \text{SiO}_4^{2-}$ Network forming specie	Silica, fireclay, porcelain, zircon silicate.
Basic	Oxide + H_2O = Base (hydroxide) $\text{CaO} + \text{H}_2\text{O} = \text{Ca}(\text{OH})_2$ Network breaking specie	Products with magnesia or dolomite base, lime.
Neutral/Amphoteric	Reacts both ways, depending on the basicity of the system	Alumina, chromite, picrochromite, spinel, forsterite

It is actually possible for lining materials to be compatible for a given slag composition even if the basicity of the slag and the basicity of the lining is not a match. If the kinetics of the slag-lining reaction is very slow, the lining lifetime could be quite long. This is for example true for systems where the crystallized reaction products from the dissolution of lining into the slag have a higher melting point than the original lining. A good example has been presented by Seltveit [41]. When trying to melt cordierite ($2\text{MgO} \cdot 2\text{Al}_2\text{O}_3 \cdot 5\text{SiO}_2$) and heating it to $1600\text{ }^\circ\text{C}$, which is the best option between a crucible of pure silica (SiO_2), mullite ($3\text{Al}_2\text{O}_3 \cdot 2\text{SiO}_2$), corundum (Al_2O_3) or periclase (MgO)? Figure 23 shows the melting paths of each material in contact with cordierite.

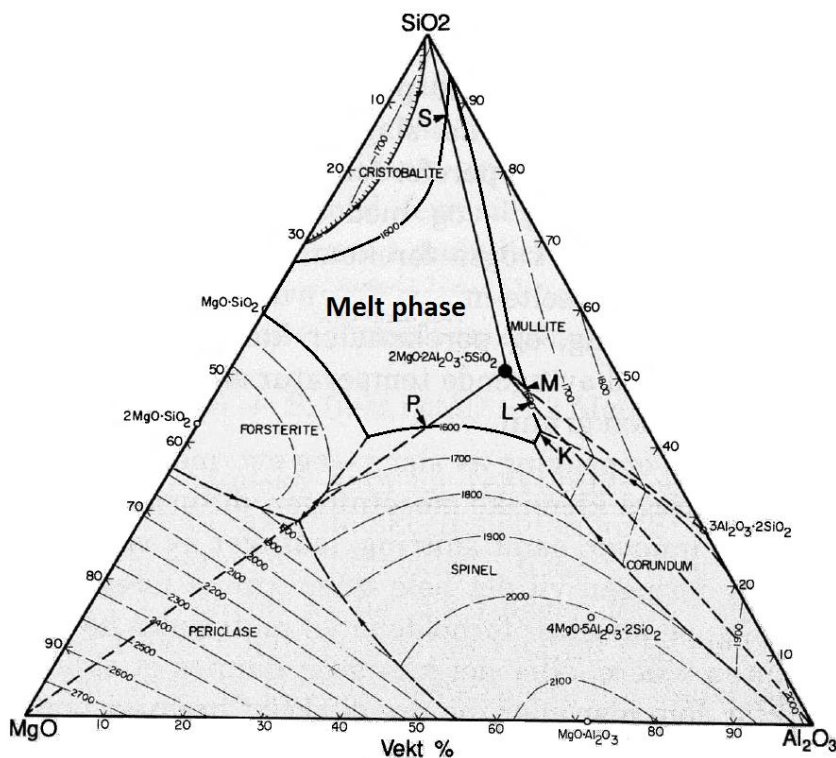
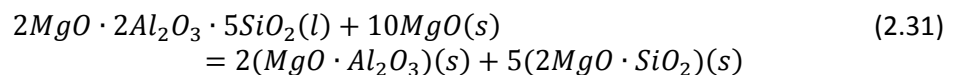


Figure 23: Isothermal section of the Al_2O_3 - MgO - SiO_2 phase diagram [41].

Choosing silica is obviously a bad choice, as the path to saturation (marked “S”) is very long and the dissolution loss will be high. Following the rule of thumb and choosing similar basicity, mullite should be the best choice, as the slag would be saturated already at the point marked “M”. However, the reaction products would not create any sort of protecting layer, so the speed of dissolution is determined only by the speed of diffusion from the lining into the slag. A corundum crucible would first be covered by a thin layer of mullite, marked by point “L”, and the continuing reaction would be determined by the speed of conversion from corundum to mullite, which would reach saturation at point “K”. Using periclase would lead to a large initial dissolution rate, but as soon as the melt concentration reaches the point marked “P” spinel would be formed. Spinel will drastically reduce the speed of the reaction between cordierite and periclase to spinel and forsterite (equation 2.33), and will therefore result in a stable lining:



The same exercise as above can be done for melting off-grades, using the Al_2O_3 -CaO- SiO_2 slag system and plotting the composition of the slag found by XRF. From here, saturation lines can be drawn to silica, mullite, corundum and lime, as in Figure 24. The lime saturation line corresponds approximately to using a lining made of Portland cement, even though there will always be some Al_2O_3 and SiO_2 in Portland cement.

A crucible made of silica will be just as bad a choice for this system as for the Al_2O_3 -MgO- SiO_2 system, as the path to saturation (marked “S”) is just as long. This is the case for a lining of Portland cement as well (marked “P”). In addition, the viscosity of high-CaO slags is very low compared to high-silicon slags. As CaO is dissolved into the slag, the fluidity would increase and the melting point would sink, giving a greater penetration depth of the slag. Using mullite would likely be a good choice of refractory, as the slag composition is more or less on the 1600 °C isotherm and the path to saturation is short (marked “M”). Using corundum is also a great choice, because the path to the 1600 °C isotherm is short (marked “L”), and the dissolution rate is determined by the reaction from corundum to mullite (marked “K”). In fact, the refractory used by Elkem Thamshavn to line their ladles is a monolithic casting concrete called Silmet 75, which is made of a corundum/mullite mix bonded by lime and microsilica [44]. This hard, dense, low-cement refractory is then covered by a high-cement spray concrete with the same overall composition called Rescocast 17 G [45]. The spray concrete will have a brittle, porous structure compared to the hard, dense outer refractory. When a substantial layer of freeze linings have grown onto the linings, it must be chiseled out by pneumatic hammers. The force of the hammers will then crumble the spray concrete, while the harder low-cement concrete is left unharmed. The total lifetime of the lining is therefore increased many times over.

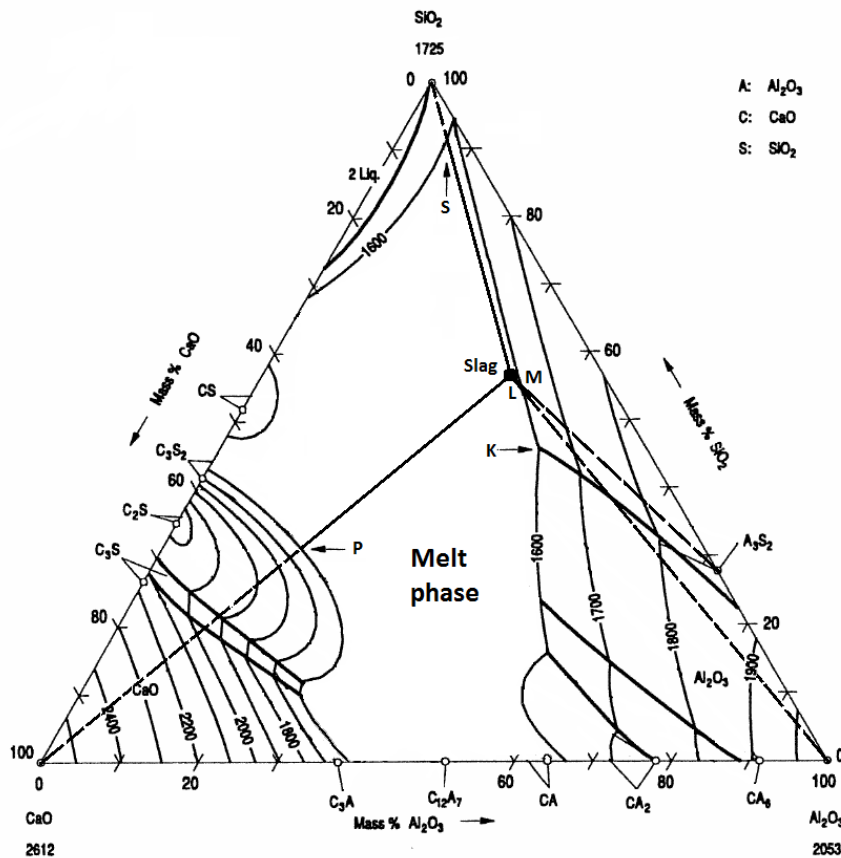


Figure 24: Saturation lines between slag and refractories in the $\text{Al}_2\text{O}_3\text{-CaO-SiO}_2$ system [15].

It is clear then, that the lifetime of a given lining can be improved either by matching the thermodynamic properties of the lining to the expected slag composition, or by decreasing the speed of reaction to near zero. However, when remelting off-grades the slag composition is going to vary a lot from batch to batch, so the lining will rarely be in equilibrium with the slag. In these systems, only a lining made from the slag itself will be in equilibrium with the molten slag at all times. Such a lining is called a freeze lining, and represents a radical change in the way high-intensity furnaces are constructed.

2.3.4 Freeze linings

Regular refractories operate on a “wear versus time”-basis [46], meaning that the thickness of refractory installed is determined by the demand on service length before relining. Even with an initially perfect refractory concept, there will be a maximum service length because deviations in the process will lead to deviations from equilibrium, and because external factors could reduce the lining lifetime. A freeze lining allows true thermal and chemical equilibrium to be achieved, and under steady-state conditions the wear on the actual refractory and cooling systems should be almost zero. Most freeze lining systems are composed of water cooled copper blocks, copper fingers or copper waffles, which are in direct contact with slag and/or metal. Refractory brick or ramming paste is often used in conjunction with copper as a safety feature.

Designing a freeze lining of a particular size is a matter of controlling the heat flux out through the side wall and bottom of the furnace in order to attain a steady-state thickness of frozen slag on the furnace wall. To choose the correct cooling system for a given process one needs to solve the heat

balance for the system. The following derivation of the heat balance is based on a paper by Hugo Joubert [43]. If one assumes that a freeze lining is already in place for a given system, the heat load on the sidewall, q , is given by equation (2.32).

$$q = h_{slag}\Delta T = h_{slag}(T_{slag} - T_{freezing}) \quad (2.32)$$

The slag-to-sidewall heat transfer coefficient is given by h_{slag} , the over temperature is ΔT , i.e. the difference between the actual slag temperature and the freezing point of the slag. Because of the liquidus-solidus temperature range of the mushy zone [47], the freezing point of the slag is taken as the average of the liquidus and solidus at the given slag composition. The thermal resistance in this mushy zone is not taken into account, and so the actual load on the sidewall is slightly over-estimated.

$$T_{freezing} = \frac{T_{liquidus} + T_{solidus}}{2} \quad (2.33)$$

The heat load on the sidewall from the slag calculated by equation (2.32) gives the absolute minimum heat load that the external cooling systems must be able to remove, and therefore the maximum thermal resistance of the lining, R_{freeze} , and the cooling system, R_{lining} .

$$q = h_{tot}(T_{freezing} - T_{cooling}) = \frac{(T_{freezing} - T_{cooling})}{R_{freeze} + R_{lining}} \quad (2.34)$$

The temperature of the cooling water is given as $T_{cooling}$. The thermal resistance is then a function of the thermal conductivity, k_{freeze} , and the thickness, x_{freeze} , of the freeze lining.

$$R_{freeze} = \frac{x_{freeze}}{k_{freeze}} \quad (2.35)$$

As R_{freeze} is given by the necessary thickness of the freeze lining, the thermal resistance of the rest of the system must be low enough to satisfy equation (2.36).

$$R_{lining} \geq \sum \frac{x_n}{k_n} + \frac{x_{shell}}{k_{shell}} + \frac{1}{h_{cooling}} \quad (2.36)$$

The parameter n specifies the number of refractory layers present in the sidewall, as each layer will add a certain amount of thermal resistance. The shell must naturally also be included, even though mild steel has a very high thermal conductivity ($45-50 \frac{W}{mK}$) [48]. It is of utmost importance to establish good contact between the refractory lining and the shell. Even thin gaps would greatly increase the thermal resistance leading to a severe reduction in freeze lining thickness in this region [49]. To prevent this from happening, highly conducting graphite tiles are sometimes glued to the shell. If an air gap forms, the graphite tiles can conduct the heat in the particular zone to the adjacent areas. It is also possible to inject a grouting mix into the void through the steel shell, thereby restoring contact between the refractory and the shell [41].

As the intensity of the furnace is increased, the heat flux through the wall must also be increased, which means that as processes get more and more intensive, freeze linings can only be kept stable by

better coolers. In chapter 4.3.3 Freeze lining thickness, equations (2.34) to (2.38) are used to calculate the necessary cooling capacity for a hypothetical slag furnace. The result of 45 kW/m^2 is such a high heat flux that all kinds of air cooling systems are out of the picture, as shown in Figure 25. Only copper coolers can transport heat quickly enough to sustain the lining thickness. These can be made in various shapes, but the challenges faced are the same no matter how the system is made. It is important to note that the maximum capacity of the system must be much larger than the steady-state value, as a safety buffer in case of process disturbances. Joubert recommends a safety factor of at least 4 in order to be certain that cooling capacity is never a limiting parameter. This has been accounted for in the calculation in chapter 4.3.3 Freeze lining thickness.

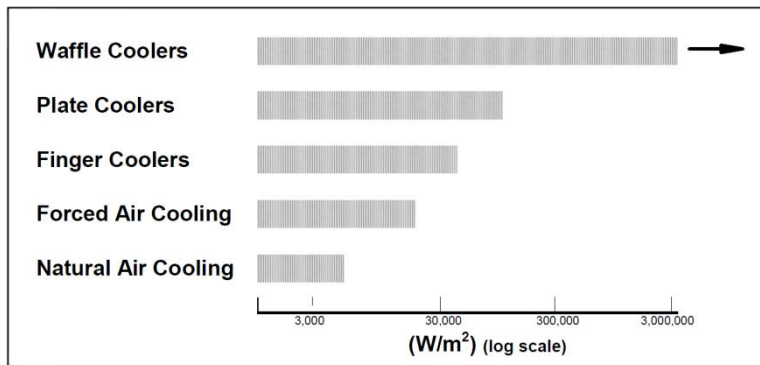


Figure 25: Comparison of different cooling systems [50].

Finger coolers consist of copper elements welded to a copper back plate which is cooled by oil or water. Each finger penetrates the furnace brickwork and act either directly on the slag or on a thin outer refractory layer. The cooling media has to be outside the furnace hearth to avoid steam explosions inside the furnace should a water leakage occur. Plate coolers expand the concept by increasing the surface area of each finger, giving higher heat transfer capabilities at the cost of increased volumes of copper [51]. Waffle coolers use a slightly different approach, as the cooler no longer extend through the furnace brickwork, but is actually the structural component of the furnace wall, thereby removing the need for furnace brickwork altogether.

In the bottom of Figure 26, below, is shown a section of what is called a “duck-tailed” waffle cooler, which refers to the slanted shape of each pocket in the surface, shown to the bottom-right of the figure. The structure is cast in copper, and the pockets are filled with refractory material [52]. Having refractory-filled pockets reduces the surface area exposed to molten slag if the freeze lining spalls, thereby increasing the lifetime of the copper lining. Since the pockets are duck-tailed, the initial refractory is held in place even as the freeze lining spalls, and can instantly initiate growth of new lining.

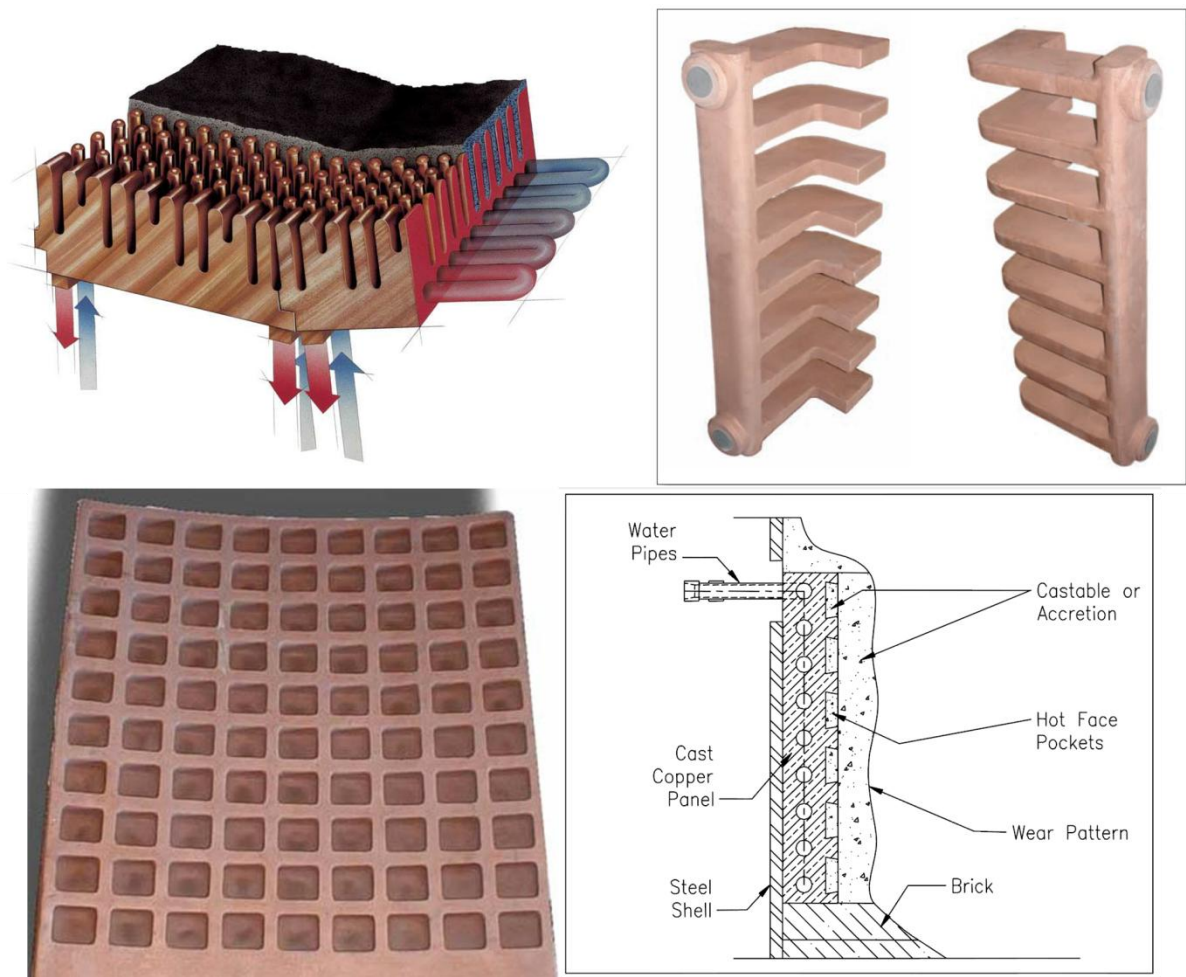


Figure 26: Different cooler solutions.

Upper left: Finger cooler. Upper right: Plate cooler. Bottom left: Waffle cooler. Bottom right: A sketch showing the horizontal section of an installed waffle cooler.

2.3.5 Lining problems

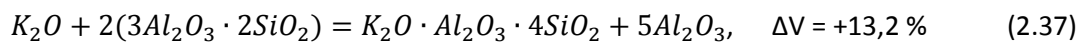
It is important to be aware that the refractory lining is going to be used in severe conditions of high temperature, aggressive environments, high loads and regular temperature cycles. Over the course of a furnace lifetime, the lining is likely to fail several times. Knowing what to expect from these failures is therefore critical both to the design of the furnace and the design of the lining.

The worst problems any lining solution can face are explosions or eruptions as a result of burn-through by liquid metal or slag. Since all the lining concepts detailed above are water or oil cooled, the danger of an explosion following a burn-through is always present, no matter how well the system has been designed. However, by being aware of the problems which a given lining is likely to face, and installing monitoring and early warning systems in problem areas, the risk can be reduced to a minimum.

As mentioned earlier, a rather serious problem furnaces can experience is “furnace pregnancy”, i.e. bulging of the furnace walls caused by infiltration of slag, metal or gases into the cracks of the brickwork. Almost all materials have a positive thermal expansion coefficient, i.e. they expand on

heating. This is logical, as increased temperatures increase the vibrations of atoms in their lattices, increasing the total volume of the lattice. Therefore, the bricks are laid down during relining with a certain gap to account for thermal expansion, so that the wall is completely tight at the operating temperature. However, when furnace irregularities like breakdowns or long maintenance periods lower the brickwork temperature, the brick will contract, giving liquids and gas an opportunity to infiltrate the cracks and solidify. As the furnace is restarted and the brickwork expands, the extra material forces the circumference of the furnace to increase, making the furnace wall bulge out [53]. Over time this can lead to a rupture in the furnace wall, which is both dangerous to any workers nearby and expensive to repair.

Another mechanism of expansion in the brickwork is by reaction with the charge. A common example is when mullite bricks are exposed to alkali oxide gases, most often potassium oxide (K_2O). This is a common problem in the primary production of many metals, because mullite is an excellent refractory for many applications, and alkalis will tend to accumulate in the furnace in many metallurgical processes. The volume expansion by reaction with K_2O is 13.2 %, and the reaction products can also further react with more potassium oxide, resulting in an even greater volume change. For a furnace diameter of 6 meter, this would result in an obviously impossible 2.4 m increase in circumference. As the exposed layers react, the internal stresses crack the brickwork which spalls and enters the slag, reducing the lifetime of the lining. The reaction between mullite and potassium oxide is given in equation (2.37), below [41].



A solution to furnace pregnancy which has been implemented on new furnaces since about the 1980s [53] is spring loading of the furnace wall, giving the whole of the wall an opportunity to expand and contract in a controlled manner. This is shown below in Figure 27. Having sufficient force on the brickwork at all times should keep the gaps closed, giving the furnace lining a much better fatigue life. This does not alleviate the problem of chemical attack by slag and alkalis, but it could possibly reduce the rate of attack since less of the lining is exposed.

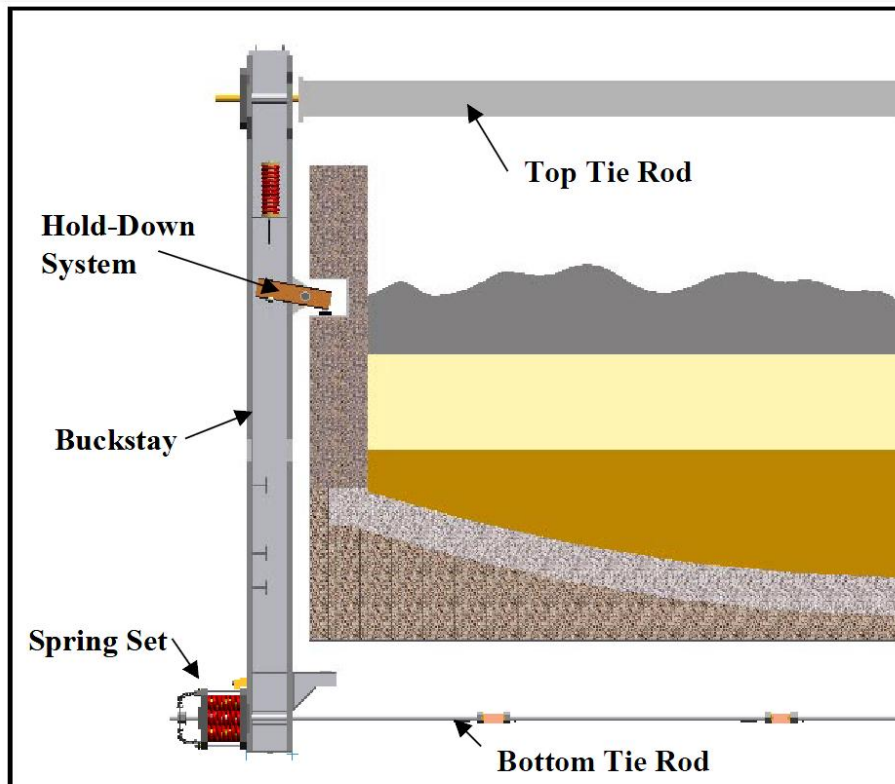
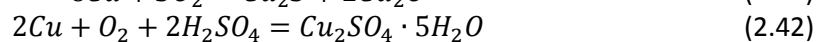
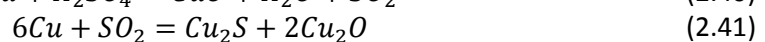


Figure 27: Spring loaded furnace [53]

Freeze linings face a problem which is more specific to the technology. The copper cooler is much colder than the charge, so gaseous species will move towards the copper surface because of natural convection. As they reach the copper, several reactions could occur which will erode the copper and eventually destroy the cooler. Even with very pure raw materials, these species will be present in the system, and can cause damage. Equations (2.40) to (2.44) show some of the possible reactions of gaseous species with copper [54].



One way of dealing with this problem is to install monitoring systems which can measure the copper thickness and the freeze lining thickness. These can either be external devices which work for example by ultrasound or some form of internal devices which can measure temperature changes in the copper. Internal devices are more cumbersome to produce because they have to be included when the block is cast, and when they are in place they are normally not replaceable. However, they have the important advantage that they can measure the whole of the copper surface. Ultrasonic devices cannot measure behind the copper tubing, where accurate measurements are most important. This is shown in Figure 28, below.

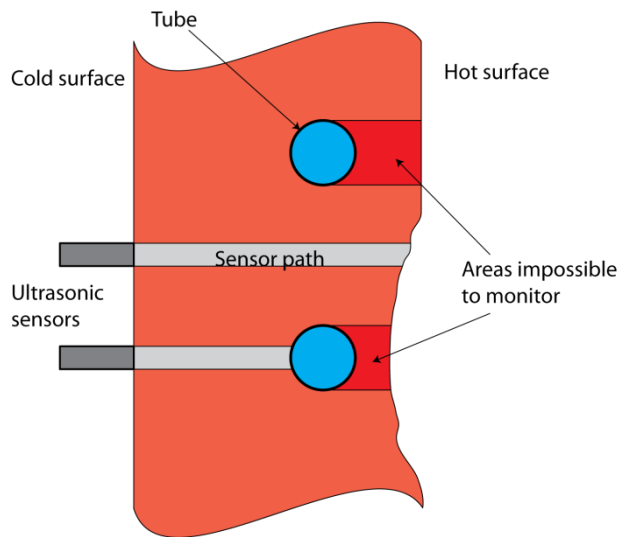


Figure 28: Monitoring of copper coolers using ultrasonic sensors

3 Experimental procedure

Important theory governing the different separation methods investigated in this thesis has now been presented. Several experiments were carried out based on these theories: Dense medium experiments, aimed to find the suspension density where only one of the phases would float, validating the separation method for silicon-slag systems. Optical separation experiments were done externally at Comex AS to uncover the threshold values in color and reflectivity between slags and silicon. Manual separation was then done, based on these thresholds. Zeta potential measurements were carried out to establish the viability of the method at pH 7, without surface activators. Remelting experiments were carried out in a small-scale induction furnace using different slag fluxes. The experimental procedures will be discussed in detail along with descriptions of the materials used.

It is important to note that some of these tests were done on a trial-and-error basis, and some of the parameters are therefore changed in the middle of a series of experiments to factor in new knowledge of the setup. The furnace design and freeze lining calculations are not included in this chapter, but can be found in chapter 4.3 .

3.1 Material

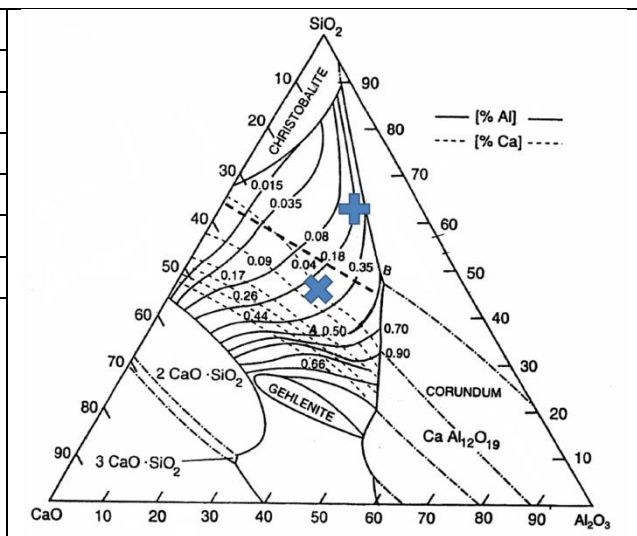
The raw material used for the dense medium experiments and the remelting experiments was off-grades from the slag pit at Elkem Thamshavn's furnace #2, taken just a short time after tapping. An XRF analysis of the metal produced in that particular tapping is given in Table 2. Because the silicon and slag phases interact with each other, the impurity content of the silicon should be in equilibrium with the content of the process slag. The analysis of the refined metal corresponds approximately to the cross (X) in the reprint of Figure 9, below. The actual composition of the slag is given by the plus sign (+). Before remelting, the off-grades were crushed to -25 mm. The limestone added in two of the remelting experiments was also taken from Elkem Thamshavn. In experiment number 6, rock dolomite containing 12 wt% MgCO_3 was added. The magnesium carbonate added to the last experiment was pure, powdered MgCO_3 from Sigma-Aldrich [55].

The raw material for the optical sorting experiments was freeze linings chiseled from the ladles. These were not crushed before processing. In the dense medium separation experiments, two magnetite powders with different grain size distributions were used to create the heavy medium. These were supplied by Colorana AS, and had product identification tags M-10T (fine grains) and M-20T (coarser grains) [56].

Table 2: XRF metal analysis

Prøve:	Furnace 2	14. jan	201101491
	Tapped	Dip	Refined
Si	98,30 %	99,00 %	98,90 %
Al	0,60 %	0,20 %	0,26 %
Ca	0,31 %	0,03 %	0,04 %
Fe	0,46 %	0,44 %	0,44 %
Ti	0,03 %	0,03 %	0,03 %

Figure 9, reprinted with a cross to show the approximate slag composition corresponding to the metal analysis above: 24 % Al_2O_3 28 % CaO 48 % SiO_2 . The plus-sign denotes the composition found by XRF analysis.



3.2 Mechanical separation experiments

3.2.1 Dense medium separation

The aim of the DMS experiments was only to investigate the viability of a DMS-process, not to design the whole process from raw material to finished product. Doing a full analysis would require more time and resources than what was available for this thesis. Therefore, an experiment was designed to determine the fluid density which would float either the silicon ($\rho \approx 2,3$ [4]) or the slag ($\rho \approx 2,3 - 2,6$ depending on slag content). If there is a density where one phase floats and the other sinks, further investigation into dense media separation should be carried out. A dense medium was prepared by putting a few grains of slag and a few grains of silicon into a beaker with 300 mL of water. Powdered magnetite was sequentially added to the mix and held in suspension by a small impeller. As mentioned in chapter 2 Theory, the maximum density for which magnetite should be viable is $2,5 \text{ g/cm}^3$, which is above the density of silicon. Powder was to be added until one of the materials floated, or until the viscosity of the mix rose to the point where slag and silicon was trapped in the fluid. As explained in chapter 2.1.1 Dense medium separation, the viscosity of a suspension of solid particles increases as the particle size of the solids decrease. Should the fluid reach critical viscosity before either material floats, a coarser magnetite powder would be used. A photograph of the experimental setup is shown in Figure 29, below.

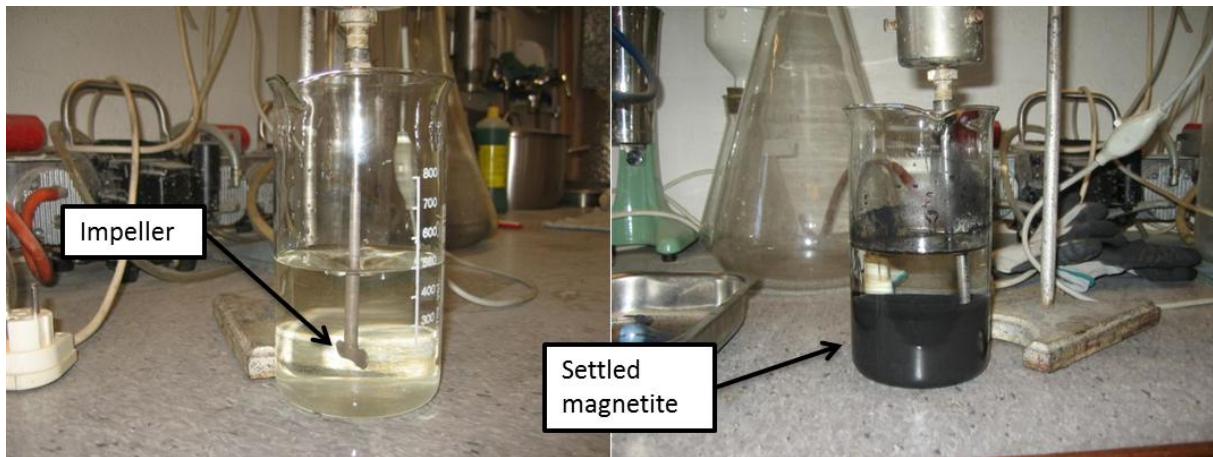


Figure 29: Experimental setup for dense medium separation

3.2.2 Optical separation

A sample was sent to Comex AS to be separated using their optical separation equipment. The finest fraction of -5 mm was removed prior to shipment, since optical separators are unable to handle the finest fractions. The rest of the sample was separated into a fine fraction (5-20 mm), a middle fraction (20-40 mm) and a coarse fraction (40-80 mm) using manual sieves. As the sample sent to Comex was small compared to full-scale industrial applications, it was only put through a small scale test. Small batches of the sample were selected, photographed and analyzed. The analysis was done by finding threshold values for the reflectance, color and hue of refractory materials, slags and silicon. The analysis software used was the same as those used in full-scale applications, and the results from small-scale experiments can later be used as starting points for determining the optimal thresholds in large-scale application. The various grains were sorted by hand into pure silicon grains (~100 % silicon), waste (~0 % silicon) and contaminated grains, based on the amount of either phase found in each particle. The analysis process is shown schematically in Figure 30. Samples were taken from each fraction and analyzed for chemical composition in the same way as the samples from the remelting experiments were analyzed, see Chapter 3.3: Remelting and settling of silicon.

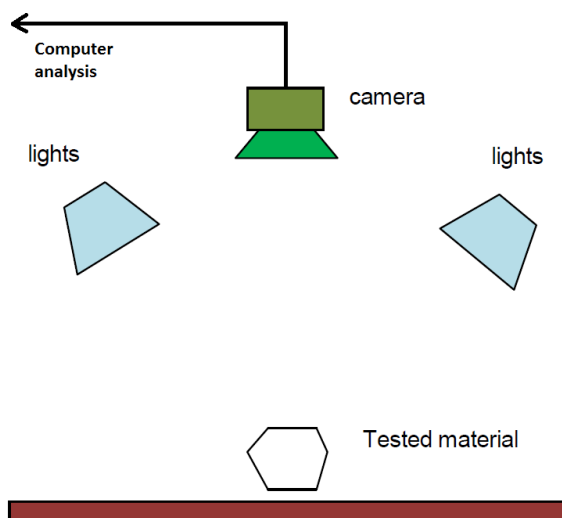


Figure 30: Analysis method used by Comex

3.2.3 Flotation – zeta potential analysis

Fully establishing the surface properties of slag and silicon and developing a whole flotation system would take too much time for this project. Therefore, only the zeta potential at 25 °C and pH = 7 was measured. As mentioned in chapter 2.1.3 Flotation, the zeta potential can be used to quantify the viability of separating two materials by measuring the potential difference between the materials. If the measurement showed that the potential difference is large, that could be a starting point for further investigation into flotation separation techniques. The zeta potential measuring device used was made by Malvern, model Zetaziser nano ZS. It measures the velocity of particles in a water suspension, using laser interferometry, as an external electrical field is applied. The measured velocity is then proportional to the zeta potential of the particles [57]. A fairly pure slag phase sample and a pure metal phase sample were crushed to -10 µm and mixed with distilled, deionized water to approximately 1 % by weight. It is important not to introduce ions into the solution, as these will alter the surface properties of the sample [3]. Each suspension was fed into a cuvette and analyzed twice by the zeta potential measurer in order to keep statistical errors down. The results were automatically plotted by the software as applied potential versus laser intensity.

3.3 Remelting and settling of silicon

The remelting experiments done in this project builds on the previous work by the author, which focused on finding the degree of settling as a function of settling time [2]. The aim in this work is to improve the speed of settling by adding limestone or dolomite to the charge mix. As explained in chapter 2 Theory, the viscosity of the slag should decrease and the spreading coefficient (the tendency for separation of phases) should increase when CaO or MgO is added to the mix. Both of these effects should decrease the settling time. The material used is slightly different compared to the previous work, as slag from the slag pit of furnace #2 is used instead of freeze linings. However, both of these sources are classified as off-grade material, and the results should be similar. Each crucible was heated to 1600 °C and held there for 10 or 30 minutes, depending on the experiment. The specific conditions for each crucible are given in Table 3. The “upgraded charge” was sorted by hand before remelting. The results were later compared to using an optical separation machine. In experiment 4 to 7, limestone or dolomite were added as flux to the slag in order to decrease the viscosity and reduce the melting point of the slag, which should increase the settling speed and efficiency. In experiments 4 through 6 the flux was added to the bottom of the crucible and the off-grade charge was laid on top. However, this led to two failed experiments where the flux did not mix with the charge and the charging pattern was changed in experiment 7. In that experiment, the flux was mixed with the off-grades before charging, giving a much better mixing into the melt.

Table 3: Experimental conditions

	Experiment	Raw material [g]	Addition of fluxes	Holding time [min] at 1600 °C	Estimated slag composition [wt%]			
					Al ₂ O ₃	CaO	SiO ₂	MgO
1	Original charge	4296	None	30	24	13	62	0
2	Upgraded charge	4297	None	30	24	13	62	0
3	Optically separated charge	4390	None	30	24	13	62	0
4	Low lime addition	4000	850 g limestone	10	20	30	50	0
5	High lime addition	4000	1625 g limestone	10	17	41	42	0

6	Low dolomite addition	4000	830 g dolomite (12 % MgO)	10	20	28	50	2
7	High dolomite addition	4000	370 g MgCO ₃	10	22	13	57	8

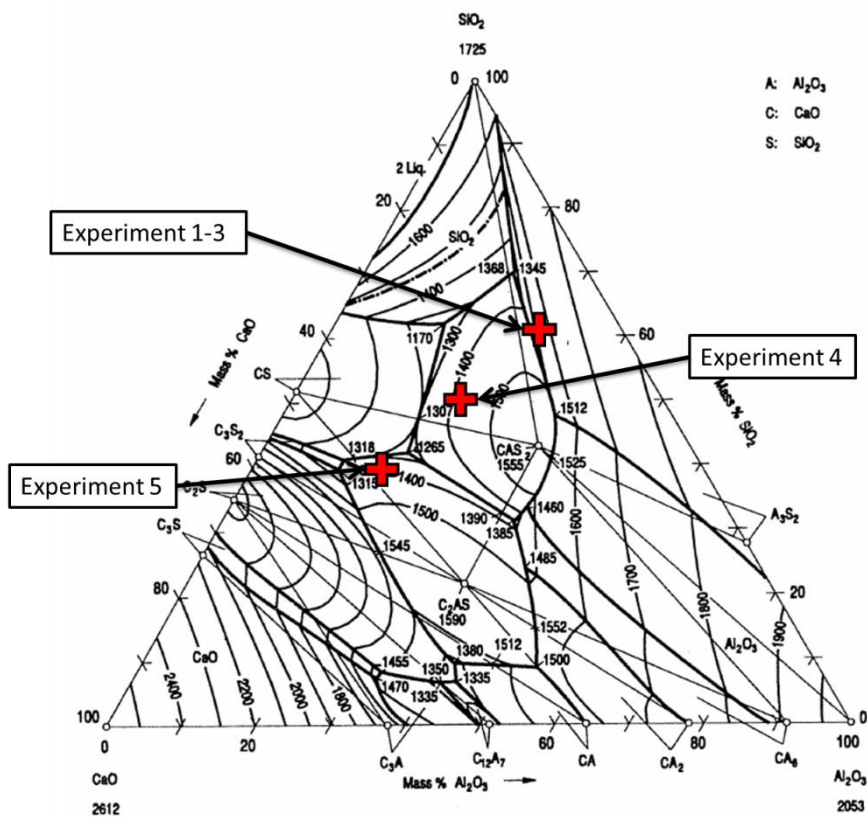


Figure 31: Estimated slag compositions in experiments 1-5.

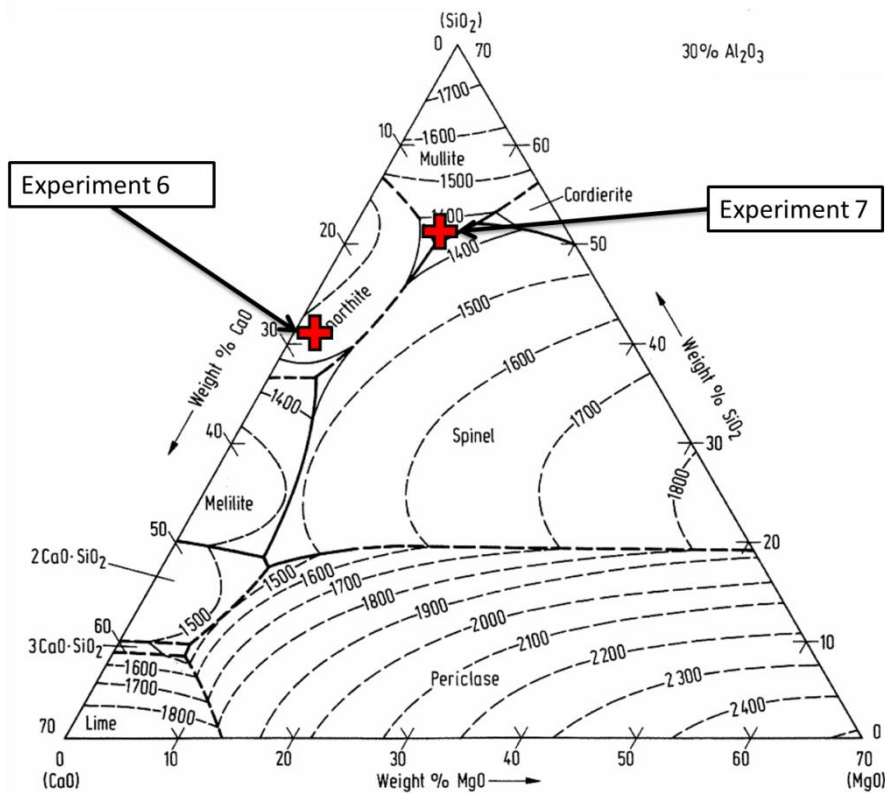


Figure 32: Estimated slag compositions in experiment 6 and 7. Alumina content is set at 30 wt%.

The furnaces used were the ASEA induction furnace at the Department of Materials Science and Engineering, a sketch of which is shown in Figure 33, and a similar induction furnace at SINTEF. The ASEA furnace was made in 1947, and operates at a maximum nominal frequency of 3830 Hz. It has a maximum power output of 50 kW with manual power control [58]. The lack of automation means that a significant experience with furnace operation is necessary to keep a constant heating rate and to maintain a specific temperature. There is a significant lag between changes in electrical input and the resulting change in crucible temperature, which means that inexperienced operators will find it difficult to keep the desired temperature constant. The thermocouple used to control the power is contained in the crucible wall, not dipped into the molten slag or metal, which will not give a precise reading of the actual charge temperature. This is treated in further detail in 5.2.4 Error analysis. The SINTEF furnace was used for the last three experiments because the generator for the ASEA furnace failed in mid-march. Neither furnace has a cover, so refractory glass wool was used to cover the crucible during the experiments.

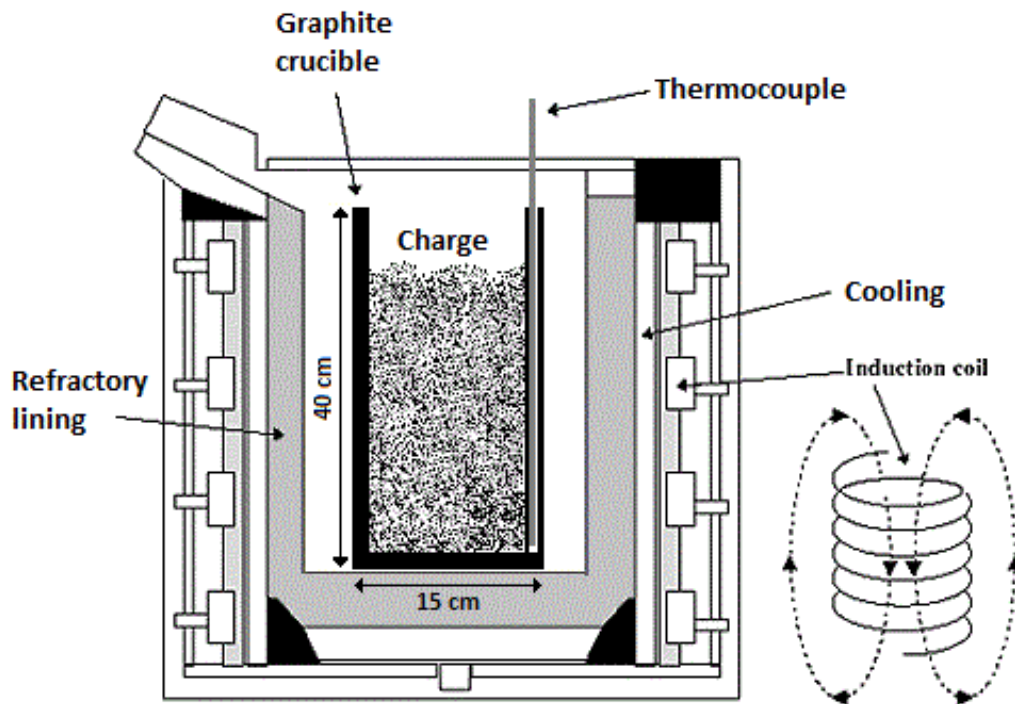


Figure 33: The ASEA induction furnace [59]

After the given holding time at 1600 °C, each crucible was taken out and air cooled to room temperature. Slag samples were chiselled out from the bottom, the middle and the top of each crucible, along the crucible wall. These were cast in epoxy to be analysed using a light microscope. In addition, slag samples were taken for chemical analysis. The silicon content of the samples was established using titrimetric analysis, and the slag composition was found using XRF. Metal samples were taken from the bulk of the produced metal and analysed by XRF.

The samples which were cast in epoxy were honed to shine using SiC-sandpaper and subsequent polishing steps. The polished samples were then photographed using mosaic-imaging at 100X magnification, where series of high-magnification images are taken and pieced together to make a larger high resolution image. An 8x8 images example of this is shown in Figure 34, below. The images are numbered in the sequence they were taken. The microscopy analysis was done using 16x16 mosaics, i.e. 256 images per sample.

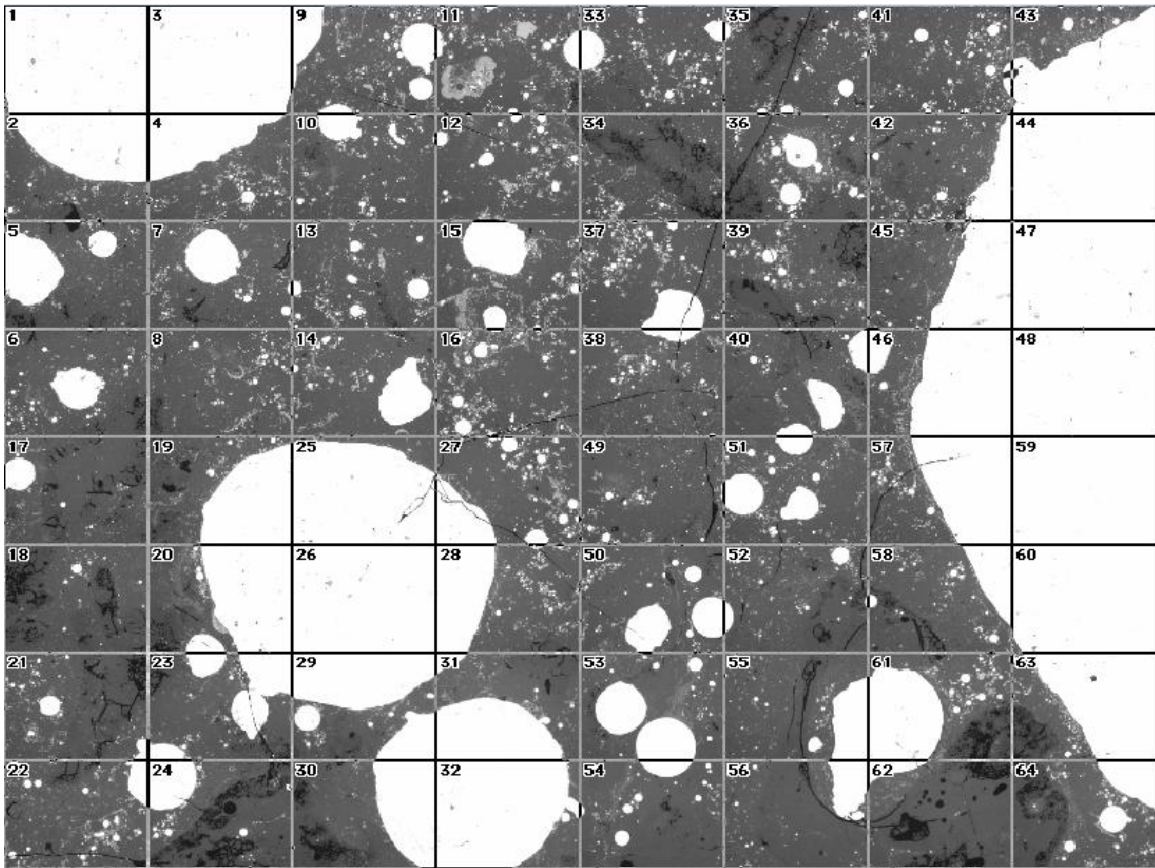


Figure 34: 8X8 mosaic image of a sample surface, each image was taken at 100X and joined into the larger image.

After 16x16 images were taken of the sample surface, the mosaic image was binarized using imaging software. Binarization means setting a threshold for color intensity and coloring the partitions in two contrasting colors. When the threshold was set, the imaging software was able to calculate the fraction of the image which was white, i.e. the area fraction of silicon in the sample. An example of this is shown in Figure 35 where the bright areas are colored green and the dark areas are white. It is important that the overall intensity (brightness) is identical for each sample, so that the threshold value can be constant for all the samples. If the brightness is not the same, then particles which are accounted for in one sample could be left out in the next. Therefore, all of the samples were done at the same light intensity using identical settings for the microscope.

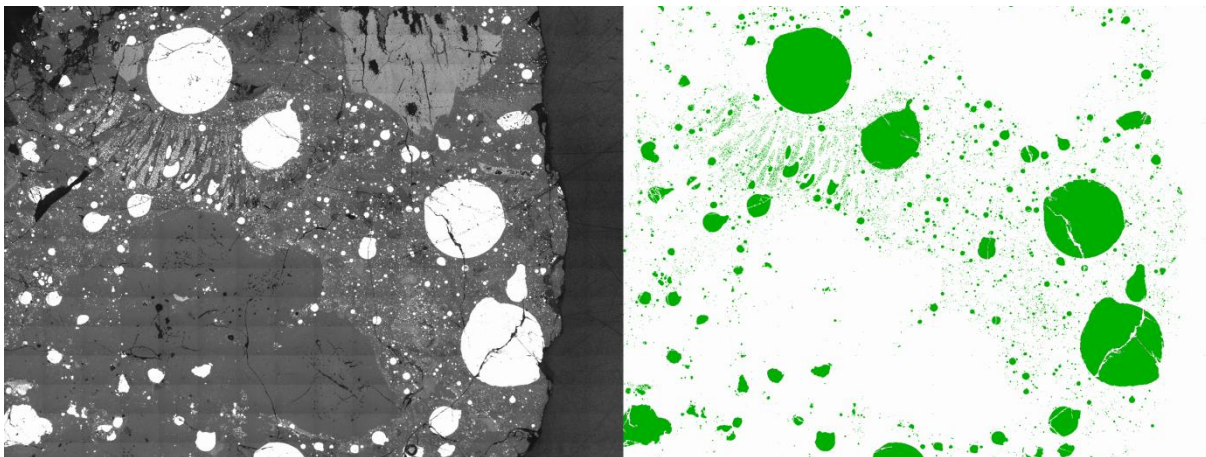


Figure 35: Left: The original mosaic image of a sample. Right: The binarized image of the same sample

4 Results

This chapter will present all the results from the various experiments done in this thesis, as well as the results from the various calculations. Results from previous work will also be presented. Some short explanation of graphs, tables or results will be given if deemed necessary, but the main discussion of the results will be given in chapter 5. A short brush-up on the experimental setup used for the various experiments will also be given.

4.1 Mechanical separation experiments

4.1.1 Dense medium separation

The aim of these experiments was to find the fluid density where either the slag or the silicon would float, while the other phase sunk. As magnetite was reported in literature to be viable up to 2.5 g/cm^3 [3], powdered magnetite was used to create the heavy medium. The finest fraction (M-10T) was used first, and the plan was to add magnetite to the stirred suspension until floating particles were visible at the top of the beaker. However, before this point was reached the viscosity of the mix became so high that the added particles could no longer move vertically. Even at maximum impeller speed, the suspension was too thick to allow for separation. Because of this, the coarser magnetite powder (M20-T) was used instead. Sadly, the viscosity of the suspension rose again to levels where vertical particle movement was impossible, and no results could be obtained.

4.1.2 Optical separation

The sample sent to Comex was analyzed by taking static pictures of particles from each fraction of the sample. Each image was then analyzed to find the optimal threshold value to identify the various phases of the charge. The analyzed charge was then separated by hand into a silicon rich product fraction and a slag rich waste fraction. An original image and the resulting analysis for each of the three fractions are shown in Figure 36 to Figure 38, below.

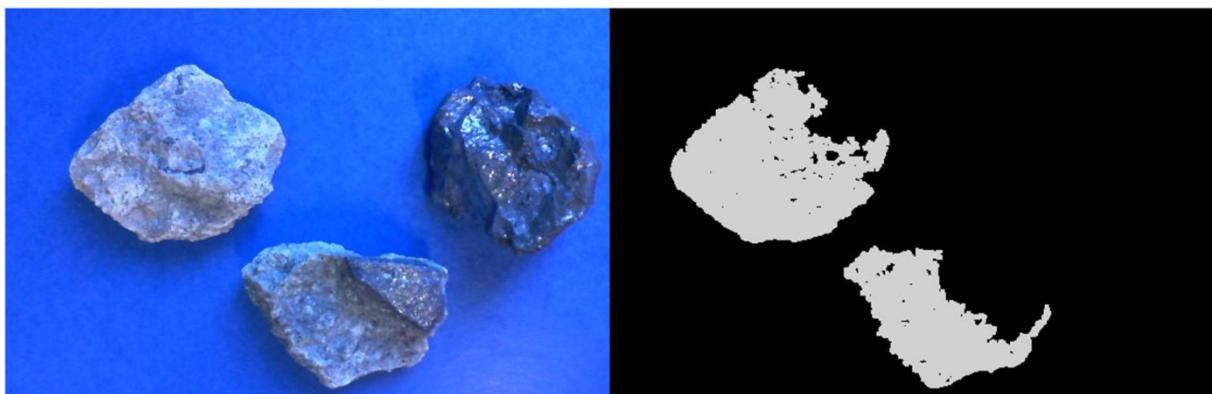


Figure 36: Original and analyzed image of the coarse fraction (40-80 mm).

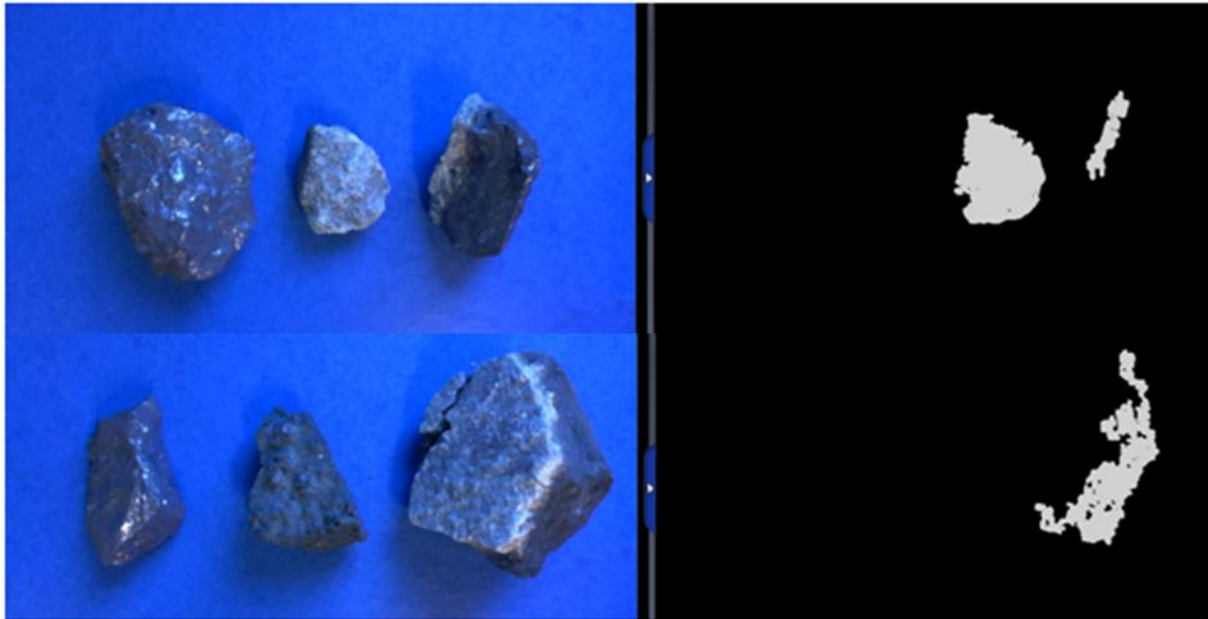


Figure 37: Original and analyzed image of the middle fraction (20-40 mm).

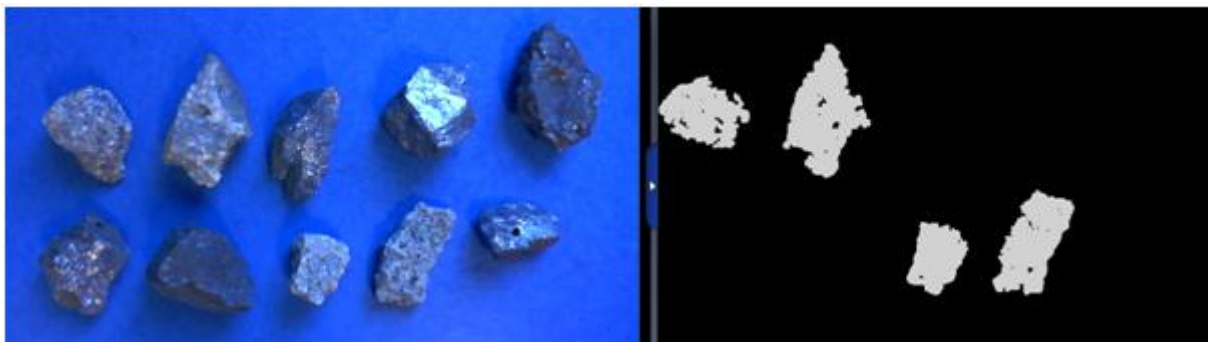


Figure 38: Original and analyzed image of the fine fraction (5-20 mm).

Classification was done with manual sieves, and the weight distribution between fractions is given in Table 4, below.

Table 4: Classification and weight distribution of the investigated fractions.

No	Size Fraction [mm]	Product [kg]	Waste [kg]	Sum [kg]	Total weight distribution
1	40-80	3.18	3.26	6.44	66 %
2	20-40	1.14	0.68	1.82	18.6 %
3	5-20	0.42	0.48	0.9	9.2 %
4	Under 5	-	-	0.6	6.1%
Sum				9.76	100 %

The separation efficiency figures, as calculated by Comex labs, are given below in Table 5.

Table 5: Separation result summary

No	Parameter	Value
1	Received material amount	9.76 kg

2	Material under 5 mm removed	0.6 kg (6.1 %)
3	Identification efficiency to both fractions	100 %
4	Amount of product recovered from the sample	4.76 kg (48.5 %)

The chemical compositions of the three fractions were analyzed in the same manner as slag from the remelting experiments, see chapter 4.2 Remelting experiments. The results are given in Table 6. The first row, which is marked as Si-met, gives the total content of metallic silicon in the samples. The subsequent rows give the chemical composition of the slag phase, i.e. the whole of the sample minus the metallic silicon content. Averages are weighted against the amount of charge in each fraction. The chemical analysis of the hand sorted charge has been included for comparison. It is important to note that the errors in the slag composition will increase exponentially as the amount of slag in the analyzed sample approaches zero.

Table 6: Chemical analysis of optically separated off-grades

Unit	Element	Hand sorted	Product Coarse	Product Middle	Product Fine	Product Average	Waste Coarse	Waste Middle	Waste Fine	Waste Average
kg	Weight	-	3.18	1.14	0.42	-	3.26	0.68	0.48	-
wt%	Si _{met}	82	77	68	69	74	6	9	15	7.5
wt%	SiO ₂	70.5	21.6	43.5	50.7	29.4	33.9	35.4	31.5	33.8
wt%	CaO	14.9	32.9	22.1	22.8	29.4	11.1	8.7	7.4	10.3
wt%	Al ₂ O ₃	12.2	41.3	31.4	25.1	37.5	54.0	54.6	60.0	54.7
wt%	TiO ₂	0.7	0.9	0.6	0.4	0.8	0.5	0.7	0.6	0.6
wt%	FeO	1.8	3.3	2.3	1.0	2.9	0.5	0.6	0.6	0.5

4.1.3 Flotation – zeta potential analysis

The results from the zeta potential analyses are given in Figure 39 as kilocounts per second of the interferometer as a function of the applied potential. The graphs are paired because each of the two samples was run twice, to reduce statistical errors. As seen in the figure, the graphs are almost totally overlapping, which means that flotation is not viable. The average peak value for silicon (red and blue graphs) is 34.5 mV ± 6 mV, the average peak for slag is 38 mV ± 4 mV.

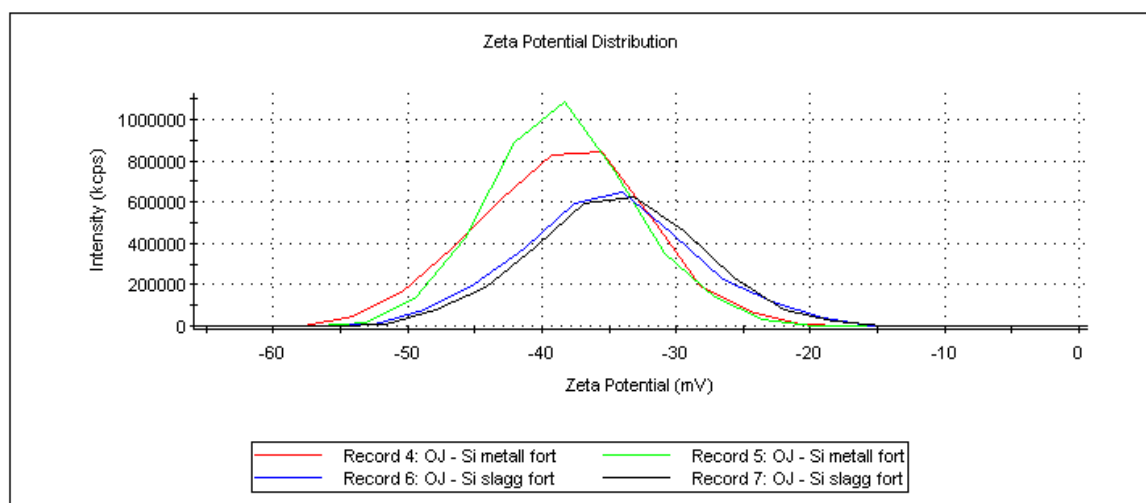


Figure 39: Results of the zeta potential analysis

4.2 Remelting experiments

Table 7 gives the analysis of the raw material used in the remelting experiments, which was slag taken from the slag pit at Elkem Thamshavn. Three samples of the raw materials were analyzed to see the normal variance in the off-grade. The values for Si_{met} were found using titrimetric analysis. The content of other elements were found using XRF, and are adjusted to show only the contents of the slag phase. Chemical analysis of the hand-sorted charge and the optically sorted charge can be found in chapter 4.1.2 Optical separation. As the raw material used in this thesis is not identical to the raw material used in previous work, the analysis of the previous raw material is also given [2].

Table 7: XRF analysis of slags and freeze linings.

Unit	Element	Slag	Slag	Slag	Slag average	Freeze linings
wt%	Si_{met}	52	52	52	52	41
wt%	Al_2O_3	23.9	24.8	23.6	24.1	29.5
wt%	CaO	14.2	13.4	12.6	13.4	9.5
wt%	SiO_2	61.5	61.3	63.3	62.0	60.5
wt%	Fe	0.33	0.35	0.34	0.34	0.61
wt%	TiO_2	0.10	0.15	0.09	0.12	0.26

The chemical analysis of the produced slag is given in Table 8. Values of Si_{met} were found using titrimetric analysis. The slag analyses were found using XRF, and the figures are adjusted to show only the contents of the slag phase. The same data are plotted in Figure 40, below.

Table 8: XRF analysis of produced slag

Unit	Element	Original charge	Upgraded Charge	Optically sorted charge	Low lime	High lime	Dolomite	MgO
	Ex. No:	1	2	3	4	5	6	7
Min	Holding time	30	30	30	10	10	10	10
wt%	Si_{met}	16.4	18.0	11.6	24.7	19.5	34.3	17.3
wt%	Al_2O_3	12.3	14.1	28.7	13.1	12.6	23.7	17.9
wt%	CaO	14.9	15.7	19.5	21.5	15.4	14.2	16.3
wt%	SiO_2	72.4	69.8	51.1	64.9	71.6	61.0	65.4
wt%	TiO_2	0.11	0.11	0.36	0.13	0.11	0.31	0.08
wt%	Fe	0.28	0.26	0.34	0.34	0.27	0.81	0.35

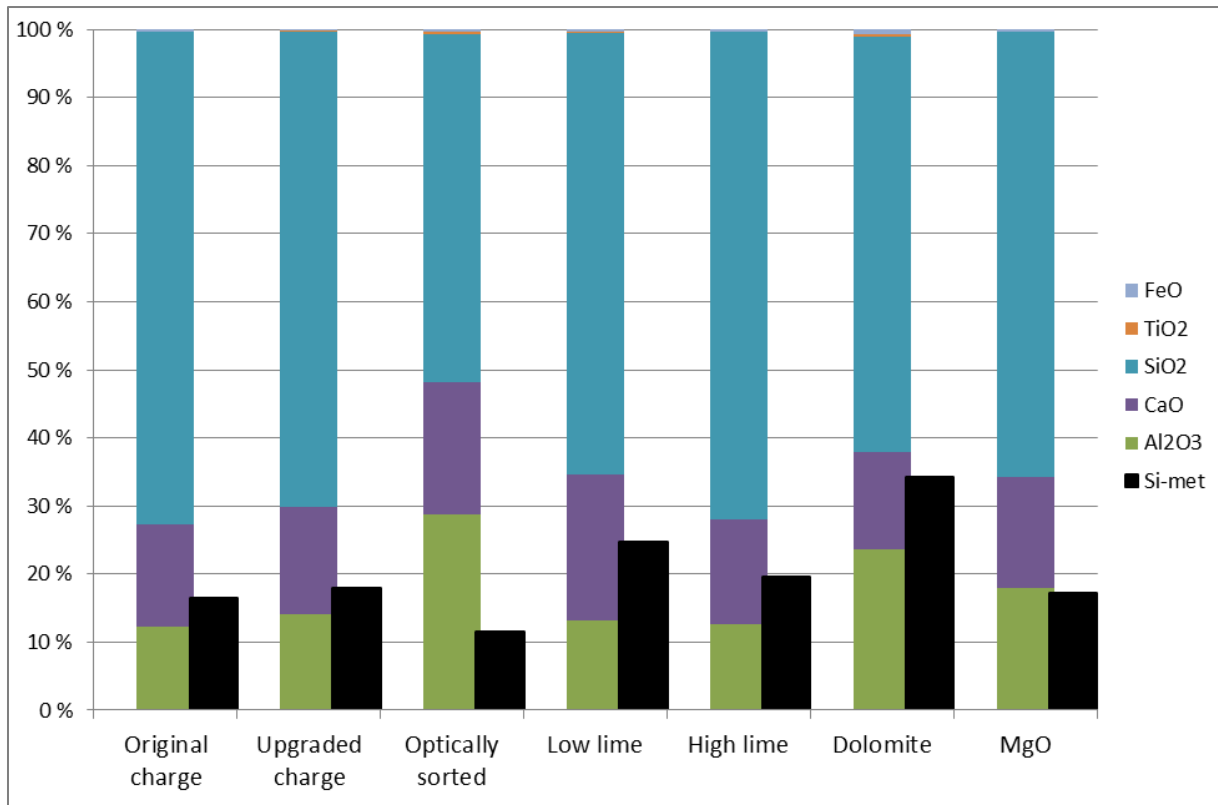


Figure 40: Chemical analysis of produced slag. Oxides are given as fraction of the total slag, where Si_{met} is not included.

The XRF analysis of the produced metal is given in Table 9. The same figures are plotted as a stacked column diagram in Figure 41.

Table 9: XRF analysis of produced silicon

Unit	Element	Unprocessed Off-grade	Original charge	Upgraded Charge	Optically sorted charge	Low lime	High lime	Dolomite	MgO
	Exp. No:	-	1	2	3	4	5	6	7
wt%	Si	98.90	99.5	99.6	99.30	99.4	99.2	93.57	99.46
wt%	Al	0.257	0.032	0.028	0.102	0.027	0.026	0.479	0.034
wt%	Ca	0.042	0.022	0.015	0.116	0.018	0.013	2.921	0.009
wt%	Fe	0.442	0.291	0.206	0.247	0.410	0.488	0.427	0.286
wt%	Ti	0.027	0.019	0.013	0.022	0.024	0.034	0.034	0.019
ppmw	Mg	0	11	6	1037	12	11	24122	527

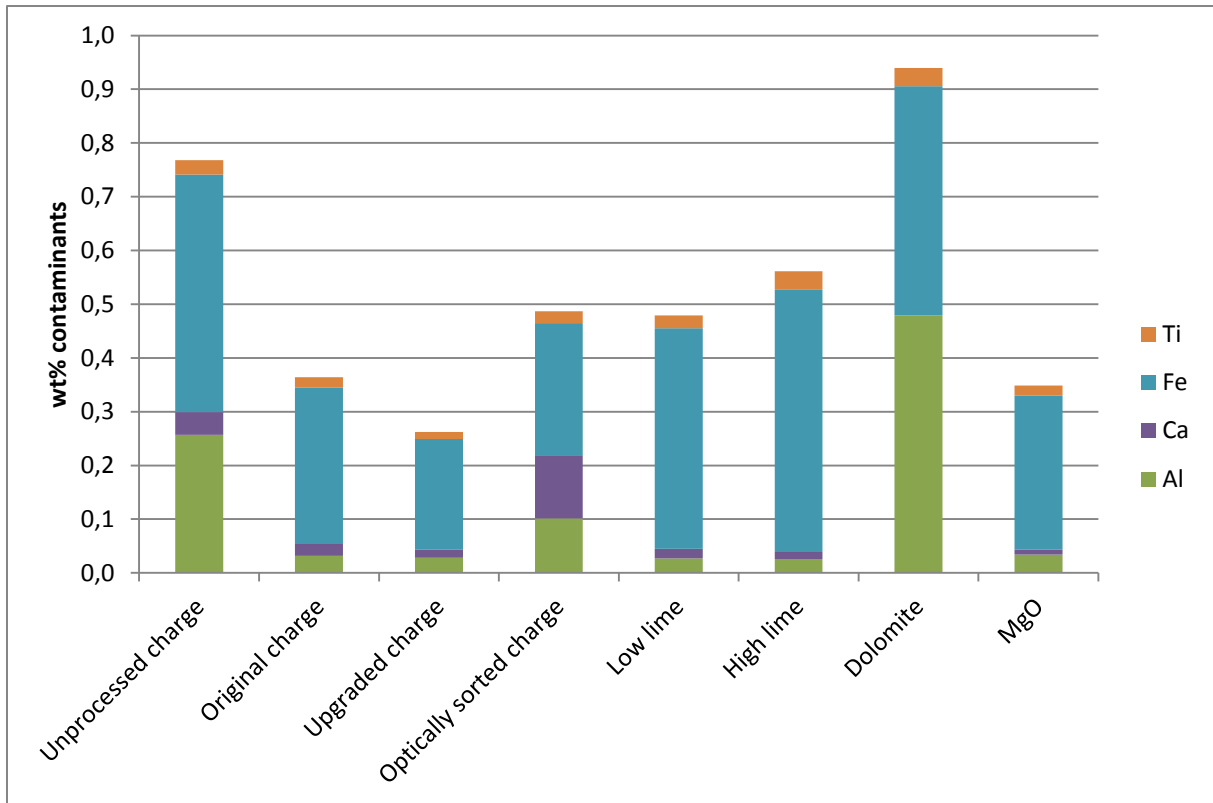


Figure 41: XRF analysis of the produced silicon

The area fraction of silicon in each of the slag samples taken from the remelting experiments were found by microscopy analysis. The results are given in Figure 42 and Figure 43, below. The average area fraction of silicon from each experiment is given in Figure 44, together with the silicon content of samples found by chemical analysis. A low bar indicates good separation of phases. The count data are given in full in the appendix.

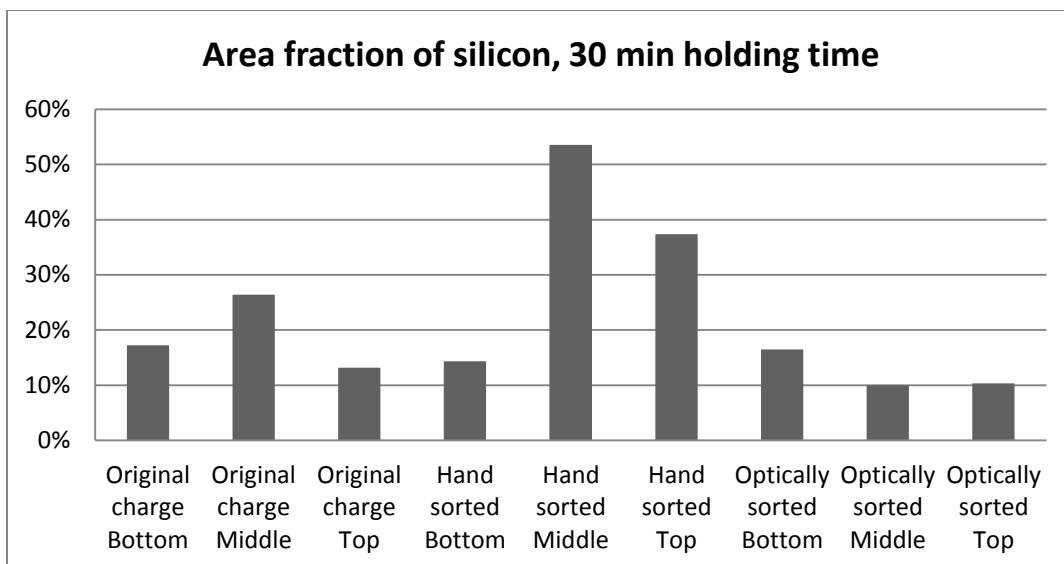


Figure 42: Area fraction of silicon in samples from experiment 1, 2 and 3, 30 minutes holding time

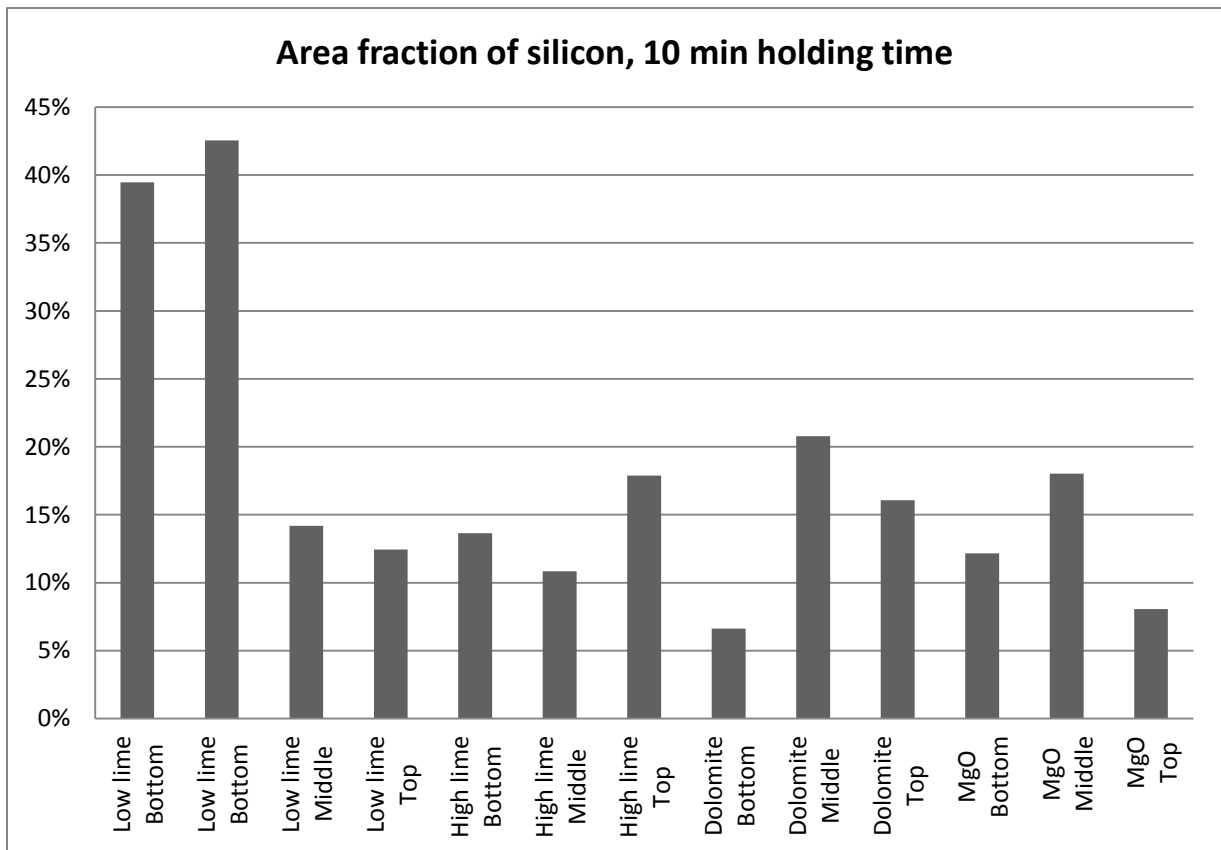


Figure 43: Area fraction of silicon in samples from experiments 4, 5, 6 and 7, 10 minutes holding time

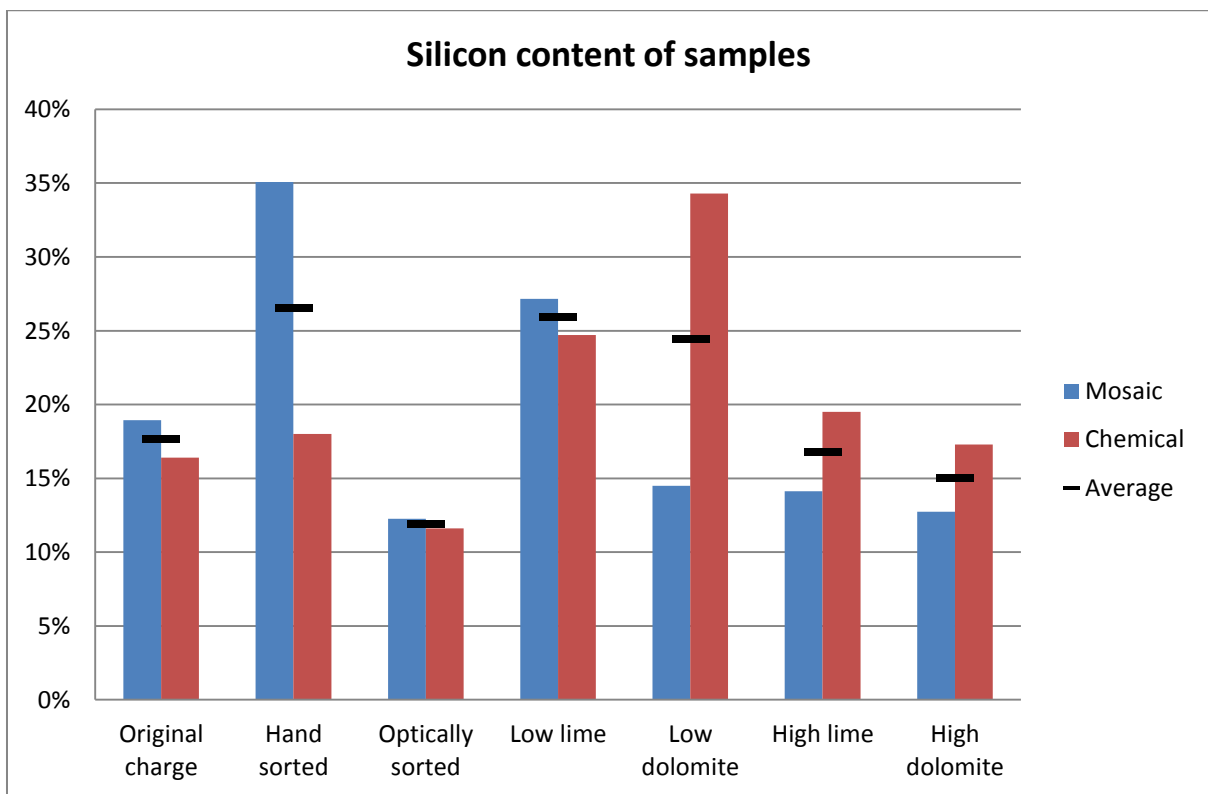


Figure 44: Average area fraction and chemically determined silicon content of slag in each experiment.

Because the previous microscopy done by the author was only done manually, the samples were redone using automated mosaic imaging. Both the result from the manual analysis and the result from the automated mosaic image analysis are given in Figure 45, below. The chemical analysis found is also included to show the variance between area analysis and chemical analysis.

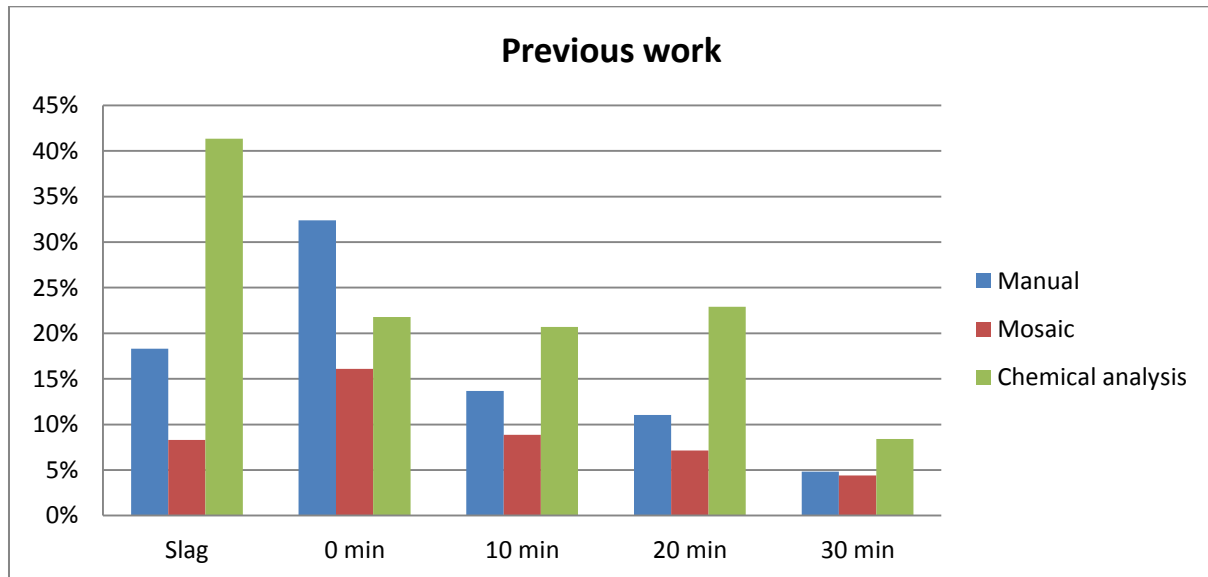


Figure 45: Previous work and new mosaic area analysis of slags from previous work.

4.3 Furnace design

Modeling is often the cheapest, easiest and best way of estimating dimensions and costs of a future investment, and is an essential tool when evaluating huge investments in metallurgical equipment. In this chapter, various models will be used to evaluate the dimensions, restrictions and designs of solutions for separating silicon and slags in off-grade materials.

The chapter will start with calculating how much of the off-grades could be recycled simply by adding them to the ladle during or after tapping. This is done by calculating the amount of heat available from the furnace, and calculating how much material this superheat can melt. The second part of the chapter will focus on dimensioning a new furnace for remelting off-grades using equations presented in chapter 2.3 Furnace design. Both the physical dimensions and the electrical parameters will be calculated, and possible furnace designs will be presented in terms of electrical and thermal efficiency. In the third and last part of the chapter, parameters for a freeze lining system will be calculated with results from the induction furnace dimensioning as input parameters.

4.3.1 Heat balance

The cheapest possible way of remelting off-grades would be to utilize the superheat from the furnaces. The off-grades would then replace the cooling metal, which is fine silicon material added to the ladle to reduce the temperature of the silicon before casting. The problem with remelting off-grade in this way is that there is no outlet for slag components. One would have to hope that the amount of silicon trapped in slag decreases when the total fraction of slag is increased, so that slag could be removed at regular intervals. Otherwise, another separation process would have to be

installed to remove slag components before remelting. This could for example be done by an optical separator set to remove only grains of (more or less) pure slag and pure silicon. That would have a double benefit as the total amount of off-grades is reduced, and the quality of the off-grade material to be remelted would be higher.

Calculating the available heat from the furnace will give the maximum potential of remelting in the ladle. This has been done using the software package HSC Chemistry v. 4.1 from Outokumpu Technology Oy [60]. The calculation assumes 5 wt% slag in the tapped metal, which corresponds well to figures from Elkem Thamshavn. The off-grade added is assumed upgraded to 70 wt% silicon, which should be a very moderate estimation of the separation capabilities of optical separators [3]. The rest of the off-grades is assumed to be 7,2 wt% Al_2O_3 , 4,0 wt% CaO and 18,6 wt% SiO_2 . They are assumed to be the only slag constituents, i.e. other contaminations are neglected. This corresponds reasonably well to the slag composition found by XRF analysis; see Table 7 in chapter 4.2. According to data provided by Elkem Thamshavn, the average tapping temperature in 2010 was 1590 °C, and the average temperature before tapping was 1466 °C. This gives a total superheat of 122 MJ per ton tapped metal, which is enough to melt a total of 43,4 kg upgraded off-grade per ton tapped metal. The average weight of a full ladle at Elkem Thamshavn's furnace #2 in 2010 was 7250 kg, so each ladle would be able to handle an average addition of 315 kg off-grade material. This would mean a maximum total remelting capability of about 2172 tons of off-grade per year, assuming that the furnaces continue to produce 50 000 tons of silicon per year. The average amount of cooling metal added in 2010 was 300 kg per ladle, 6 tons per day, for a total of 2190 tons [61]. The heat balance calculation seems therefore to fit very well to the actual conditions at Elkem Thamshavn.

4.3.2 Dimensioning an induction furnace for remelting off-grades

The main input parameters when dimensioning an induction furnace for remelting off-grades are tonnage, melt cycle time, chemistry of the charge material, electrical properties of the charge and the available power. In addition, a decision will have to be made on the mode of operation for the furnace. A furnace lined with a carbon susceptor will require a completely different approach than a furnace lined with electrically and thermally insulating refractory. Therefore, two different solutions will be presented. One where the charge is heated directly by the coil, using an electrically and thermally insulating refractory, and one where the charge is heated indirectly, with a lining made out of carbonaceous refractories.

The total production of off-grades per year at Elkem Thamshavn is about 5160 tons, which makes the basis for the minimum tonnage the furnace must be able to handle per year. If one assumes that the furnace would be run only during daytime shifts and only on weekdays, a minimum remelting capacity for the furnace of about 20 tons per shift or 2.5 tons per hour is required. Silicon at room temperature has a density of 2570 kg/m³ [1], giving a minimum total volume of the furnace of 0.97 m³. As mentioned previously, unprocessed off-grades consist of approximately 50 wt% slag, which gives a theoretical heat energy requirement of 2800 MJ/ton off-grade, or 7000 MJ per 2.5 ton batch, assuming that each batch is heated to 1600 °C [60]. If one then assumes that the melt cycle time is one hour per batch, including 15 minutes for tapping and recharging of the furnace, the power necessary to melt the material is 2.6 MW.

To produce a certain amount of power in the material, the same amount of power must first be supplied by the inductor, which will give an ohmic power loss in the copper coil. This power loss was calculated from equation (2.20), and depends on the quality of the copper conductor, the temperature of the coil and the space factor. Any impurities in the copper will reduce the conductivity of the conductor, so using a high-purity copper coil is important. The coil temperature is important because the conductivity of copper is inversely proportional to the temperature. Therefore, copper inductors are always water cooled. The copper quality of the coil was assumed to be 80 %IACS and the coil temperature was assumed to be 50 °C. Finding the space factor demands an assumption about the spacing between coil turns. In the present calculation, the spacing has been set to 5 mm. The height to diameter ratio of the charge was set at 1.8, following recommendations by Ahmed, Masoud and El-Sharkawy [34], giving an inductor height of 1.59 m and charge diameter of 0.88 m. They also recommend a layer of refractory of about 14 cm between the inductor and the molten charge, depending on the total capacity of the furnace, giving an inductor diameter of 1.16 m. As mentioned, the furnace can either be made in such a way that silicon is the magnetic susceptor and the charge is directly heated, or the lining can act as susceptor and the charge is indirectly heated. Direct heating will require low frequency (i.e. net frequency of 50 Hz) and indirect heating will require medium frequency (2-5 kHz) in order to operate at optimal skin depth in the material. Key figures from the two different scenarios will be presented below, and the calculation of all figures will be included in the appendix. The number of turns on the coil will depend on the space available along the furnace wall and the maximum current of the system. According to equation (2.25), the magnetic field strength is proportional to the ampere-turns of the solenoid, i.e. it depends both on the current and the number of turns on the solenoid. It is therefore possible to reduce the current by adding turns to the solenoid. This will not reduce the ohmic losses in the coil however, because the conductor must be longer to coil more times around the furnace. As seen from equations (2.20), the power lost in the conductor is proportional to the square of the current and the square of the number of turns. Therefore, the loss in the conductor is also proportional to the ampere-turns of the solenoid. Table 10 gives the physical dimensions of the furnace, and Table 11 gives the physical properties of the charge, the coil and the graphite lining. The dimensions and the physical properties are identical for the two cases presented below. Most of the data are also given in the illustration shown below Table 10, in Figure 46.

Table 10: Physical dimensions of the furnace

	Symbol	Value	Unit
Mass of charge	M	2500	kg
Volume of charge	V_m	0.97	m^3
Charge diameter	D_w	0.88	m
Height of inductor	l_c	1.59	m
Height/diameter ratio	X	1.80	
Surface area of molten bath	A_{bath}	5.63	m^2
Maximum meniscus height	Δh_{max}	0.17	m
Thickness of refractory	B_r	0.13	m
Thickness of insulation	B_{ins}	0.006	m
Inner diameter of inductor	D_c	1.16	m
Melting time	t	2700	s

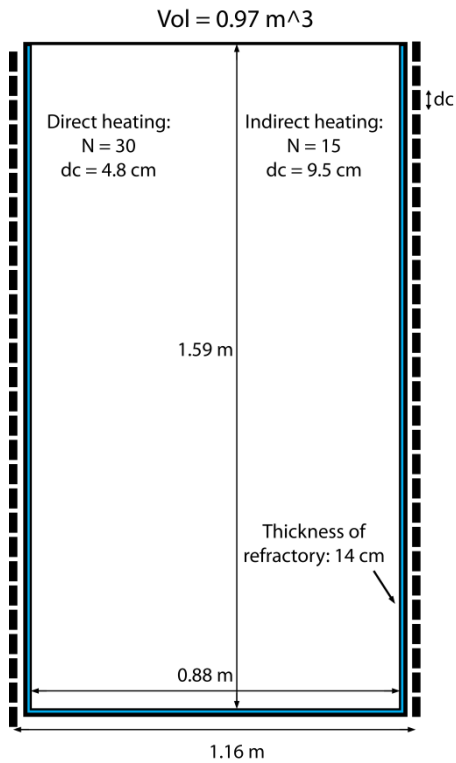


Figure 46: Schematic showing the dimensions of the furnace

Table 11: Physical properties of the system

	Symbol	Value	Unit	Source
Settling temperature	T	1600	°C	-
Electrical resistivity of charge	ρ_w	$1.00 \cdot 10^{-6}$	$\Omega \cdot m$	[32]
Electrical resistivity of graphite	ρ_g	$1.00 \cdot 10^{-4}$	$\Omega \cdot m$	[4]
El. resistivity of pure copper at 25 °C	ρ_{0c}	$1.72 \cdot 10^{-8}$	$\Omega \cdot m$	[33]
Temperature coefficient	-	$3.93 \cdot 10^{-3}$		
Temperature of coil	T_{coil}	50	°C	
Effect of impurities in copper	%IACS	80	%	
Electrical resistivity of copper conductor	ρ_c	$2.51 \cdot 10^{-8}$	$\Omega \cdot m$	
Density of charge	ρ_v	2570	kg/m^3	[15]
Vol% slag in charge	-	50	%	
Permeability of vacuum	μ_0	$1.26 \cdot 10^{-6}$	$V \cdot s/A \cdot m$	

In the first case of direct heating, the charge itself is the susceptor for the magnetic field. It was assumed that a sump of liquid silicon is used to melt the charge, and that the charge behaves as a monolithic, homogenous mixture with an electrical resistivity equal to that of liquid silicon at its melting point, $\rho_{Si} = 1 \cdot 10^{-6} \Omega$ [32]. This is likely to be a gross simplification of the actual conditions in the charge, but lack of data makes this simplification necessary. Because liquid silicon has a low electrical resistance, the necessary magnetic field was very large. The amount of turns on the solenoid has therefore been set to 30. This was rather high compared to the 2,7 MW iron remelting furnace calculated by Ahmed, Masoud and El-Sharkawy [34], which had 20 turns. The operating frequency has been set to the frequency of the electricity grid, 50 Hz, because this frequency is in

frequent use in other plants. The generator needed for the furnace will then likely be easily available at suppliers.

The second case will look at indirect heating from a lining made out of carbon (graphite or amorphous) or silicon carbide. The reason why this was an interesting case is that carbonaceous materials are good refractories against silicon and siliceous slags, and are excellent magnetic susceptors. Graphite is easily machinable, has a high resistivity, can easily be made monolithic and has a melting point of 3974 °C [4]. It will also react with silicon to equilibrium and generate a SiC lining, which is likely to be stable against silicon and siliceous slag [41]. The high resistivity of both graphite and SiC means that a high amount of ohmic heating will be generated when a current is passed through the lining, but it also means that the skin depth in the lining will be high, see equation (2.9). In order to reduce the skin depth to a value where all the magnetic flux was contained within the lining, the frequency had to be increased. This is why a higher frequency of 3000 Hz was well suited for the indirect heating scenario. The results of both scenarios are given in Table 12, below.

Table 12: Selected electric and magnetic properties

	Symbol	Direct	Indirect	Unit
Frequency	f	50	3000	Hz
Number of turns	N	30	15	--
Width of copper coil	d _c	0.048	0.095	m
Length of "wire"	l _{wire}	111	57.8	m
Skin depth in coil	δ _c	0.0119	0.0015	m
Skin depth in material	δ _w	0.071	0.092	m
Magnetic field strength	H	205	23	kA/m
Maximum magnetic field strength	H _{max}	82	82	kA/m
RMS current in coil	I _{rms}	12167	2755	A
Current in the charge	I _w	325623	36998	A
Dimensionless parameter	ξ _w	8.77	6.79	-
Power in the charge	P _w	2.60	2.60	MW
Power lost to cooling	P _{cooling}	731523	70247	W
Power needed	P	3.32	2.67	MW
Electrical efficiency	-	78	97	%
Total circuit resistance	R _t	19.87	96.16	Ω
Total circuit reactance	X _t	0.03	0.43	Ω
Total circuit inductance	L	8.64·10 ⁻⁵	2.30·10 ⁻⁵	Henry
Required capacitance	C	0.11741	1.2·10 ⁻⁴	F

4.3.3 Freeze lining thickness

Using equations 2.32 to 2.36, presented in chapter 2.3.4 Freeze linings, the heat flux needed to sustain a 5 cm freeze lining in a hypothetical slag remelting furnace has been calculated. The conditions in the furnace are assumed to be as equal to the calculations in the previous chapter as

possible, both with regards to physical dimensions and to process conditions. Important results will be mentioned, and the full calculation can be found in the appendix.

The first assumption which must be made is about the flow characteristic of the molten slag. This was important because the heat transfer coefficient between the melt and the lining directly depends on the flow characteristics of the melt. The flow is assumed to be governed by natural convection with laminar flow, i.e. the product of the dimensionless Grashof's number (Gr) and Prandtl's number (Pr) was between $8 \cdot 10^6$ and $1 \cdot 10^{11}$. The composition of the slag in the melt as assumed to be the same as has been found by XRF, see chapter 4.2 Remelting experiments. Values for the liquidus and solidus temperature, density (ρ), viscosity (μ) and thermal conductivity of slag (k_{slag}) has been found in the Slag Atlas [15]. The specific heat capacity (C_p) of each specie has been interpolated from figure 4 in Berman and Brown [62]. The height of the melt was assumed to be 1.6 m, i.e. the same furnace height as calculated in the previous chapter. This is the same as assuming that only the slag phase will act as a freeze lining, but because the slag is likely to have a higher melting point than the silicon, the assumption should be valid. Because of missing data for this system for the thermal conductivity of frozen slag, k_{freeze} , it has been assumed equal to 3 W/mK. According to Joubert [43], values between 1 and 3 W/mK are observed depending on composition, ergo 3 W/mK is the worst case scenario where the heat transfer is the highest.

The resulting heat transfer coefficient from the slag to the cooling system with the given assumptions and physical parameters was 32.4 W/m²K, and the heat flux which must be removed at all times by the external cooling system was 11.2 kW/m². As described by Joubert [43], the actual design of the cooling systems must be much more powerful than the minimum requirements to be able to handle process variations and unexpected events, like spalling of the freeze lining. A "safe" system must therefore be able to remove at least 45.1 kW/m², at a safety factor of 4. Important inputs and results from the calculation are given in Table 13, below.

Table 13: Selected inputs and outputs for the calculation of a freeze lining system

Inputs	Symbol	Value	Unit
Density of slag	ρ_{slag}	2200	kg/m ³
Volumetric expansion coeff.	β_{slag}	1.00E-04	-
Holding temperature	T_{slag}	1600	°C
"Average" freezing point	T_{freeze}	1447.5	°C
Temperature of cooling medium	$T_{cooling}$	20	°C
Height of melt	L	1.6	m
Dynamic viscosity	M	38.23	Pa·s
Specific heat capacity	C_p	1350.28	J/kg·K
Thermal conductivity of slag	k_{slag}	1.7	W/m·K
Freeze lining thickness	x_{freeze}	0.05	m
Thermal conductivity of freeze lining	k_{freeze}	3	W/m·K

Calculations	Symbol	Value	Unit
Flow characteristic number	$Gr \cdot Pr$	$6 \cdot 10^7$	
Nusselt number	Nu	69.51	
Heat transfer coefficient at hot face	h_{slag}	73.86	W/m ² ·K

Heat flux	q	11.26 kW/m ²
Total thermal resistance	R	0.031 m ² ·K/W
System heat transfer coefficient	h_{tot}	32.39 W/m ² ·K
Safety factor	X_{safe}	4
"Safe" capacity of cooling system	q_{safe}	45.05 kW/m ²

5 Discussion

This chapter will discuss the results and the repercussions they have for the possibility of upgrading off-grades at Elkem Thamshavn. Important aspects of the results will be emphasized, and possible explanations for negative results will be given

5.1 Mechanical separation experiments

5.1.1 Dense medium separation

The DMS experiments with magnetite as the dense medium failed. As described in the results, the viscosity of the medium rose to extreme levels long before the necessary density was reached. The maximum density given by Digre, Malvik and Sandvik was then probably a best case scenario, using high impeller speeds and rounded magnetite particles. The magnetite used was not rounded, and so the maximum density was severely lowered.

Future work should be carried out either with true dense liquids, or with ferrosilicon, which can have a much higher density range than magnetite, depending on the iron content of the FeSi. Using either of these liquids, it should be possible to determine whether a medium density exists where it is possible to separate slags from silicon. If such a density exists, an investigation of the economic potential of DMS should be carried out.

5.1.2 Optical separation

The results in chapter 3.2.2 Optical separation show that the rate of detection of slag components is quite good, as is the subsequent separation of silicon and slag. In the coarse fraction, see Figure 36, both slag containing particles are positively identified as slag, and the boundary between refractory and silicon in the contaminated grain to the left can easily be seen. The silicon grain is also perfectly identified as silicon, even though the reflectivity of the sample varies a lot across its surface. In the middle fraction, see Figure 37, the grain containing some lining material has been identified, but the slag-containing grain (center and middle of the picture) has not been identified. The analysis of the grain to the bottom right seems to have identified the whitest part of the refractory, but neither the darker refractory to the left nor the slag to the right. In the fine fraction, see Figure 38, all four slag containing particles are identified. Overall, this gives a good indication that upgrading off-grades by use of an optical separator is viable. However, the separation thresholds will have to be tuned so that all three phases are identified correctly.

The chemical analysis of the different partitions show a few interesting trends. First of all, the separation seems to be quite effective, although not as effective as indicated in the report by Comex, which estimated an efficiency of over 90 %. However, an average product quality of 74 wt% from initial trials is very good, since the process has not been optimized yet. As seen from the chemical analysis of the hand-sorted charge, the potential for improvement is still quite large. Since the optical separator uses the same physical properties as separation criterion (color, reflectivity, hue) and the same overall separation method, i.e. physical displacement of one of the phases, the two methods should have the same separation potential. The silicon content of the waste fraction is 7.5 wt% on average. If this is converted into tons of silicon lost annually, it would equal approximately 200 tons, depending on the amount of off-grades produced, and the average silicon content of the off-grades.

As expected, the separation efficiency seems to be best for the coarser particles, but the variation between coarse and fine particles is low. This might be an indication that the mineralogical

composition of the off-grades will be less important than the analysis errors of the separator in full-scale operation. If the impurities are mainly caused by contaminated grains, i.e. grains with several phases present, the low variation in silicon content might indicate that grains do not preferentially break along phase interfaces. There will then be an equal proportion of contaminated grains in each size fraction, and the variance between fractions will only depend on the separator efficiency.

There is a tendency for enrichment of alumina in the coarse product fraction. This is probably because of contamination of refractory lining, as the lining used at Elkem are made of a mullite/corundum mix (>50 wt% Al_2O_3) [45]. One plausible explanation why there is a tendency for concentration only in the coarse fraction is that larger particles can hide larger amounts of contamination from the camera, because of their lower surface area to weight ratio. As the size of particles increase, the specific area decreases, lowering the total area the camera can analyse. It is therefore likely that an optimal particle size exists where the available surface area is high enough for the maximum analysis efficiency, without overly sacrificing production capacity.

There are a few drawbacks with the method which will reduce its applicability. Firstly, all fines generated by handling of the off-grades will have to be removed before separation. A crushing stage must likely be installed before separation, since the machine can only handle a certain particle size, and this stage is likely to produce a significant amount of fines as well. As both slag and silicon are rather brittle, the loss to fines could become significant. Secondly, there will be a trade-off between loss of silicon in contaminated grains, and slag content in the separation product. If the aim is to get as pure a product as possible, the losses of silicon to contaminated grains would be high. But if the slag content of the product is too high, the selling price will be lowered and the overall economy would suffer. One way of dealing with this problem is to introduce a secondary crusher which will further crush the waste fraction before reintroducing its product to the process. All of the slag from the whole process would then have to be crushed into fines, but this will also free all of the silicon, giving maximum possible yield without sacrificing product quality, at the expense of increased crushing costs and reduced separator capacity. A flow chart for such a process has been outlined in Figure 47, below. The choice of separator setup will depend on the expected long term economic gain versus the extra investment cost, and will demand that large scale experiments are carried out before a choice is made.

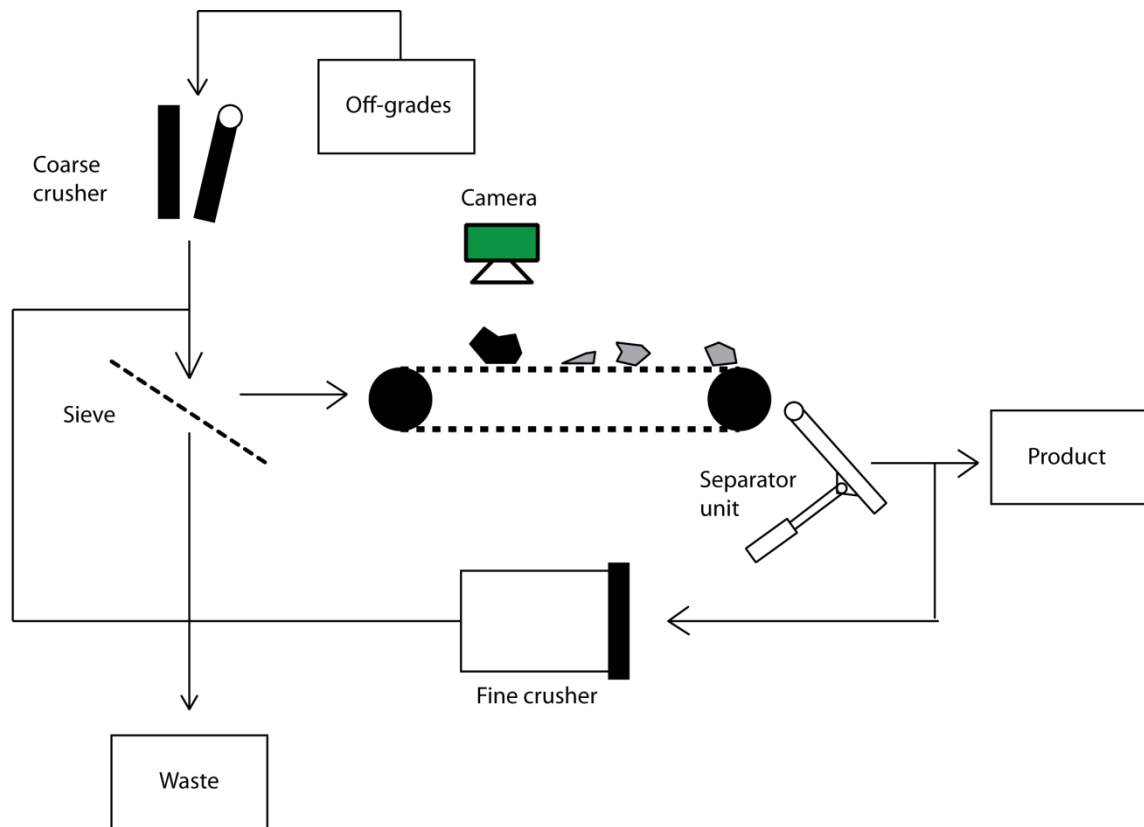


Figure 47: Flow chart for an optical sorting process with reprocessing of waste products

5.1.3 Flotation

The aim of the zeta potential experiment was to make a rough estimate of the potential for flotation without addition of surface activators. As seen in Figure 39 the peak of the curves for slag and silicon are almost completely overlapping. This means that the possibility for separation is approximately zero at neutral pH and without surface activators of any kind. However, the result is only valid for the current setup, and could change drastically when surface activators are introduced to the suspension. The next step in future work with the method would be to repeat the test while titrating with cheap, commercially available acids, like hydrochloric acid (HCl) or sulfuric acid (H₂SO₄), and bases like sodium hydroxide (NaOH) or potassium hydroxide. Because flotation is both expensive and complicated compared to other separation methods, it is important to test for cheap, safe options first. The HSE aspect of flotation can become very expensive if toxic chemicals are introduced to the process [3].

The results presented in this thesis should be regarded as a starting point for future work, if other separation methods fail. As mentioned in chapter 2.1.3 Flotation, the method is viable for more or less any combination of materials, because the surface qualities two materials of different composition will always differ. However, the more alike the two materials are, the less difference there will be in surface qualities, and finding an effective flotation sequence will be harder. It is therefore recommended to test other, less complicated separation methods first.

5.2 Remelting experiments

The remelting experiments were divided into two parts. In the first three experiments, the holding time was 30 minutes and no fluxes were added. Only an upgrading of the silicon content was done, first by hand, then by optical separation analysis. The aim of these experiments were to compare how the raw material used in this thesis would behave, compared to the sculls used in previous work, and to see the effect of increased silicon content of the slag. The holding time chosen was 30 minutes so that the results could be compared to the results from the previous work.

In the last four experiments, the holding time was reduced to 10 minutes. This shorter holding time was chosen because the effect of flux additions on settling efficiency was not known. It was therefore important to choose a settling time where the two phases were unlikely to be completely separated, so that any increase in settling efficiency would show on the results.

Because the microscopy analysis was done manually in the previous work, the samples from 2010 were analyzed again with automated mosaic imaging.

5.2.1 Chemical analysis

The chemical analysis is divided into three parts. The first part regards the contents of the charge, and is presented in Table 7. Three samples were analyzed to get an estimate of the expected variance in chemical composition of the charge. As seen from the low discrepancies in content between the samples, it is reasonable to assume that the charge is well homogenized. The slag composition is therefore equal for all of the remelting experiments, except for the optically upgraded charge.

Compared to previous investigations by the author [2] and to recommendations from Elkem engineers, the silicon content of the investigated off-grade is high (52 wt%, compared to 41 wt% and 40 wt%, respectively). This can either mean that the actual silicon content in off-grades is somewhat higher than estimated by Elkem, or that the batch which the off-grade originated from had higher silicon content than usual. Because of the large variations in off-grade composition, the latter scenario is the most likely. The slag analyses of the two different raw materials are actually quite similar. The freeze linings used in previous work show slightly increased alumina content, which is to be expected since there will be some refractory material chiseled off with the freeze linings. The iron and titanium content was also slightly elevated, which is likely caused by a random fluctuation in the silicon process, not by the processing of the freeze linings. It can be seen from the figure presented in Table 2 that the slag composition found by XRF and the calculated slag composition found using the figure, does not match up well. This is an indication that full chemical equilibrium is not in place in the ladle during tapping. When the off-grades are remelted, it is possible that this could change the calcium and aluminium content in the produced silicon. However, as seen from the figure, the slag has a lower CaO and an equal Al_2O_3 content than expected. Evidently, the refining process has been incomplete and remelting could actually improve the silicon quality with regards to calcium.

The second part of the chemical analysis is the XRF analyses of the produced slag. Starting with the three experiments held for 30 minutes, there are a few notable features. The silicon content ranges from 11.6 % in the experiment using optically sorted charge to 18.0 % in the experiment using charge which was upgraded by hand. Compared to the previous work this is very high, but the silicon content of the charge materials was also a lot higher than in the previous work. The off-grades contained 52 wt% Si, the optically sorted charge contained 74 wt% Si and the hand-sorted charge

contained 82 wt% Si. The increased total silicon content could have increased the necessary settling time. As the mean path between slag droplets increase, the time needed for droplets to meet and coalesce increases. The effective droplet size is therefore smaller, which reduces the settling efficiency. However, the results might also be a result of poor sampling. When the silicon content increases, the slag phase becomes smaller and finding slag samples which are completely free of the bulk silicon phase becomes harder. It is therefore difficult to say whether the results are completely representative of the slag phase, but they seem to indicate that increased silicon content leads to increased silicon content of the slag. The content of the slag in the first two experiments is quite similar, but the optically sorted charge has much higher alumina content. This is expected, as the optically sorted charge came from freeze lining, and the other experiments used slag as charge. No preferential removal of slag seems to have happened during upgrading of slag for experiment 2.

The experiments using CaO show a very interesting feature. The CaO content is lower for experiment 5 than for experiment 4, even though the addition of lime was almost twice as large. This indicates that the flux mixed poorly with the original slag, reducing the actual impact of the addition. As mentioned in chapter 3.3 Remelting and settling of silicon, the charging pattern was changed because of mixing issues. It is possible that the flux mixed very slowly in experiment number 5 as well, resulting in a reduced effective settling time. The only other explanation is a random variation in the particular samples taken. However, the analyzed material was taken from several sites on the crucible, so this is unlikely.

The experiments with MgO-additions gave inconclusive results. Experiment 6 where dolomite was added gave an elevated silicon content of the slag compared to experiment 4 where some lime was added, but experiment 7 with MgO gave slightly lowered silicon content compared to experiment 5, using lime. This might indicate that MgO and CaO are interchangeable fluxes, but the variations are far too large to draw a conclusion.

The third part of the chemical analysis regards the quality of the produced silicon. As stated in the introduction, the aim of this thesis is to find a way to "...recover high-grade silicon from off-grades..." It is therefore of utmost importance to analyze the produced silicon and establish whether the processing has been detrimental to the product quality. It can be seen from Table 9 that this is not at all the case. The iron content of experiments 4 to 6 is slightly elevated and the sample taken from experiment six obviously had some dolomite grains in it, but the other samples are even purer than the original silicon product. It is therefore possible to conclude that the remelting process has not reduced the quality of the silicon, and that producing high quality silicon by remelting off-grades in an induction furnace is possible.

5.2.2 Microscopy analysis

The aim of the microscopy analysis was to find the amount of silicon trapped in slag as a function of slag additions. This could then be used to estimate the impact the various additions had on the settling efficiency and the quality of the produced metal. The first obvious feature of the microscopy analysis was that the variation between samples was very large, mainly because the area fraction was dominated by the largest particles in the samples. If a large particle which should perhaps have been counted as part of the bulk phase is present in the sample, the area fraction silicon of that sample was increased dramatically. The variance from sample to sample was often several percent, and the only noticeable trend within experiments was that the silicon content was often higher in the

sample taken from the middle of the crucible than those taken at the top and the bottom of the crucible. This is a logical consequence of the flow pattern in the furnace. Because the external magnetic field forces the melt to move in a circular motion, the flow speed of the melt was highest near the middle of the crucible. The slag in these areas would then entrain more silicon as a result of these higher speeds, cf. equation (2.7) in chapter 2.2.5 Melt stirring speed.

There were still trends in the overall area fraction of silicon from one experiment to the next. It would seem that slag additions were effective in increasing the settling efficiency, because experiments 4-7, which were only held for 10 minutes at 1600 °C, showed similar or even lower area fractions of silicon than experiments 1-3, which were held for 30 minutes. It would also seem that adding MgO was more effective than adding CaO, but because of the large variance in the results, this conclusion is uncertain. As explained in chapter 2 Theory, MgO should have some advantages over CaO, but the results from the XRF-analysis of the produced metal showed increased Mg levels in the produced silicon. Luckily, the oxygen affinity of magnesium is very high, so by introducing a short refining step to the process, where oxygen is blown through the melt, the added magnesium should be easily removed [1].

In Figure 44, the average area fraction of silicon is plotted together with the results of the chemical analysis. It can immediately be seen that there is a rather large discrepancy between the chemical analysis and the mosaic image area analysis. The difference was extremely large in experiment 2 and 5, which indicates that a large part of the bulk silicon has entered the samples. The average value between the two analyses has also been included. The conclusion from these average values was however the same as the conclusion from the mosaic imaging analysis: Adding slag fluxes seem to increase the settling efficiency, and the magnitude of the effect depended on the amount of flux added. MgO additions seemed to give a slightly better product, but the results are inconclusive.

The samples taken from the previous work were analyzed again using automated mosaic imaging. This was done so that previous results and current results could be directly compared. It can be seen from Figure 45 that the manual analysis gave higher fractions of silicon than the automated analysis, which indicates that the previous work did not get a representable value for each sample. The chemical analysis of silicon content is added for comparison. As the chemical analysis used larger samples, the accuracy of the analysis should be better. However, as will be explained in the next chapter, separating slag samples from the bulk silicon was very hard. It is therefore likely that some of the bulk silicon was included in the slag samples, overestimating the actual silicon content of the slag phase. It can be seen from Figure 45 that the chemical analyses do estimate quite a lot more silicon in the samples than the area analysis. The overall trend is the same however: The silicon content decreases with increasing settling time.

Comparing the current results with the previous results, it can be seen that the silicon content of samples in the current work was higher than for the previous work. Such a comparison is shown in Figure 48 and Figure 49, below. The previous results are superimposed onto the current results in the figures. The elevated silicon content could simply be a result of the slight difference in slag chemistry and the original silicon content of the charge, but a few factors were changed from the previous work which could have impacted the settling speed. Crucibles used previously had slightly thicker walls, and no hole for a thermocouple. A graphite tube was therefore used to hold the thermocouple, giving more accurate temperature readings of the actual charge temperature.

However, bridging was a much larger problem previously, which could have altered the settling speed by increasing the thermal insulation somewhat. The greatest difference between the raw materials was that the freeze linings had significantly lower silicon content (41 % vs. 52%), giving a larger slag phase. This made extracting samples much easier, giving less interference from the bulk silicon and therefore lower estimates of the silicon content of the slag.

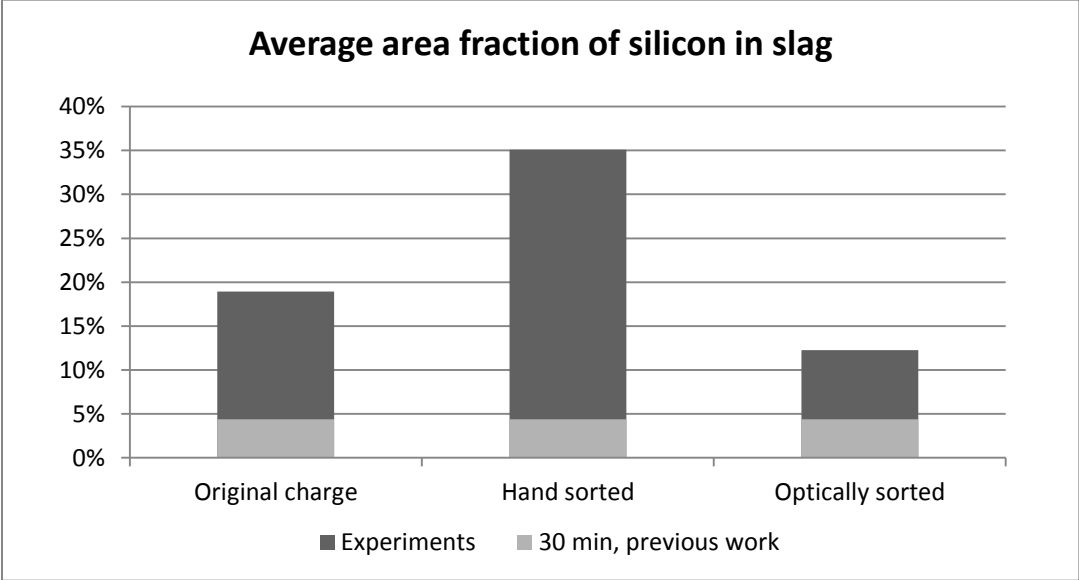


Figure 48: Comparison of the first three experiments to previous work with 30 min holding time

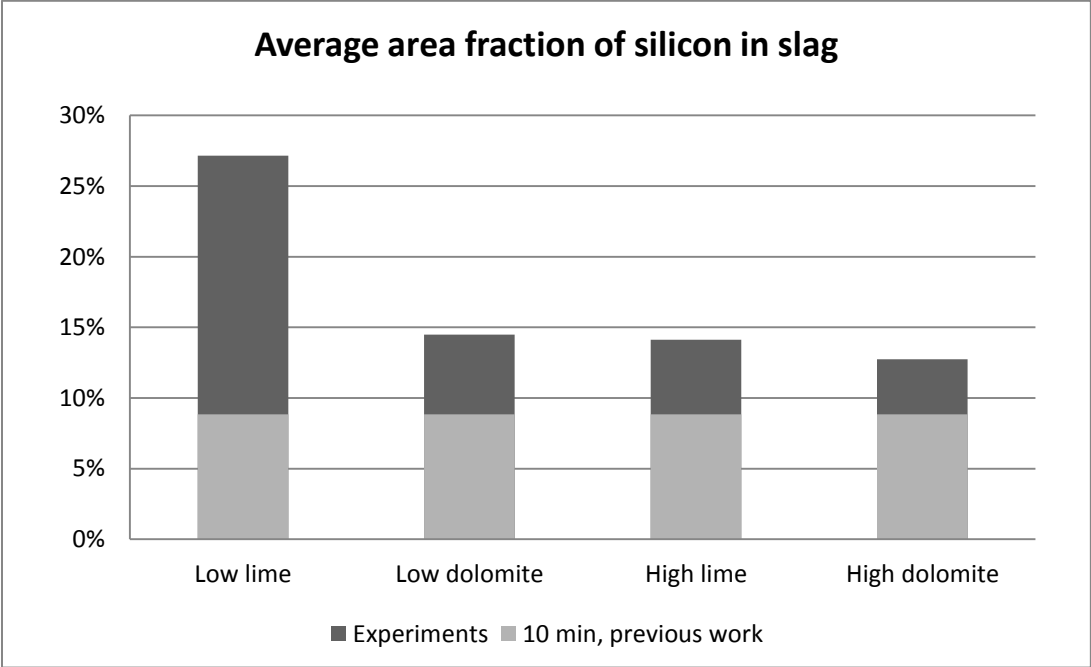


Figure 49: Comparison of the last four experiments to previous work with 10 min holding time

From the results presented, one can conclude that area fraction analysis of silicon in slag samples has not been a very good way of determining the silicon content. Not because of the method itself however, but because of the extreme heterogeneity of the samples and because sample extraction

was difficult. Should further work be undertaken with off-grades, it will be important to increase the number of samples investigated, so that the area fraction analyses will be more representative of the experiments.

5.2.3 Experimental difficulties

As explained in chapters 2.2.2 and 2.2.3, the low density difference between slag and silicon and the high viscosity of the slag posed a range of problems to settling of silicon from off-grade materials. The extreme viscosity of the slag coupled with a seemingly low interfacial tension between slag and graphite lead to close adhesion of the slag to the crucible wall during the remelting experiments. In addition, as explained in chapter 2.3.2 Furnace design, the magnetic field used to heat the charge will stir the molten metal and slag. As the molten material flowed towards the center of the crucible, silicon droplets would meet and coalesce into a larger bulk. Because only the slag phase seemed to have an affinity for graphite, the slag/metal interface was vertical instead of horizontal as expected when liquids spontaneously separate into two phases. Figure 50 shows a horizontal section of a crucible, and one can see how the slag is contacting the wall, while the silicon has formed a bulk phase in the center of the crucible. This is why all the samples extracted from the experiments had to be collected from near the wall of each crucible. It is expected that the issues with adhesion and a vertical interface will diminish as the batch size is increased and gravitational forces exceed surface tension.

Taking out samples from the crucibles posed a problem of its own. The produced silicon and slag is hard, but very brittle, so when slices were cut from the crucible the contents would often crumble into pieces which were too small to be cast in epoxy. Also, the amount of slag in experiment 2 and 3 was so low that finding whole pieces with a diameter suitable for casting in 3.5 cm molds was difficult. Therefore, only three samples were liberated from each crucible. This will add some statistical error to the results.

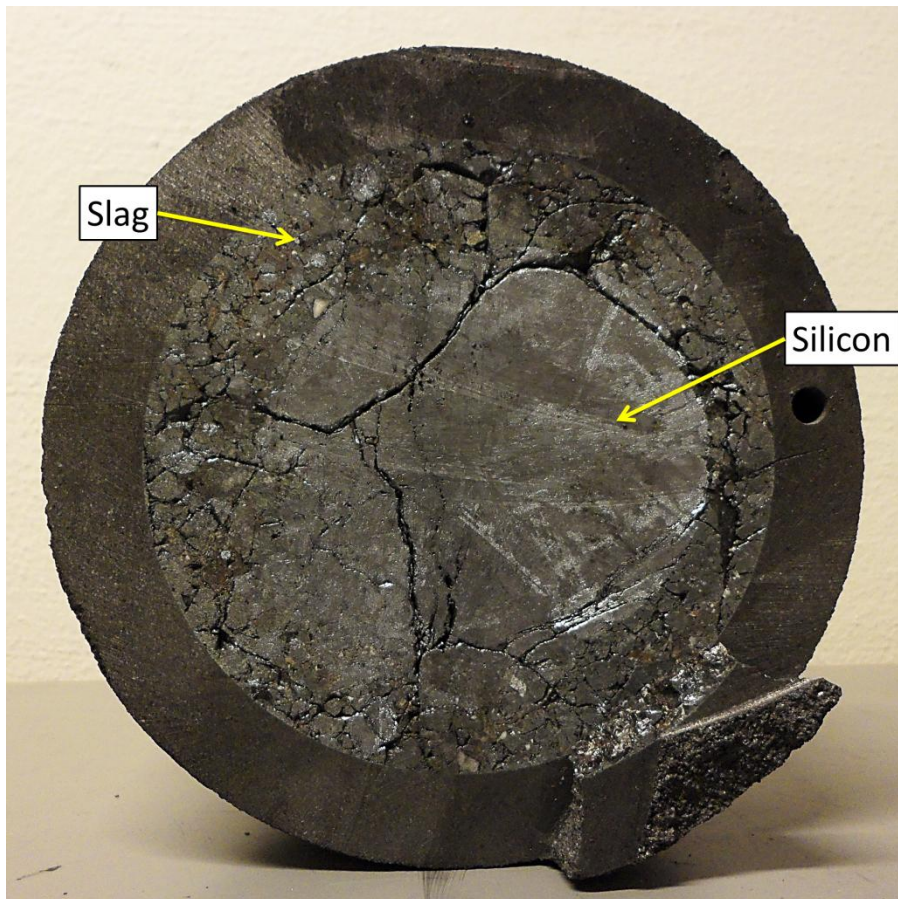


Figure 50: A horizontal section through the crucible from experiment 7.

During the experiments with slag additions, namely experiment 4-7, there was a problem with evolution of CO_2 from the carbonate additions. The production of gas was expected because both CaCO_3 and MgCO_3 will release CO_2 when heated to about $800\text{ }^\circ\text{C}$ [41]. It was however not expected that the charge near the top of the crucible would sinter into an air-tight bridge which would trap the evolving gas. As the temperature increased, the CO_2 pressure increased and the whole charge was lifted from the bottom of the crucible and ejected. The result can be seen in Figure 51. In previous experiments, breaking the bridge using manual force has posed only few problems, but because the ASEA furnace at NTNU broke down, a newer furnace at SINTEF was used for experiments 4-7. That furnace had a longer inductor, better insulation and a more powerful generator, resulting in a lower temperature gradient as a function of crucible height. The lower gradient gave a longer region where the temperature was high enough for the charge to sinter, but low enough that it did not melt. Therefore, the bridge became longer and stronger than it used to be in the ASEA furnace, and breaking it by manual force was impossible. In future work, larger diameter crucibles should be used, if possible. This would lessen the bridging problem as the strength of the bridge is a function of the crucible diameter. It would also lessen problems with slag adhesion and liberation of samples. The bridging phenomenon should not pose a problem in full scale operation with large diameter crucibles.



Figure 51: Failed experiment where the top of the charge sintered into an air-tight bridge which the building CO₂ pressure ejected from the crucible.

As mentioned in chapter 3.3 Remelting and settling of silicon, the charging pattern was changed in experiment 7. In experiments 4, 5 and 6, the fluxes were added before the off-grades were added, giving two distinct sections in the crucible. However, when large amount of fluxes were added, the fluxes did not mix properly with the melt. The fluxes have a much higher melting point than the slag. Pure CaO for example has a melting point of 2572 °C, which is far above the holding temperature in the remelting experiments. The added flux would therefore only partially mix into the melt, creating a zone of high-melting slag which stopped the rest of the fluxes from mixing with the slag. The result of one of the failed experiments is shown in Figure 52, below. The bottom of the crucible has just been cut off, and the flux has poured out. Because of these two failed experiments, the charging pattern was changed in experiment 7. Instead of adding the flux to the bottom of the crucible, the flux was mixed with the off-grades before charging. This gave better packing of the crucible, higher porosity so evolved CO₂ could escape more easily, the bridging phenomenon was reduced and the flux seemed to mix better with the melt. However, since the fluxes were now also present at the top of the crucible, more flux was lost with the off-gas than with bottom charging. The heating rate had to be slower as well to avoid losing too much flux with the off-gas. Overall, the benefits of mixing the fluxes with the off-grades before charging outweighed the disadvantages, and future work should use the same charging pattern.



Figure 52: Failed experiment where the flux did not mix properly with the slag.

5.2.4 Error analysis

As mentioned several times throughout this thesis, the statistical errors in the remelting experiments were large, both because of the large variation in off-grade quality and because of the large differences in scale between the lab work and industrial application. This chapter will try to summarize all the statistical error factors encountered, and roughly estimate their impact on the conclusions.

The first and largest source of error came from the raw material itself. “Off-grades” is a category which contains a whole range of different materials. Slags from the slag pit, sculls chiseled from used ladles, produced silicon with too high impurity levels and the occasional ladle which has been left to freeze during process interruptions; all enter the same pile. The chemical composition, silicon content and impurity level will therefore vary greatly, which means that a very large sample from as many batches as possible would have to be taken. One way of estimating the required sample size, is by using Gy’s formula [3], presented in equation (5.1), below.

$$M = f \cdot g \cdot h \cdot m \cdot \frac{d^3}{s_r^2} \quad (5.1)$$

$$m = \frac{1 - a}{a} [(1 - a)r + at]$$

Gy’s formula states that the required mass is a function of physical parameters, the sample grain size and the required sampling accuracy. The parameters are the shape factor f , the grain distribution factor g , the comminution factor h , which accounts for the degree of free crushing at the specific

sample grain size, and the mineralogical composition factor m , which accounts for the density difference between the silicon and the slag (r and t), and the amount of Si in the sample (a). The f , g and h factors used to calculate the necessary sample amount were recommended by Digre, Malvik and Sandvik. Their values are $f = 0.5$ to represent common grain shape, $g = 0.25$ to account for a full spectrum of grain sizes, $h = 0.3$ to represent the degree of free crushing. The mineralogical composition factor was calculated with $r = 2,5 \text{ kg/dm}^3$, $t = 2,6 \text{ dm}^3$ and the amount of silicon in off-grades is assumed to be 50 %, which gives $m = 2,5$. It is assumed that the grain size of the off-grades is 90 % below 5 cm ($d = 5 \text{ cm}$) and that a minimum sampling accuracy of $\pm 5 \text{ wt\%}$ silicon is demanded. Inserting these numbers into equation (5.1) gave a minimum sample size of 1 172 kg. Decreasing the accuracy will reduce the sample size, but even at $\pm 10 \text{ wt\%}$ accuracy the sample size will still be about 300 kg. In other words, far too much work is needed in order to be sure that the sample will be representative for off-grades as a whole. It was therefore decided to take a large sample from a single tapping, and work from chemical composition of that specific batch. The sample would then be representative of that particular tapping, and could only give qualitative results for off-grades as a material category.

Finding representative samples from the crucibles posed the same problems as finding representative raw material. The remelted slag is also very heterogeneous, so the variation in silicon content from one slag sample to the next can be large. The solution to this problem is taking more and larger samples, but as explained in the previous chapter, liberating slag samples of sufficient size was very difficult. In further work, larger batches should be treated so that the slag phase becomes larger, and sampling becomes easier. Overall, the heterogeneity of the slag and the resulting variance in slag composition is probably the largest error in the remelting experiments.

The second important statistical error encountered in these experiments is the settling time. There was no way of knowing when all of the charge has melted, other than trying to stir the contents of the crucible with a graphite rod to determine whether the charge is molten. Therefore, knowing exactly when the melting point had been reached was difficult. To make the task even harder, the thermocouple had to be contained within the crucible wall, not in a separate graphite tube, because the reduced crucible aperture would lead to increased bridge strength. Since the graphite crucible was more inductive than the charge and closer to the coil, it was carrying most of the generated eddy current. The temperature reading in the wall was therefore likely to be higher than the actual charge temperature, so the thermocouple readout could not be used to estimate when the melting point of the charge was reached. Because of the above, a range of perhaps 8 – 15 minutes must be set as the actual settling time. This discrepancy will probably add significantly to the total error, and in future work, thermocouples must be installed in the center of each crucible to monitor the state of the charge.

The third important error source was the holding temperature. Because induction heating works by inducing currents in the work piece itself, the power produced is a function of the current in the work piece. As the temperature increases, the resistivity of the charge will change, and for silicon there will be a sudden drop in resistivity upon melting [32]. Solid silicon has a very high electrical resistance of up to several ohm [31]. In addition, gaps in the charge between particles will add a lot to the effective resistance. Therefore, the charge carries almost no current before it is molten. As silicon melts, it will start to carry a current and contribute to the power input to the charge, meaning that the total power to the system will rapidly increase as more and more silicon becomes molten. This

spike in power lead to the charge being heated somewhat above 1600 °C before the temperature could be stabilized again. The temperature was however rarely above 1630 °C, and since all samples were treated in approximately the same way, the overall impact on the results is unlikely to be large.

A few less important sources of error were loss of material during handling, contaminations, weighing errors, and segregation of fluxes and charge in the crucible. Some of the flux added to experiments 4-7 was lost during gas evolution as the pressure was released through the charge, but some of the off-grade was also lost in this manner, so the overall impact was probably very small. The weights used were accurate to ± 10 g, which was insignificant compared to the whole charge of 4-5 kg. It is possible that the stirring of the molten charge was low enough that fluxes never became completely mixed with the original slag. There is no way to know whether this occurred, but the fact that the CaO level in experiment 5 was lower than in experiment 4, even though the lime addition was twice as large, indicates that it happened. The most likely source of contamination of the charge was the crushing stage before remelting. An ordinary jaw crusher with steel jaws was used to crush the off-grades, giving a slightly elevated iron content of the produced silicon. Because iron is readily reduced by silicon, all the contamination would have ended up in the silicon phase [1]. The only other conceivable contamination would be an increased carbon content because of reaction with the crucible wall, which would lead to a higher carbon content of the slag.

The conclusion from this analysis is that the errors were likely too large for the results to be quantitative, mainly because the slag is too heterogeneous. Only qualitative conclusions can be made from the remelting experiments. It is likely that quantitative conclusions can be made only in full scale, because the aforementioned issues will dominate small scale tests.

5.3 Furnace design

5.3.1 Heat balance

The heat balance model seemed to fit quite well to the actual use of cooling metal at Elkem Thamshavn, with an estimated error of less than 1 %. This is surprising, because the model does not include heat losses from the ladle nor does it include the extra heat produced by refining. As mentioned in chapter 2.2.1 The Al_2O_3 -CaO-SiO₂ slag system, oxidative refining of silicon is done by blowing oxygen-enriched air through the melt to reduce contaminants with high affinity for oxygen like aluminium and calcium. The oxidation reactions are strongly exothermic, and depending on the oxygen content of the gas, the temperature increase during refining can be several degrees [1]. However, the amount of heat lost through the ladle wall and the melt surface can also be significant, and in the current calculation, it seems like the two effects nearly cancel each other out.

Remelting slag directly in the ladle will have a synergy effect on the overall economy of the process. The silicon which is currently used to cool the tapped melt is actually of sellable quality, which has been crushed to size specifically for this use. If off-grade material is upgraded and added to the ladles instead, the silicon which is now used for cooling can be sold. However, as stated in chapter 4.3.1 Heat balance, a separation method has to be introduced into the production line; otherwise there will be no outlet for process slag. The efficiency of the separation process will determine the amount of material which can be remelted.

If the results from the heat balance is added to the results of the optical separation trials, and one assumes that an industrial separator will achieve the same results, the total annual amount of upgraded off-grades is about 2650 tons. Ergo, the heat from the ladles will not be enough to melt the whole of the production. However, this calculation assumes that the only product streams from the separator are waste and charge for remelting. If a system of two or more separators in series was installed, the first separator could do a coarse separation and the second did a fine separation. This would give three product streams: “Waste”, “remelts” and “silicon to sale”. The flow chart for two separators in series is shown in Figure 53, below.

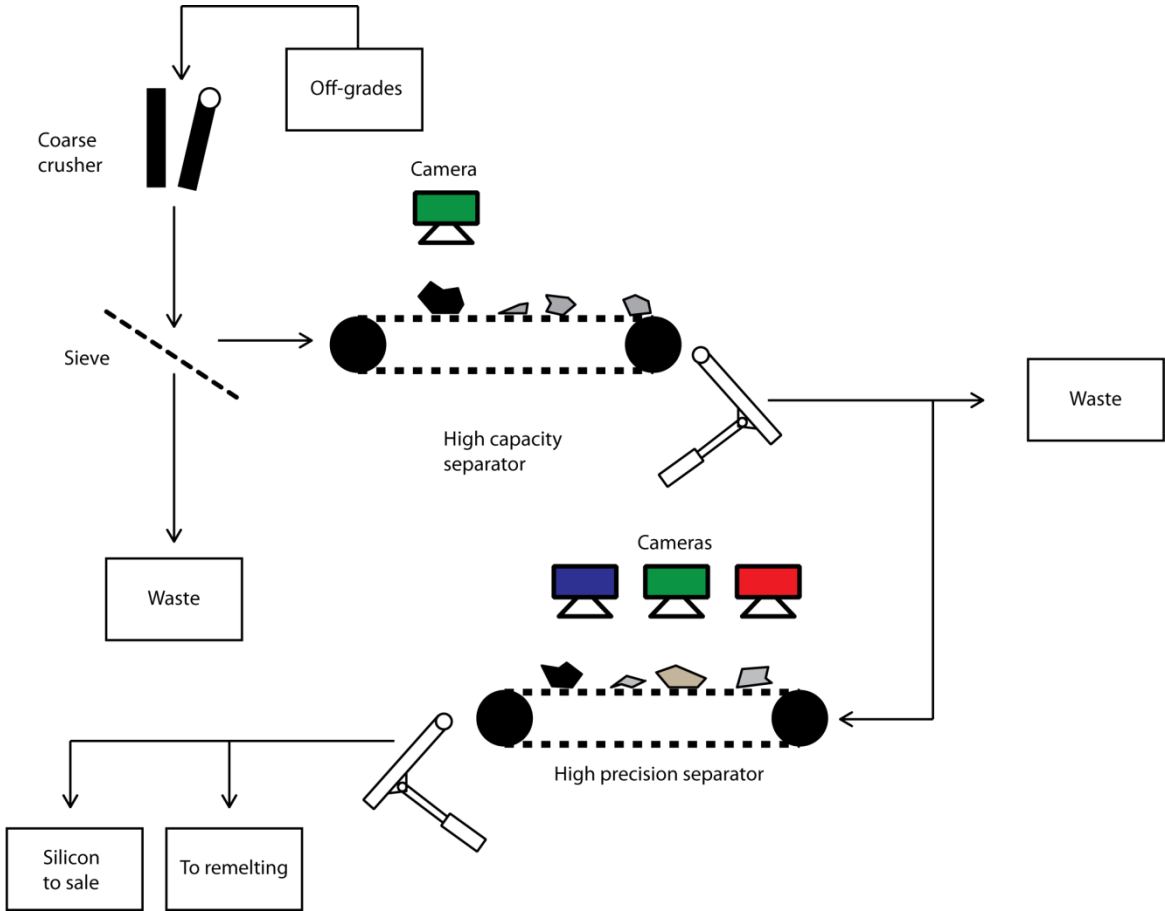


Figure 53: Flow sheet for a double optical sorting scheme

5.3.2 Dimensioning an induction furnace for remelting off-grades

The two furnace designs presented in chapter 4.3.2 Dimensioning an induction furnace for remelting off-grades, represent two completely different approaches to the problem. In the first design, low frequency currents are used to induce eddy currents in the charge itself. Because of the very low resistivity of liquid silicon, the solenoid current must be very large. This leads to ohmic losses in the conductor of about 0.7 MW, giving a theoretical electrical efficiency of just 78 %. However, the thermal efficiency of the system would be reasonably high, seeing as an insulating refractory could be used to contain the charge. One of the worst aspects of this option is the extremely high magnetic field strength produced by the high current. The theoretical maximum magnetic field strength before splashing becomes an issue is 82 kA/m, but the design demands a magnetic field strength of 205 kA/m. A lid could of course be installed on the furnace to reduce the dangers of splashing, but the

velocity of the melt would still be very high. As shown in chapter 2.2.5 Melt stirring speed, silicon would likely be entrained into the slag. This could be abated by superheating the melt to say 1700 °C, turning off the power and letting the entrained particles settle again. In addition to the electrical problems, there could be a number of practical problems with direct heating. Since liquid silicon is the only susceptor in the system, the likely remelting strategy is one where solid charge is continually melted into a bath of liquid charge. In other words, the assumption made in chapter 4.3.2 saying that the resistivity of the charge was equal to the resistivity of liquid silicon would be more or less correct, but the melt height would be a function of time. The ohmic losses in the conductor depend on the length of wire in the conductor, but the current generated in the charge depends on the height of the charge. Therefore the power generated in the charge would also be a function of time, resulting in a reduction in electrical efficiency.

The second design features a carbonaceous lining which acts as susceptor for a high frequency magnetic field, and therefore as the only conductor of eddy-currents. The ohmic losses in the inductor are reduced to 0.07 MW, the magnetic field strength is just 23.3 kA/m, and the electrical efficiency is increased to 97 %. There is no need for a liquid sump either, seeing as the lining will act as the susceptor at all temperatures. However, the thermal efficiency of indirect heating is likely to be much lower than for direct heating. The thickness of the insulating refractory will be reduced to a few millimeters, and the hottest part of the carbon lining will be just next to the insulation, since the outer part of the lining will be closest to the coil. In addition, the produced heat will have to be conducted from the lining into the charge. Even though carbonaceous materials generally have high thermal conductivities, the lining will probably have to be superheated to several tens or hundreds of degrees, giving further increases in thermal losses.

The choice of furnace setup is going to be decided only after careful weighing of the pros and cons of each option. It would be advisable to do a thermal modeling of each option, using finite element computer simulation software. By carefully modeling both the electrical and the thermal behavior of each option, while keeping practical problems like charging, tapping and maintenance in mind, the best overall solution can be found.

5.3.3 Freeze lining thickness

As explained in chapter 2.3.3 and 2.3.4, the freeze lining concept is in many ways superior to traditional refractory lining systems. It is always chemically stable with regards to the charge, seeing as it is made out of the charge, it can be easily adjusted to accommodate more intensive operation by increasing the cooling rate, and during normal operation it should last almost indefinitely. However, using it in an induction furnace could pose a few problems. It cannot be used for indirect heating of the charge, naturally, as the lining is the hottest part of the furnace at any given moment, but it might be viable for direct heating. Both solid silicon and solid slag have a very high electrical resistance and are therefore insusceptible to the magnetic field. The problem then would be to control the heat flow very carefully so that the lining does not grow more than necessary, reducing the electrical efficiency of the furnace.

The results of the modeling of a 5 cm freeze lining show a few interesting aspects. The minimum cooling capacity is rather modest, compared to the maximum capacity of coolers. It also means that upgrading the furnace to higher capacities will be fairly easy. However, as mentioned in the previous

chapter, direct heating will need a large magnetic field strength to produce the necessary power, which will give a large melt stirring speed. In the model, the flow characteristics of the melt were assumed to be governed by natural convection with laminar flow, but with such a high magnetic field strength this assumption might not be valid. If that is the case, the heat transfer coefficients could be altered, increasing the demands on the cooler. This must be included when choosing a lining concept for the remelting furnace.

6. Conclusions

This project has studied various ways of separating silicon from slags in off-grade materials. The aim was to find a separation method which would separate silicon and slag efficiently, cheaply and at low risk to personnel. The investigated methods were dense medium separation, flotation, optical sorting and remelting of slag with fluxes added.

1. **Dense medium separation using magnetite suspended in water failed.** The viscosity of the suspension increased to levels where vertical movement of particles became impossible, before the density required for floating the lighter phase was reached.
2. **Zeta potential measurements showed that flotation is not viable in water at pH 7.** A zeta potential measurement of slag and silicon was carried out at room temperature, using neutral solutions without surface activators. The results showed that their zeta potential is almost equal at the investigated conditions, which indicates a poor flotation potential. The potential found for silicon was 34.5 ± 6 mV, the potential of slag was found to be 38 ± 4 mV.
3. **Optical separation of slag and silicon proved successful.** A sample was sent to Comex labs, where it was separated into waste and product. The product fraction had an average silicon content of 74 wt%, compared to 52 wt% in the original off-grade material, while the waste fraction contained 7.5 wt% silicon. The separation efficiency was best for the coarsest particles, both in the waste and the product fractions. This was the expected result based on theory.
4. **Adding slag fluxes seem to increase the settling efficiency.** The work done on remelting off-grade material was based on previous work by the author, which established the settling efficiency as a function of time [2]. In this thesis, the effect on settling efficiency and silicon quality of adding fluxes to the melt has been investigated, with focus on CaO and MgO additions. According to theory, adding these fluxes should increase the settling efficiency by reducing slag viscosity and melting point, and increasing the interfacial tension between slag and silicon. By using chemical analysis and area analysis of slag samples, it was indicated that adding fluxes will increase the settling efficiency. The silicon quality was unaffected by CaO additions, but MgO additions led to an increased magnesium content.
5. **The main source of error in the experiments was high sample heterogeneity.** An error analysis of the remelting experiments was done, which concluded that only full scale application is likely to quantify the effect of fluxes accurately. Because of the heterogeneity of the slag sample, and because surface effects dominated small scale separation, accurate quantitative data could not be established.

7 Future work

Future work with dense medium separation should focus on using a denser separation media. Either a suspension of ferrosilicon in water, as the density of ferrosilicon is a lot higher than magnetite, or true heavy liquids. Using these suspensions, it should be possible to determine whether a medium density exists where it is possible to separate slags from silicon. If such a density exists, an investigation of the economic potential of the separation method should be carried out.

The zeta potential experiments showed that flotation is not viable without changing the pH or adding some kind of surface activator to the mix. It is likely that the zeta potential of one of the phases could be shifted to the point where flotation is viable by changing the pH or adding activators. However, finding the optimal combination of additives is likely to be time consuming, and flotation is inherently expensive compared to other separation methods [3]. It is therefore not recommended to investigate it further until other options have been researched.

As initial tests with optical sorting proved positive, further work should focus on increasing the efficiency and yield of the process in order to maximize the economic potential of the method. This can be done by tuning the separation thresholds between refractories, silicon and slags and by finding the optimal grain size. There must be a tradeoff between tonnage and yield from the separator, which will be a function of particle size. Therefore, an optimal grain size must exist where the tonnage equals the total production of off-grades and the yield is maximized. An economic analysis of the project should then be carried out to determine the optimal setup for optical separation of off-grades.

The remelting experiments have only yielded qualitative data of the effect of slag additions on settling efficiency, because of extreme sample heterogeneity. Future work should therefore focus on producing quantitative data, e.g. settling time as a function of slag composition or viscosity. This cannot be done using the same scale and setup as was used in this thesis. The experiments should be done at a larger scale using synthetic slags, much better temperature control and control of holding time. A larger number of samples should be taken from each experiment to get more representative results with less variation.

8. References

1. Schei, A., J.K. Tuset, and H. Tveit, *Production of high silicon alloys*, 1998, Trondheim: Tapir. 363 s.
2. Østensen, O.J., *Upgrading of waste from the silicon process: Dressing or remelting as a route to increased silicon yield from Elkem Thamshavn*, 2010, Norwegian University of Science and Technology: Trondheim.
3. Sandvik, K.L., M. Digre, and T. Malvik, *Oppredning av primære og sekundære råstoffer* 1999, Trondheim: Tapir. 497 s.
4. Aylward, G.H. and T.J.V. Findlay, *Si chemical data* 2008, Milton: Wiley. XI, 212 s.
5. Burt, R.O., *Dense-Medium Separation*. Ullmann's Encyclopedia of Industrial Chemistry 2000: Wiley-VCH Verlag GmbH & Co. KGaA.
6. Sigma-Aldrich. *Product details: Tetrabromoethane*. 2011; Available from: http://www.sigmaaldrich.com/catalog/ProductDetail.do?lang=en&N4=86760|FLUKA&N5=SEARCH_CONCAT_PNO|BRAND_KEY&F=SPEC.
7. Sigma-Aldrich. *Product details: Diiodomethane*. 2011; Available from: http://www.sigmaaldrich.com/catalog/ProductDetail.do?lang=en&N4=158429|SIAL&N5=SEARCH_CONCAT_PNO|BRAND_KEY&F=SPEC.
8. Sigma-Aldrich. *Product details: Sodium polytungstate*. 2011; Available from: http://www.sigmaaldrich.com/catalog/ProductDetail.do?lang=en&N4=71913|FLUKA&N5=SEARCH_CONCAT_PNO|BRAND_KEY&F=SPEC.
9. DeVaney, F.D. and S.M. Shelton, *Properties of suspension mediums for float-and-sink concentration*. U.S. Bureau of Mines Report of Investigations, 1940. **3469-R**.
10. Wills, B.A. and T. Napier-Munn, *Wills' mineral processing technology: an introduction to the practical aspects of ore treatment and mineral recovery* 2006, Amsterdam: Elsevier/BH. viii, 444 s.
11. Chemistry, E. *Element Silicon*. 1995; Available from: <http://environmentalchemistry.com/yogi/periodic/Si.html>.
12. Kolacz, J., *Test report on separation of metallurgical slag in the VSX and OSX optical sorting system*, 2011, Comex AS. p. 9.
13. COMEX, *Sorting solutions: OSX separator series*, 2011.
14. Olsen, S.E., M. Tangstad, and T. Lindstad, *Production of manganese ferroalloys* 2007, Trondheim: Tapir akademisk forlag.
15. Allibert, M., et al., *Slag Atlas*. 2nd ed, ed. V.D.E. (VDEh) 1995, Düsseldorf: Stahleisen.
16. Engh, T.A., C.J. Simensen, and O. Wijk, *Principles of metal refining* 1992, Oxford: Oxford University Press. 473 s.
17. Yanniotis, S., S. Skaltsi, and S. Karaburnioti, *Effect of moisture content on the viscosity of honey at different temperatures*. Journal of Food Engineering, 2006. **72**(4): p. 372-377.
18. Engh, T.A., C.J. Simensen, and O. Wijk, *Principles of metal refining* 1992, Oxford: Oxford University Press. xxx, 473 s.
19. Stølen, S., T. Grande, and N.L. Allan, *Chemical thermodynamics of materials: macroscopic and microscopic aspects* 2004, Chichester: Wiley. XII, 395 s.
20. Wikipedia, *Surface Tension*. 2010.
21. Zumdahl, S.S., *Chemical principles*. 5th ed 2005, Boston: Houghton Mifflin. xix, 1070, 94 p.
22. Keene, B.J., *A review of the surface tension of silicon and its binary alloys with reference to Marangoni flow*. Surface and Interface Analysis, 1987. **10**(8): p. 367-383.
23. Dumay, C. and A.W. Cramb, *Density and interfacial tensions of liquid Fe-Si alloys*. Metallurgia and materials transactions B, 1995. **26B**: p. 4.
24. Abdallah, M., R. Diabi, and A. Belhamra, *Industrial applications for induction heating*. Journal of Engineering and applied sciences, 2007. **2**(7): p. 5.
25. Heaviside, O., *The induction of current in cores*. The electrician, 1884. **12**.
26. Schneider, C.P.E., *Electric Furnace*, U.S.P. Office, Editor 1904: France.

27. Burch, C.R. and N.R. Davis, *An introduction to the theory of eddy-current heating*1928, London: Ernest & Benn Ltd.
28. Mühlbauer, A., *History of induction heating and melting*2008: Vulkan-Verlag GmbH.
29. Tipler, P.A. and G. Mosca, *Physics for scientists and engineers*2004, New York: Freeman. XXX, 1116, [95] s.
30. Zinn, S. and S.L. Semiatin, *Elements of induction heating: Design, control and applications*1988: ASM International.
31. Serway, R.A. and J.W. Jewett, *Principles of physics*1998, Fort Worth: Saunders College Publishing. XXXII, 954 s.
32. Allen, P.B. and J.Q. Broughton, *Electrical Conductivity and Electronic Properties of Liquid Silicon*. Journal of Physical Chemistry, 1987. **91**: p. 7.
33. Kennedy, M.W., et al., *Review of classical design methods as applied to aluminum billet heating of induction coils*, in *TMS 2011, EDP Congress*2011: San Diego.
34. Ahmed, M.M., M. Masoud, and A.M. El-Sharkawy, *Design of a Coreless Induction Furnace for Melting Iron*, in *International Conference On Communication, Computer And Power (Icccp'09)*2009: Muscat, Oman.
35. Chen, L.X., et al., *3D Electromagnetic Simulation Study for the Distribution of Electromagnetic Field of Microwave Sintering Cavity*. Advanced Materials Research, 2009. **79 - 82**: p. 4.
36. Office of Engineering Standards, I.f.A.T., *Copper Wire Tables*, H. 100, Editor 1966, US National Bureau of Standards: Washington D. C.
37. Weisstein, E.W. *Root-mean-square*. Mathworld 2011 [cited 2011 12.5]; Available from: <http://mathworld.wolfram.com/Root-Mean-Square.html>.
38. Sundberg, Y., *Elektrougnar och induktiva omrörare*1978, Västerås: ASEA Ugnsbyrå.
39. ISO, *Terminology for refractories*, 2001.
40. Routschka, G. and H. Wuthnow, eds. *Pocket manual of refractory materials*. 3rd ed. 2008, Vulkan-Verlag GmbH: Essen, Germany.
41. Seltveit, A., *Ildfaste Materialer*. 2. utgave ed1992, Trondheim: Tapir forlag.
42. Babaitsev, I.V. and O.V. Kuznetsov, *Energy of Explosions Occurring when Water Falls onto a Layer of Molten Metal*. Metallurgist, 2001. **45**(5): p. 185-188.
43. Joubert, H., *Designing for slag "freeze linings" on furnace sidewalls - an engineering perspective*, in *Molten slags, fluxes and salts*, S. Seetharaman and D.U. Sichen, Editors. 2000: Stockholm.
44. Ildfast, A., *Silmet 75*, 2009, AS Ildfast.
45. Ildfast, A., *Rescocast 17G*, 2009, AS Ildfast.
46. Hear, A.M., A.J. Dzermejko, and P.H. Lamont. *Freeze lining concepts for improving submerged arc furnace lining life and performance*. in *8th International Ferroalloys Congress*. 1998. Beijing, China.
47. Kurz, W. and D.J. Fisher, *Fundamentals of solidification*1998, Uetikon-Zuerich: Trans Tech Publications. 305 s.
48. Toolbox, E. *Thermal Conductivity of some common Materials and Gases*. 2011 [cited 2011 23.05]; Available from: http://www.engineeringtoolbox.com/thermal-conductivity-d_429.html.
49. Pan, Y., S. Sun, and S. Jahanshahi, *Efficient and portable mathematical models for simulating heat transfer in electric furnaces for sulphide smelting*. Sohn International Symposium; Advanced Processing of Metals and Materials: International Symposium on Sulfide Smelting, 2006. **8**: p. 14.
50. Voermann, N., et al., *Furnace cooling design for modern high-intensity pyrometallurgical processes*, in *Copper 99 - Cobre 99; Fourth international conference*1999: Phoenix, Arizona.
51. Voermann, N., et al., *Furnace technology for ferro-nickel production - an update*, in *International Laterite Nickel Symposium*2004. p. 563-577.
52. Slaven, G., A. MacRae, and L. Valentas, *The implementation of Ultralife copper casting technology in the EAF*, in *AISE*2003: Pittsburg, Pennsylvania.

53. Sarvinis, J., et al., *"Furnace Design for Modern, High-Intensity Pyrometallurgical Processes, in Metallurgical Plant Design and Operating Strategies 2002*, AusIMM: Sydney, NSW. p. 318-331.
54. Hopf, M. and E. Rossouw, *New opportunities - Exhaustive monitored copper coolers for submerged arc furnaces, in Southern African Pyrometallurgy 2006*, R.T. Jones, Editor 2006, South African Institute of Mining and Metallurgy: Johannesburg.
55. Sigma-Aldrich. *Magnesium carbonate basic*. 2011 [cited 2011 16.05]; Available from: http://www.sigmaaldrich.com/catalog/ProductDetail.do?lang=en&N4=13118|SIAL&N5=SEARCH_CONCAT_PNO|BRAND_KEY&F=SPEC.
56. COLORANA, *Technical information, Particle size distribution*, 2006: Mo i Rana.
57. Malvern. *Zetasizer nano ZS datasheet*. 2011 [cited 2011 29.03]; Available from: <http://www.malvern.com/common/downloads/MRK496.pdf>.
58. Bakken, J.A., *Elektriske ovner, induksjonsovner - teori og virkemåte* 1993, Trondheim: Metallurgisk institutt, NTH.
59. *Industrial Metal Casting: Electric induction furnaces*. [cited 2011 16.6]; Available from: <http://www.industrialmetalcasting.com/electric-induction-furnaces.html>.
60. Roine, A., *HSC chemistry*, 1999, Outokumpu Research Oy: Pori.
61. Ophaug, H., *Omsmelt i øse*, O.J. Østensen, Editor 2011: Trondheim.
62. Berman, R.G. and T.H. Brown, *A thermodynamic model for multicomponent melts, with application to the system CaO-Al₂O₃-SiO₂*. *Geochimica et Cosmochimica Acta*, 1984. **48**: p. 18.

Appendix

1 Count data, microscopy analysis

The count data from the microscopy analysis are given in Table 14 and Table 15, below. The tables list the total area of particles with a sphere equivalent radius between the given radius and the previous radius.

Table 14: Microscopy count data. experiments without slag fluxes

Position	Bottom	Middle	Top	Bottom	Middle	Top	Bottom	Middle	Top
radius	Original	Original	Original	Hand	Hand	Hand	Optically	Optically	Optically
0.631	8896.945	19695.47	17334.19	11727.4	7339.859	8621.848	67553.82	8572.941	17438.05
0.794	0	0	0	0	0	0	0	0	0
1	10768.47	20492.9	18940.13	13035.77	8290.324	9222.302	75136.89	9753.987	19297.76
1.259	23199.78	36455.98	36527.78	26085.99	17019.5	18513.75	127593.6	24029.49	41398.95
1.585	15921.18	21614.07	22969.33	17394.08	11523.69	12706.33	96394.71	22570.53	31876.85
1.995	38602.48	46741.19	51459.07	40020.31	24556.74	28827.23	172824	53235.88	67145.36
2.512	48028.9	52484.36	63635.16	49443.68	31039.91	37205.1	200088.5	83746.53	87961.94
3.162	57020.95	59878.16	70983.22	53363.09	32337	41367.13	212385.7	108122	103674.4
3.981	86063.74	78667.04	100820.5	81285.83	43868.34	62467.73	267329.5	185694.5	146303.7
5.012	110770.2	89629.84	114797.7	93978.28	55162.89	75530.18	290630.9	245716.3	165634.7
6.31	120860.7	95701.82	130173.5	99987.59	55152.09	73287.1	272686.4	298858.6	185582.2
7.943	154365.2	111986.5	142205.9	127032	64538.15	102737.8	300484	377460.7	206238.2
10	165272.8	131675.4	163002.4	142421.3	76550.75	103200.9	290753.8	417113.8	237452.2
12.589	188357	140237.8	205717.2	145386.9	65399.9	131076.4	300198.3	371301.7	251901.9
15.849	202500.9	170765.8	244696.2	181226.1	82159.74	134256	356522.2	311072.4	293793
19.953	216909.3	173418.3	312047.2	168058.3	105330.8	187269	376643.3	318065.7	306610.8
25.119	295964.3	181282.5	331430.6	230029.5	140071.3	178520.1	446014.4	329158.5	401533.5
31.623	265780.1	294398.1	385273.2	245457.1	190787.8	270513.6	537395.2	320397.4	473069.5
39.811	443542.3	254734.7	471015.9	338092.2	203076.9	239852.6	606475.9	392850.2	551612.6
50.119	467419.2	287113	480878.8	332611.7	361796.6	279995.9	680797.4	362093	495472.1
63.096	494038.8	459721.5	580481.3	272906.3	329140.2	385782.1	881746.1	454233.2	587256.2
79.433	500668.5	400923.8	751157.1	279039.4	426857.3	381461	905315.6	643875.1	721521.3
100	417401	439624.7	771292.1	530411.1	609395.8	673628.3	1062153	348230.1	830745.1
125.893	775231.1	511669.5	1167835	502065	613244.7	476521.1	1718469	494891.4	819053.6
158.489	1228821	532883.3	1207613	319312.5	567056.9	1030352	1464550	669602.3	662196.4
199.526	891533.9	868981.7	831981.4	857907.2	1858613	1236664	2134901	396466.8	1427230
251.189	1489632	398723.6	1790034	954710.6	1766108	867954.9	1703933	160566.9	1441759
316.228	1048299	659478.3	1259557	959850.6	3367590	1234723	1896935	602376.5	263262
398.107	1698274	1325019	2007135	0	2691140	586724.4	918786	468206.1	1006844
501.187	4116679	0	2181588	0	3909932	2656627	3037864	637549.4	1665735
630.957	1161812	0	0	0	8231108	2553034	2641898	0	0
794.328	2469230	1629334	4635930	0	2123551	0	1943818	2323429	0
1000	0	0	0	0	9755565	2681037	0	0	3929000
1258.92	0	4590434	0	5957209	9278069	0	0	0	0
1584.89	0	0	0	0	8873033	0	0	0	0
1995.26	0	1452895	0	0	0	0	0	0	0
2511.88	0	1712257	0	0	1865099	2419143	0	0	0
3162.27	0	0	0	0	0	0	0	0	0
Sample area	1.12E+08	1.73E+08	1.56E+08	91029904	1.39E+08	1.1E+08	1.58E+08	1.15E+08	1.69E+08

Table 15: Microscopy count data, experiments with slag fluxes

Position	Bottom	Bottom	Middle	Top	Bottom	Middle	Top	Bottom	Middle	Top	Bottom	Middle	Top
Radius [µm]	Low lime	Low lime	Low lime	Low lime	Dolomite	Dolomite	Dolomite	High lime	High lime	High lime	MgO	MgO	MgO
0.631	11912.32	4105.438	20007.05	7781.402	21429	20083.41	18647.71	21587.85	12639.8	18241.44	21178.52	22200.31	19967.33
0.794	0	0	0	0	0	0	0	0	0	0	0	0	0
1	15171.68	4727.42	22183.23	9136.743	16241.16	20581.55	15516.97	25019.79	14108.31	20245.32	22094.58	24093.63	22296.32
1.259	35557.54	9995.763	43234.26	19189.11	21322.24	37108.41	22492.56	47983.06	28677.3	37592.73	43742.82	47023.41	45764.48
1.585	30454.44	6486.035	31132.77	15154.12	15016.6	23650.7	15146.47	32264.98	21504.09	24986.12	29673.65	32012.83	31934.94
1.995	68771.13	15375.51	65502.7	35907.37	22859.24	48592.85	25585.01	69732.27	49703.58	53041.86	65542.52	69040.16	68916.38
2.512	92542.43	21328.4	81540.24	50375.82	30450.13	56505.82	34228.74	84577.73	65853.72	62290.56	77268.42	82220.13	85758.71
3.162	115281.6	26321.58	95651.23	61452.12	31669.31	60232.67	35238.56	90225.79	78164.34	65097.74	85317.86	90525.03	94315.84
3.981	165152	41386.97	136677.9	92302.4	45261.79	82361.56	53749.44	133478.8	128212.2	91367.13	109840	123548.7	131733.9
5.012	208892.8	53896.22	172481.1	122510.7	68616.31	85787.11	71993.06	152465.3	158971.2	109634.8	121497.7	139624.7	144138.3
6.31	233616.2	58020	197595	144594.1	74258.82	104933.5	78286.46	173316.2	181599.2	108041.3	137752	152751.8	145666.5
7.943	296575.2	78196.3	239620.4	158787	108204.8	119931.8	107298.8	186543.4	205352	130428.5	151373.5	172313.7	172433
10	344797	94774.27	260247.3	191924.6	131878.6	155685.2	123571.2	214036.6	238231.6	142622.9	163411.8	187403.5	175412.2
12.589	401398.9	124477.2	261104.8	236170.4	168195.8	170370	202927.2	234665.4	263324.6	155199.3	183689.1	211107.7	180391.9
15.849	488085.8	122388.6	294526.4	244736	219381.5	250980.5	219202.8	236153.5	292320.2	156880	232168.8	221603.1	220493.8
19.953	552560.3	127018.2	252151	247460.2	258319.2	303610	299882.1	272744.4	315492.7	193180.5	234944.9	259313.9	210886.2
25.119	647835.3	178781.3	304730.1	296457.8	289537.8	438031.1	407347.1	297669.5	364496.4	209087.8	268574.6	260771.5	267569.2
31.623	723984.6	199009.6	285074.8	373607.5	295678.5	470944.1	441737.8	401556.4	351849.8	271561.7	303888	342567.6	327977.5
39.811	595798.9	183441.5	372531.8	328628.3	329068.4	686496.4	772725.4	428262.9	452847.3	310198.4	405269.1	385915	355014.1
50.119	771663.4	273810.8	310965.5	320617.4	347359.3	644829.9	726462.6	387494.8	568069.9	373165.8	581152.1	443655.3	298629
63.096	652153.3	313841	599401.7	333815.6	397877	938419.8	1166703	509990.3	651578.8	447128.4	551507.2	410150.9	425404.2
79.433	556717.4	385661.3	398625.8	448420.9	498601.1	1150287	1316425	652417.7	515619.3	505866.5	501647.9	745786.4	689943.6
100	788884.6	411014.2	643349.4	499429.3	632151.3	1468771	1274960	620028.7	599446	721374.6	555071.9	797062	525439.2
125.893	1087037	1002923	690440.2	466858.5	466898.2	1622797	1836532	681371.9	725154.8	757925.8	976333.9	702191.5	1047450
158.489	858487.8	1056277	876632	991241.9	857542.1	1034193	1944952	1030655	1260666	651311.5	1130308	1042996	956926.2
199.526	1272298	1458498	584701.4	1049005	854573.3	2597354	1801244	1104570	839052.6	905632.1	962350.3	435881.3	1174456
251.189	592500	564453.4	857418.3	1212527	435117.3	1653154	1105646	1574250	181493.4	1543739	1145205	578307.1	359087.6
316.228	1205817	613127	664661	1584119	610847.4	3042985	2066404	1421389	601221.4	2362904	1493800	1753016	267546.3
398.107	1279719	1458132	999582.9	1371371	0	3040375	1123773	1088936	473755.5	1459013	556312.6	1863559	1548873
501.187	3274362	1418749	1567434	748953.8	842878.5	2683287	755114.3	1652778	2579583	2711254	0	2672726	1377800
630.957	2634222	4465291	1175894	1476296	0	0	3608673	1176578	0	1288740	2357655	0	1521083
794.328	0	4026885	5575838	2455246	3245564	5615466	1846226	1948121	0	0	0	4030895	0
1000	9280049	2642460	3415910	0	0	0	3724136	0	3742617	0	3935161	0	0
1258.926	0	5075558	0	0	0	0	0	0	0	0	0	0	0
1584.893	9396098	0	0	0	0	7137503	0	0	0	6369578	0	9279829	0
3162.278	0	25664010	0	0	0	0	0	0	0	0	0	0	0
437008	98022728	1.23E+08	1.51E+08	1.25E+08	1.71E+08	1.72E+08	1.69E+08	1.24E+08	1.47E+08	1.24E+08	1.43E+08	1.53E+08	1.6E+08

2 Design of an induction furnace for remelting off-grades

Most of the equations presented by Kennedy et al. were given in chapter 2.3.2, however some equations were deemed of less interest to the reader, and were omitted. They will be given here instead.

The short “air” coil inductance is given in equation (2.1), below.

$$L_0 = \frac{k_N A_c \mu_0 N_c^2}{l_c} \quad (4.1)$$

The inductive reactance (X_0), the total coil impedance (Z_0) and the voltage drop (V_0) across the short “air” coil is estimated using equations (2.2) to (2.4).

$$X_0 = \omega L_0 = 2\pi f L_0 \quad (4.2)$$

$$Z_0 = \sqrt{(R_c^2 + X_c^2)} \quad (4.3)$$

$$V_0 = I_0 Z_0 \quad (4.4)$$

The magnetic flux density of the “air gap” can be calculated using equation (2.5). It is assumed that the magnetic flux density is constant across the gap, and that it is this density which induces currents in the charge.

$$B_0^* = \frac{k_N^* \mu_0 N_c I_c}{l_c} \quad (4.5)$$

The contribution of the air gap to the total inductive impedance of the circuit is given by equation (2.6).

$$X_g = \frac{k_N^* \mu_0 N_c^2 \pi^2 (D_c^2 - D_w^2)}{2l_c} \quad (4.6)$$

The inductive reactance of the charge depends on a different Bessel function than the resistance of the workpiece and is calculated using equation (2.7). The functions are given in **Error! Reference source not found.**, below. Finding the total inductive impedance of the system is a matter of summing the impedances of the air gap, the coil and the charge. After the impedance is known, finding the total

$$X_w' = \frac{\sqrt{2\pi} N_c^2 \rho_w \xi_w \psi(\xi_w)}{l_c} \quad (4.7)$$

$$X_t = X_c + X_g + X_w' \quad (4.8)$$

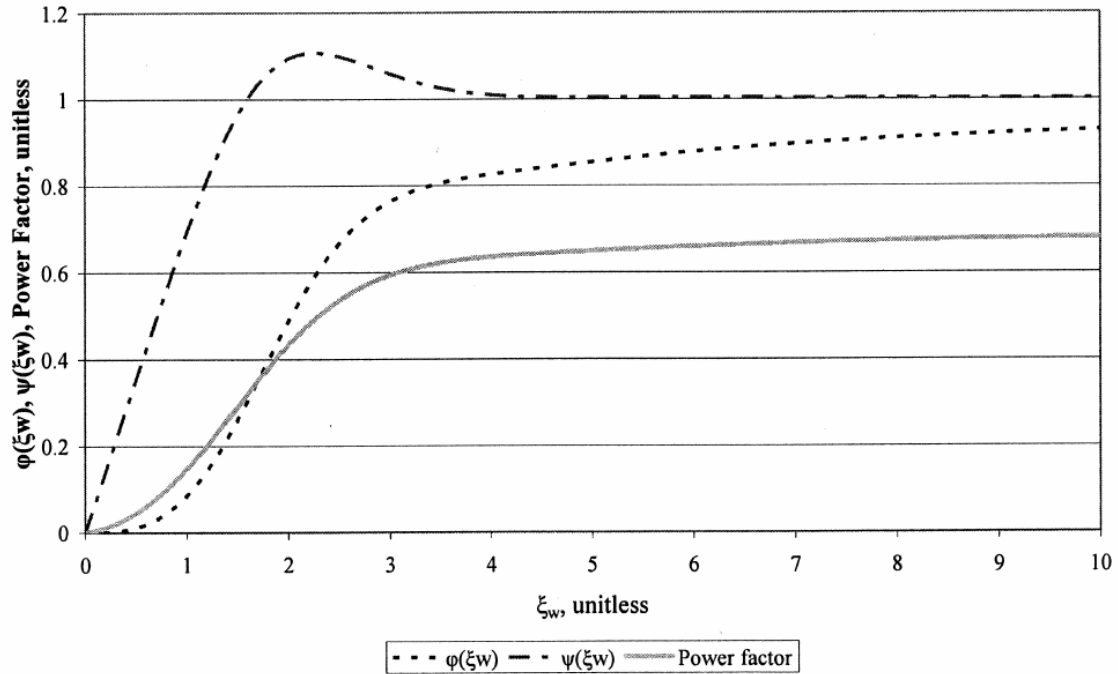
The required capacitance of the system is calculated using equation (2.9). The total inductance of the system is given by L.

$$C = \frac{1}{\sqrt{(2\pi f)^2 \cdot L}} = \frac{1}{\sqrt{2\pi f \cdot X_t}} \quad (4.9)$$

$$L = \frac{X_t}{2\pi f} \quad (4.10)$$

Finally, the reactive power of the system is given by equation (2.11)

$$Q_w = \sqrt{2\pi} \frac{k_N^* N_c^2 I_c^2 \rho_w \xi_w \psi(\xi_w)}{l_c} \quad (4.11)$$



Appendix figure 1: Bessel functions

All of the calculations concerning the dimensioning of an induction furnace for remelting off-grades are given in Table 16, below.

Table 16: Electromagnetic properties of the two furnace options.

Parameter	Symbol	Direct	Indirect	Unit
Frequency	f	50	3000	Hz
Number of turns	N	30	15	--
Skin depth in coil	δ_c	0.0120	0.0015	m
Skin depth in material	δ_w	0.0712	0.0919	m
Magnetic field strength	H	205	23	kA/m
Maximum magnetic field strength	H_{max}	82	82	kA/m
RMS current	I_{rms}	12167	2755	A
Current in the charge	I_w	325607	36998	A
Dimensionless parameter	ξ_w	8.8	6.8	-
Power in the charge	P_w	2.6	2.6	MW
Power lost to cooling	$P_{cooling}$	731523	70247	W
Power needed	P	3.32	2.66	MW
Electrical efficiency	-	78.0	97.4	%
Total circuit resistance	R_t	20	96	Ω
Total circuit reactance	X_t	0.03	0.43	Ω
Total circuit inductance	L	8.64E-05	2.30E-05	Henry

Required capacitance	C	0.12	1.22E-04	F
Nagaoka coefficient	k_N	0.75	0.75	-
Effective Nagaoka coefficient	k_N^*	0.89	0.90	-
Magnetic flux density in air gap	B_0^*	0.26	0.03	tesla
Resistance of the charge	R_w	0.02	0.43	Ω
Inductive reactance of charge	X_w	0.02	0.43	Ω
Reactive power of charge	Q_w	2.60	2.60	
Coil space factor	k_r	0.91	0.95	
Effective area of current path	$a_{current}$	5.72E-04	1.44E-04	m^2
AC resistance of the coil	R_c	3.30E-03	6.19E-03	Ω
Peak current	I_p	17207	3896	A
Power needed in charge	P_{work}	2.6	2.6	MW
Area of coil	A_c	1.08	1.06	
Inductance of "air coil"	L_0	6.85E-04	1.69E-04	Henry
Reactance of "air coil"	X_0	0.22	3.18	Ω
Total coil impedance of "air coil"	Z_0	0.22	3.18	$1/\Omega$
Voltage drop of "air coil"	V_0	2620	8772	V
Inductive reactance of air gap	X_g	1.78E-03	4.46E-04	Ω

3 Cooling system design for a furnace using freeze lining

All of the input parameters used for designing a 5 cm freeze lining for a hypothetical remelting furnace are given in Table 17. All calculated parameters are given in Table 18, below.

Table 17: Input parameters for calculating a 5 cm freeze lining

Parameter	Symbol	Value	Unit
Nusselt number constant	C	0.32	-
Nusselt number constant	m	0.3	-
Density of slag	ρ_{slag}	2200	kg/m ³
Volumetric expansion coeff.	β_{slag}	$1.0 \cdot 10^{-4}$	-
Holding temperature	T_{slag}	1600	°C
Freezing point average	T_{freeze}	1447.5	°C
Temp of cooling medium	T_{cooling}	20	°C
Height of melt	L	1.6	m
Dynamic viscosity	M	38.23	Pa·s
Specific heat capacity	C_p	1350.28	J/kg·K
heat transfer coeff.	k	1.7	W/m·K
Freeze lining thickness	X_{freeze}	0.05	m
Thermal cond. freeze lining	k_{freeze}	3	W/m·K

Table 18: Calculations and output parameters

Parameters	Symbol	Value	Unit
Calculation of dynamic viscosity	A	9.6E-12	
	B	44314	
	μ	38.2	Pa·s
Calculation of specific heat capacity of slag	Al ₂ O ₃	142	J/mol·K
	CaO	60	J/mol·K
	SiO ₂	83	J/mol·K
	Slag	93.94	J/mol·K
Grashof number	Gr	2030	
Prandtl number	Pr	30363	
Flow characteristic number	Gr*Pr	$6.2 \cdot 10^7$	
Nusselt number	Nu	69.5	
Heat transfer coeff. at hot face	h_{slag}	73.9	W/m ² ·K
Heat flux	q	11.3	kW/m ²
Total thermal resistance	R	0.031	m ² ·K/W
Heat transfer coeff. at cold face	h_{tot}	32.4	W/m ² ·K
Safety factor	X_{safe}	4	
"Safe" capacity of cooling system	q_{safe}	45.1	kW/m ²